universität wien

MASTERARBEIT

Titel der Masterarbeit

„An Ion Trap System for Massive Molecular Beams “

Verfasserin

Philine Mitrea, BSc

angestrebter akademischer Grad

Master of Science (MSc)

Wien, 2015

Studienkennzahl lt. Studienblatt:	A 066 876
Studienrichtung lt. Studienblatt:	Masterstudium Physik
Betreuer:	Univ.-Prof. Dr. Markus Arndt

An Ion Trap System for Massive Molecular Beams

by Philine Mitrea

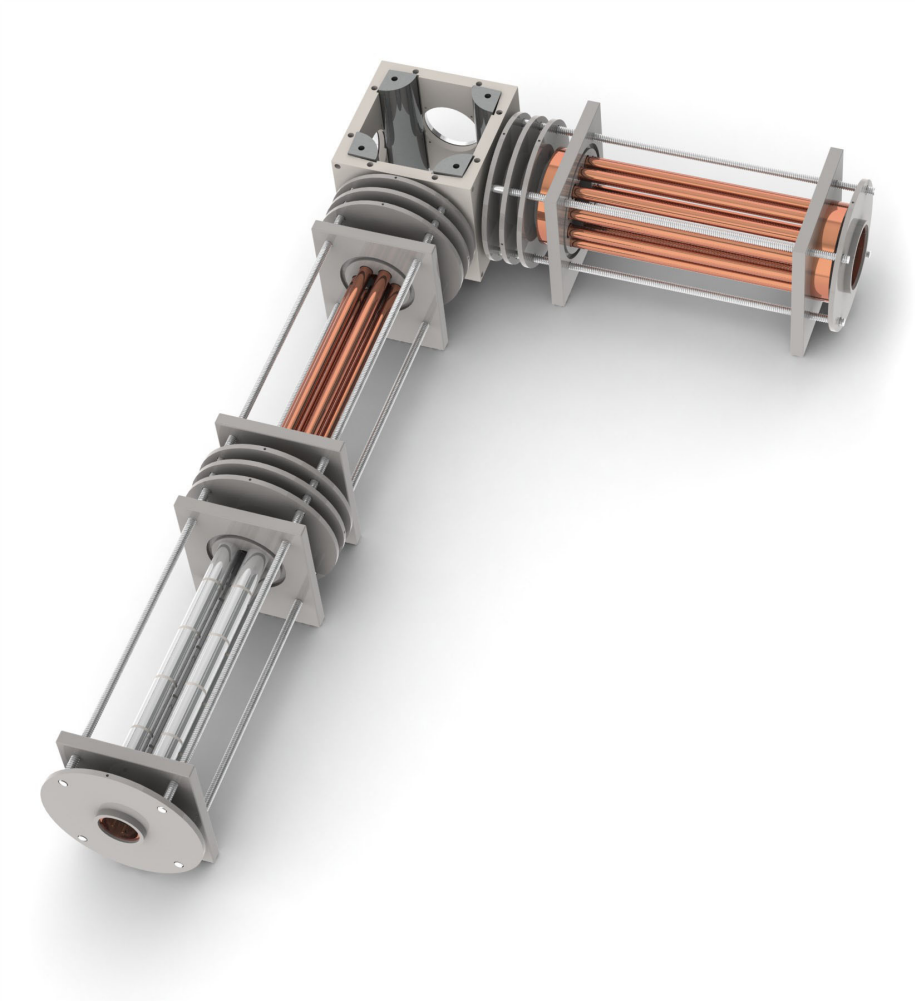

Master thesis, Vienna 2015

To my beloved grandmother

Contents

1 Introduction 1

2 Ion Trap Theory 13
- 2.1 Fundamentals of ions in EM fields . . . 13
  - 2.1.1 Adiabatic approximation . . . 14
  - 2.1.2 The effective potential . . . 15
- 2.2 Confinement in a Multipole . . . 16
  - 2.2.1 The linear quadrupole field . . . 18
  - 2.2.2 The hexapole field . . . 22
  - 2.2.3 The dodecapole field . . . 23
  - 2.2.4 The adiabaticity parameter . . . 23
- 2.3 Heating effects . . . 25
- 2.4 Charge density and Coulomb repulsion . . . 26
- 2.5 Cooling techniques . . . 27
  - 2.5.1 Optical cooling . . . 28
  - 2.5.2 Sympathetic cooling . . . 29
  - 2.5.3 Collisional cooling . . . 30

3 Trap Design 35
- 3.1 Experimental scheme . . . 35
- 3.2 Load particles . . . 36
- 3.3 Buffer-gas cells . . . 38
- 3.4 Mass selection and accumulation . . . 41
- 3.5 Pre-cooling and guiding . . . 42
- 3.6 Bending the ions . . . 43
- 3.7 Cooling stage . . . 45

3.8 Interference experiment . . . 46
3.9 Detection . . . 46

4 Simulation **47**
4.1 Initiation . . . 47
4.2 Outcoupling from the Quadrupole . . . 48
4.3 Simulating the Quadrupole Bender . . . 52
4.4 The Cold Ion Trap System . . . 56
4.5 Simplified setup: Cold Hexapole . . . 62

5 Cooling Technology **65**
5.1 Cryogenic setup . . . 65
5.2 Cooling test . . . 70
5.3 Vibrational analysis . . . 71

6 Outlook & Conclusion **73**

A SIMION Simulation Parameters **77**

Bibliography **87**

Acknowledgements **103**

Curriculum Vitae **105**

List of Figures

1.1 Sketch of far-field diffraction experiment 4
1.2 Sketch of a TL interferometer 6
1.3 Sketch of the OTIMA interferometer 7
1.4 Illustration of molecules being exposed to a standing light wave 8
1.5 Maximal velocities accepted by OTIMA and KDTLI 9
1.6 The Paul trap and the quadrupole mass filter 11

2.1 Mechanical analogon for pseudopotential of the Paul trap 16
2.2 Effective potentials of ion traps of different order 18
2.3 The quadrupole geometry 19
2.4 Stability diagram for the two-dimensional quadrupole field 21
2.5 Lowest stability region 21
2.6 The hexapole geometry 22
2.7 The dodecapole geometry 23
2.8 Number of necessary collisions 31
2.9 Buffer-gas thermalisation time 33

3.1 Schematic view of the Cold Ion Trap System 36
3.2 The open Cold Ion Trap System 37
3.3 The cold ion trap setup with buffer-gas cells 39
3.4 Pumping time for buffer-gas cell 40
3.5 Design of the quadrupole ion trap 41
3.6 Design of the hexapole ion trap 43
3.7 Design of the quadrupole ion bender 44
3.8 The rod diameter comparison - ideal quadrupole field 44
3.9 Design of the dodecapole ion trap 45

4.1 Ions freely moving out of the quadrupole . . . 49
4.2 Divergence angles of ions moving out of the quadrupole . . . 50
4.3 Ions extracted out of the quadrupole trap . . . 50
4.4 Divergence angles of ions driven out of quadrupole . . . 51
4.5 Forward velocity and kinetic energy distributions for outcoupling ions from the quadrupole . . . 52
4.6 Simulated ion beam in quadrupole bender . . . 53
4.7 Ion beam of circular shape, deformed after passing the deflector . . . 53
4.8 Divergence angles of ions passing the quadrupole bender . . . 54
4.9 Velocity and kinetic energy distributions for ions transmitted by the quadrupole deflector . . . 55
4.10 Cold Ion Trap System in SIMION . . . 56
4.11 Buffer-gas cooling at 10^{-3} mbar in Dodecapole . . . 58
4.12 Buffer-gas cooling at 10^{-5} mbar in Dodecapole . . . 59
4.13 Radius and length of ion cloud in dodecapole at 10^{-3} mbar . . . 60
4.14 3D temperature diagram of ions in the Cold Ion Trap System . . . 61
4.15 Simulation graph of the cold hexapole . . . 62
4.16 Velocity and kinetic energy distribution for the cold hexapole . . . 63
4.17 Spatially resolved diagram of the cold hexapole . . . 64

5.1 Exploded view of the interlaced cyrogenic setup . . . 66
5.2 Schematic view of the cryogenic shields . . . 67
5.3 A detail of the PEEK suspension . . . 68
5.4 Assembled cryogenic setup - "Cryobox" . . . 69
5.5 Cooling performance of the Cryobox . . . 71
5.6 Mechanical vibration analysis of the Cryobox . . . 72

List of Symbols

μ_0	Permeability of free space $\mu_0 = 4\pi \cdot 10^{-7}$ Vs/Am
ε_0	Permittivity of free space $\varepsilon_0 = 8.854187817\ldots \cdot 10^{-12}$ F/m
k_B	Boltzmann constant $k_\mathrm{B} = 1.3806488(13) \cdot 10^{-23}$ J/K
σ	Stefan-Boltzmann constant $\sigma = 5.670373(21) \cdot 10^{-8}$ $\mathrm{Wm^{-2}K^{-4}}$
e	Elementary charge $e = 1.602176565(35) \cdot 10^{-19}$ C
h	Planck's constant $h = 6.62606957(29) \cdot 10^{-34}$ Js
amu	Atomic mass unit, 1 amu $= 1.66053892 \cdot 10^{-27}$ kg
mbar	Millibar, 1 bar $= 1\,000\,000$ Pa

Abstract

The endeavour to unveil the scope of quantum mechanics necessitates the ability to study the wave-character of material systems with growing extent and complexity. Sophisticated methods have to be applied to generate superposition states of macroscopic objects that can be detected by an appropriate experimental setup. At this, the preparation of suitable samples for matter-wave experiments is central to the present master thesis. Therein an ion-based instrument is envisaged for providing cold and slow macromolecules.

The design of this device allows for the mass-selection, accumulation and buffer-gas cooling of nanoparticles over a wide mass range. Ion-optical simulations for demonstrating its functionality have been carried through. In addition, a thermal shielding structure for cryogenic application was constructed and experimentally tested. Further on, possible implementations will be presented that might open up new prospects in high mass interferometry.

Zusammenfassung

Das Bestreben den Geltungsbereich der Quantenmechanik zu enthüllen, erfordert die Möglichkeit den Wellencharakter von materiellen Systemen wachsender Ausdehnung und Komplexität zu untersuchen. Raffinierte Methoden müssen angewandt werden um Superpositionszustände von makroskopischen Objekten zu generieren, die durch Messung erfasst werden können. Hierbei ist die Preparation geeigneter Proben für Materiewellen-Experimente das zentrales Thema der vorliegenden Masterarbeit. Es wird ein ionenbasiertes Instrument vorgestellt, das kalte und langsame Makromoleküle liefert.

Das entwickelte Design dieses Apparates ermöglicht die Massenselektion, Akkumulation und Puffergaskühlung von Nanopartikeln. Ionenoptische Simulationen zur Demonstration dessen Funktionalität wurden durchgeführt. Zusätzlich wurde ein Wärmeschild zur kryogenen Anwendung konstruiert und experimentell getestet. Weiters werden mögliche Umsetzungen vorgestellt, die womöglich neue Perspektiven für die Interferometrie hoher Massen eröffnen.

Chapter 1

Introduction

Motivation

Quantum mechanics is an exceptionally successful theory in physics in view of its solid mathematical apparatus, permitting predictions of remarkable certainty albeit it is yet to be completed through interpretation [Pietschmann, 1995]. The discovery of quantisation led to enormous implications foremost in our perception of physical reality. One outstanding example is the hypothesis of Louis de Broglie that every material particle is associated with an oscillatory phenomenon [Broglie, 1923]. De Broglie linked the *energy-frequency equivalence* of light $E = \hbar\omega$ to the *energy-matter equivalence* arising from special relativity $E = mc^2$. Adopting a continuum mechanical property to a corpuscular object, the quantum nature of matter is introduced by the (deBroglie) wavelength λ of the material entity

$$\lambda_{\mathrm{dB}} = \frac{h}{p} = \frac{h}{m \cdot v} \tag{1.1}$$

where h denotes Planck's constant, and m and v stand for the mass and velocity of the particle.

The hypothesis was confirmed by demonstrating the diffraction of free electrons from a single crystal and a platnium foil [Davisson and Germer, 1927, Thomson, 1927]. In analogy to light-interferometers, matter-wave interferometers have mainly been used to prove the wave nature of particles. The first interferometer for neutrons utilised crystal diffraction [Rauch et al., 1974]. Later, standing laser light waves [Gould et al., 1986],

nano-fabricated gratings [Keith et al., 1988] and the mechanical adaption of Young's double slit [Carnal and Mlynek, 1991] were employed to show quantum interference of atoms and even complex molecules [Arndt et al., 1999]. Until now, the quantum character of molecules of some 10^4 amu has been reported [Eibenberger et al., 2013].

In experimental physics one intends to examine aspects of nature through closed and structured systems. Physical exploration requires a quantifiable practice in investigating reproductible phenomena. To confine the macrosopic object to be an observable system it has to be isolated from its environment by employing for instance, vacuum technology. Thus, individual entities are treated independent from their surroundings, covered as a particular case consistent with the physical theory. However, the regarded system is never completely isolated from the external world. As H. D. Zeh argued in [Zeh, 1970], since Schrödinger's equation is only applicable to a closed system, it cannot be expected to describe the macroscopic system exclusively.

Although the superposition of matter-waves is usually not observed in the immediate empirical world, quantum effects reveal themselves under certain conditions (cf. quantum coherence). Decoupling the system of interest from interactions with any exterior degree of freedom, the quantum behaviour of the system can be made visible. If, however, the decoupling from the surroundings is incomplete and 'which-path' information can be obtained for the matter-wave, the loss of coherence (*decoherence*) of the system leads to its classical appearance [Zurek, 1982, Zurek, 2003].

Notwithstanding, quantum mechanic's range of validity for massive objects is yet to be explored. With the Copenhagen interpretation proposed by Niels Bohr [Bohr, 1928], the existence of a border region between classical and quantum physics was presumed. Even with Everett's Many Universes Interpretation [Everett III, 1957], which postpones the quest for this transition by introducing an alternative world for every possible constitute of a superposition, both conceptions recount the moment of observation (or disturbance via decoherence). At this, the initially delocalised quantum state manifests itself in a classical event, representing one of the probable outcomes. Hence, the principle question is still an unsolved issue: is there a limitation on forming superpositions with increasing size, complexity and mass of the regarded system?

Several theoretical models have been developed to describe the breakdown of the

matter wave when approaching a certain collapse limit. Whether modifications on established theories of gravitation [Giulini and Groß ardt, 2011, Marshall et al., 2003, Penrose, 1996], continuous spontaneous localisation mechanisms [Bassi and Ghirardi, 2003, Ghirardi et al., 1986, Adler and Bassi, 2009, Pearle, 1989, Adler et al., 2013, Bassi et al., 2013] or intrinsic fluctuations of spacetime forming gravitational waves [Lamine et al., 2006] are considered, the models suggest inhibitions on the propagation of matter waves for objects exceeding a particular mass. As a consequence, extending the quantum studies to objects with high mass can test collapse models and look for a possible transition to classical mechanics. Today, matter-wave interferometry of particles at ultra-high mass[1] is a promising method for investigating the limits of quantum physics [Nimmrichter et al., 2011b, Arndt and Hornberger, 2014].

Fundamentals of matter-wave interferometry

Matter-wave interferometers consist of three distinct segments: the source, the interference region and the detector. The diffracting elements are capable of separating and recombining the transmitted wave packets. Far-field diffraction in Fig. (1.1) (as in [Arndt et al., 1999]) consisting of a source for large molecules, a diffraction grating and a screen for detection is the most elementary and conspicuous realisation of this idea.

Far-field diffraction requires however the subsequent preparation of spatial coherence. A rather tight collimation of the beam is necessary which makes this scheme not feasible for ultra-high mass nanoparticles. If at all, a fountain configuration would be conceivable allowing molecular samples of around 10^6 amu [Juffmann et al., 2010].

Interferences of complex molecules and nanoparticles in the high mass regime can be observed by setups based on near-field diffraction, particularly in the Talbot-Lau design consisting of three successive gratings [Clauser, 1997, Brezger et al., 2002]. Currently two interferometers of their kind are operated at the Quantum Nanophysics Group in Vienna: the Kapitza-Dirac-Talbot-Lau interferometer (KDTLI) [Gerlich et al., 2007] and the Optical-Time-Domain-Ionizing-Matter-Wave interferometer (OTIMA) [Haslinger, 2013]. The following elements are essential for these particular arrangements:

[1] It will be distinguished between two mass ranges: the regime of high masses around $10^4 - 10^6$ amu and ultra-high masses around $10^7 - 10^{10}$ amu.

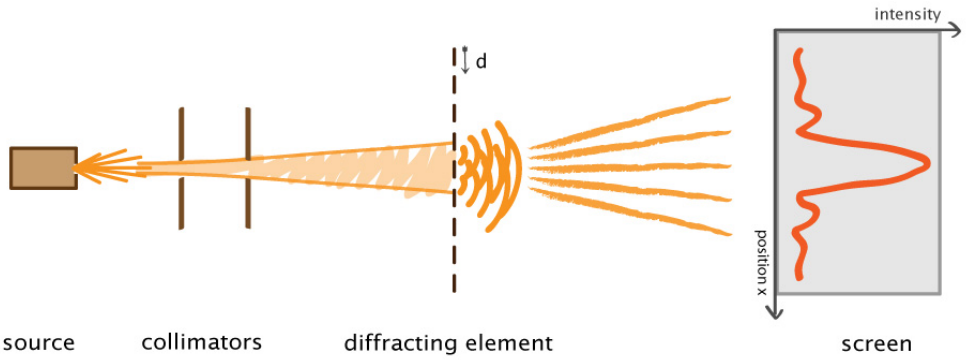

Figure 1.1: Sketch of a far-field diffraction experiment that demonstrates diffraction of a coherently delocalised matter-wave at a nanomechanical grating to produce a diffraction pattern at a detection screen. In order to seperate the diffraction orders, the screen has to be positioned at a certain distance from the grating (optical far-field). Furthermore, the beam has to be collimated in order to prevent diffraction orders from overlapping.

We start by considering the *Talbot effect* [Talbot, 1836], which is a near-field diffraction appearance of self-images emerging from a coherently illuminated periodic structure. In the context of wave mechanics, *coherence* is the well-defined relation of the wavelets that is required for interference. It has to be distinguished between *transverse coherence*, meaning the spatial connection, and *longitudinal coherence* for the link of the wavelets in time. In the case of Talbot diffraction the source has to allow for transversally coherent emission. The image of the diffraction grating of periodicity d_G is reconstructed at discrete multiples of the Talbot length l_T behind the lattice which follows from

$$l_T = \frac{d_G^2 \cdot n}{\lambda}. \tag{1.2}$$

This is indirectly proportional to the wavelength λ of the incident wave. Also at rational multiples of the Talbot length $z = \frac{m}{n} \cdot l_T$ with $n, m \in \mathbb{N}$ there are recurrences of the structure with a reduced periodicity $\frac{m}{n} \cdot d_G$. Subsequently a highly branched diffraction pattern is formed, often referred as "Talbot carpet" [Berry et al., 2001, Case et al., 2009].

The requirement of a spatially coherent beam can be circumvented when using the *Lau effect* [Lau, 1948]. It prepares coherent illumination from an incoherent source by virtue of a second grating. The first grid can be considered as equidistant parallel line

sources that emit cylindrical waves which evolve into extended coherent wave fronts because of Heisenberg's uncertainty principle [Jahns and Lohmann, 1979]. Hence, the incoming wave is prepared for Talbot diffraction at the second grating, even though the resulting self-images appear at larger distance with greater pattern period [Swanson and Leith, 1985]. Near-field diffraction at the second grating will be coherently imaged onto the plane of the last grid. The third grating provides a mask, which alternately transmits or blocks the interference signal according to its position when it is moved. With a detector behind it, the transferred particles can then be registered with high spatial resolution.

John Clauser proposed the first generalised (mechanical) Talbot-Lau interferometer which is capable of observing "small rocks and live viruses" [Clauser, 1997]. The first implementation of a Talbot-Lau interferometer for macromolecules was realised in Vienna and used three gold gratings (see Fig. (1.2)) of 550 nm thickness and 990 nm periodicity to observe interferences of C_{70} fullerenes [Brezger et al., 2002]. However, the disadvantages of nanomechanical masks became apparent. Beyond clogging, van der Waals interactions between the grating bars and the impinging objects introduce dispersive forces and cause the particles to experience an effectively reduced slit width [Hornberger et al., 2004]. Being affected by the potential that scales with r^{-3}, gratings of small openings will lead to vanishingly small interference contrast [Gerlich et al., 2007]. Thus, near-field interferometry demands thinner diffraction elements for manipulating larger molecules.

Based on the *Kapitza-Dirac effect* which proposes that electrons are diffracted at a standing light wave [Kapitza and Dirac, 1933], which was observed for the first time through [Freimund et al., 2001], a retroreflected laser beam can be used as an optical grating [Gould et al., 1986, Nairz et al., 2001]. To circumvent molecule-wall interactions that reduce the interference contrast, the Talbot-Lau scheme is improved by replacing the second grating with a standing light wave inside the interferometer, introducing the KDTLI [Gerlich et al., 2007, Eibenberger et al., 2013].

Further advancements resulted in the setup of a Talbot-Lau interferometer in the time-domain, the OTIMA interferometer that makes use of three pulsed laser gratings (see Fig. (1.3)). Thereby the Talbot length l_T is substituted by the *Talbot time* t_T

$$t_T = \frac{l_T}{v} = \frac{m d_G^2}{h} \tag{1.3}$$

where m denotes the particles' mass. When a pulsed bunch of molecular clusters

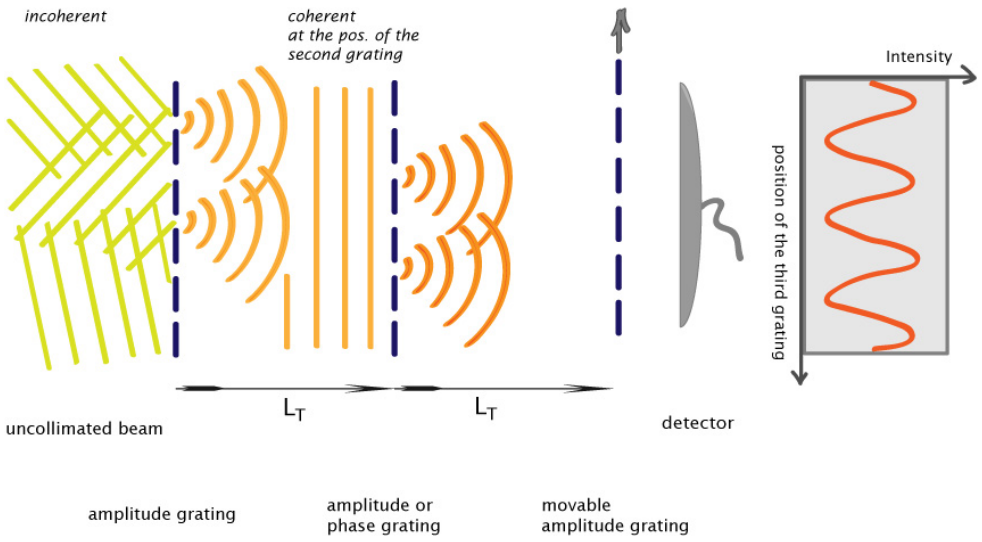

Figure 1.2: A sketch of a Talbot-Lau interferometer setup consisting of three identical gratings. The first grating, illuminated by an uncollimated molecular beam, prepares the coherence for the following diffraction grating. With the third, movable grating, a periodic pattern in the molecular distribution can be detected even if the detector itself is not position sensitive.

propagates parallel to the surface of a flat mirror the particle cloud is irradiated by a vacuum ultraviolet (VUV) laser pulse (8 ns) of 157 nm wavelength at times $t_0 = 0$, $t_1 = t_T$ and $t_2 = 2t_T$. The laser beam is retroreflected and a standing light wave is formed. It acts as the diffraction grating with a period of $d_G = \lambda/2$.

Using particles that have a high single-photon ionisation probability at the given wavelength, those molecules are most likely to be ionised passing the antinodes of the standing wave. The charged particles can then be extracted from the molecular beam with a constant electric field, leaving only neutral molecules traversing the nodes. The absorptive optical mask at t_0 thus prepares the transversal coherence of the molecular beam. After one Talbot time, at t_1 diffraction is realised by the second grating pulse, while the interference signal is probed by the following third laser pulse at t_2. An exhaustive theoretical treatment can be found in references [Haslinger, 2013, Haslinger et al., 2013, Nimmrichter et al., 2011a].

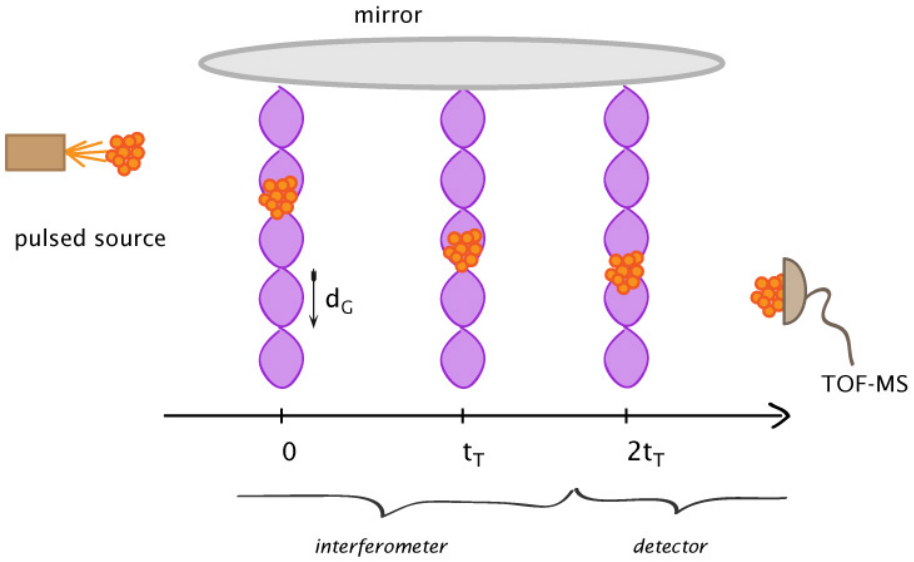

Figure 1.3: A sketch of the OTIMA interferometer concept. A pulsed source emits a particle cloud whose coherence is prepared by the first standing wave at t_0. With the second light grating at the Talbot time t_T the particles get diffracted, while the third one is used to scan the resulting interference signal. In turn, the detection is performed by measuring the post-ionised particles in a time-of-flight mass-spectrometer (TOF-MS).

Source requirements

In KDTLI, the use of an optical grating calls for the constraint on the molecular beam divergence. Since particles hitting the laser grating will be transmitted at 100%, there is a certain proportion that objects with inclined trajectory will cross different phase angles of the standing wave. Thus, the action of the optical potential can be averaged out. The collimation of the molecular beam is therefore determined by the upper limit for both the angle of incidence and the divergence with

$$\Delta\alpha < \arctan\left(\frac{\lambda_{\text{laser}}}{2 \cdot 2w_{\text{laser}}}\right) \simeq 4 \text{ mrad} \tag{1.4}$$

where the thickness w_{laser} of the laser beam is estimated for the 532 nm continuous-wave (CW) laser to be around 30 μm [Gerlich, 2011].

In order to achieve high contrast in OTIMA interferometry a particle also should not average over the nodes and anti-nodes of the standing wave during the laser pulse, Fig. (1.4). The distance for a particle passing inside the standing wave is determined by the

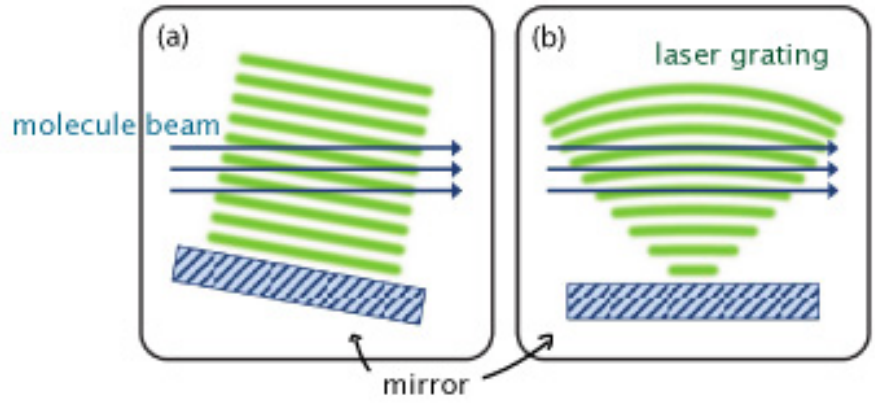

Figure 1.4: An illustration of molecules being exposed to the standing light wave. The molecule beam in (a) crosses several nodal planes due to misalignment of the laser grating. In (b) the effect of a finite wavefront curvature is shown, which causes molecules to pass different phase angles of the standing light wave. In both cases the action of the optical potential will be averaged out. Figure adapted from [Gerlich, 2011].

pulse length τ_{pulse} and the velocity of the particles v. The maximum distance travelled by the particle within the optical potential can be estimated from the effective width of the laser pulse by $w_{\text{eff}} = v \cdot \tau_{\text{pulse}}$. For a molecule with a velocity of $v_{\text{long}} = 10^3$ m/s and a laser pulse of 8 ns duration, the effective laser width would be 8 μm. With this and the relation derived in Eq. 1.4 the limitation on the divergence angle $\Delta\alpha$ of the molecular beam can be calculated to

$$\Delta\alpha < \arctan\left(\frac{\lambda_{\text{laser}}}{4 \cdot w_{\text{eff}}}\right) \simeq 10 \text{ mrad}. \tag{1.5}$$

The diagram in Fig. (1.5) shows the maximal acceptable forward velocity in KDTLI and OTIMA as a function of the molecular mass m depending on the resolution of the interferometer.

$$v_{\text{max}} = \frac{h}{m \cdot \lambda_{\text{min}}}. \tag{1.6}$$

Here I have assumed minimal wavelengths of $\lambda_{\text{dB,min,KDTLI}} = 500$ fm for the KDTLI and $\lambda_{\text{dB,min,OTIMA}} = 200$ fm for the OTIMA. Future upgrades of both experiments may allow to decrease these values by another order of magnitude.

Cooling methods have also to be implemented that provide lower internal states of the molecular samples, reducing therewith a possible decoherence channel. Since

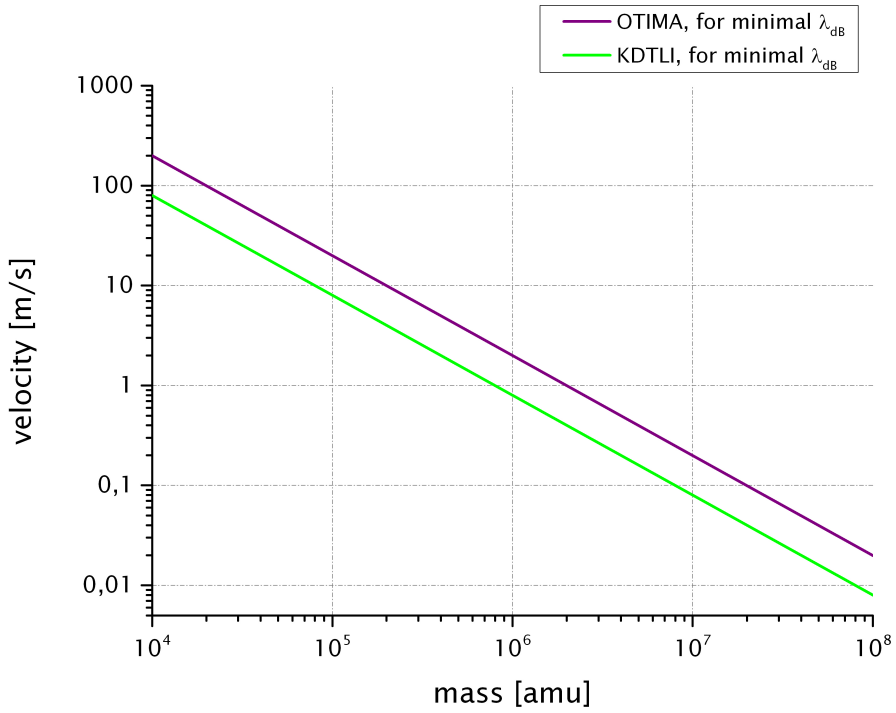

Figure 1.5: Maximal particle velocity accepted by OTIMA and KDTLI in their present implementation. The curves show Eq. 1.6 for the assumed wavelengths λ_{min}.

the environment consists of numerous interacting degrees of freedom, there are a huge number of possible channels of the interferring system to lose its coherence [Nimmrichter, 2013]. In practice, it is often enough for the complete decoherence of a quantum system, when it emits a single photon after thermal excitation (*thermal decoherence* in [Hackermüller et al., 2004]) or when it collides with a residual gas atom (*collisional decoherence* in [Hornberger et al., 2003]). Also mechanical disturbances can cause the vanishing of interference fringes. However, the reason for it are acoustic vibrations slightly moving the diffracting device, accomplishing the *phase averaging* of individual wavelets and the blurring of an interference pattern [Stibor et al., 2004].

Buffer-gas cooling in linear ion traps

Cooling the internal as well as external degrees of freedom of macromolecules can be achieved by implementing a buffer-gas cooling scheme [Gerlich, 1995, Wang et al., 2005, Mikosch et al., 2007]. Particles in a cold ion trap can be cooled to a few Kelvin [Ger-

lich, 2008a]. This may be implemented in future experiments to generate a source for internally cold and slow nanoparticles.

Ion traps are used in a wide range of fields, such as physical chemistry, quantum information, nuclear physics and biomolecular spectroscopy to name but a few [Makarov et al., 2006, Kielpinski et al., 2002, Herfurth, 2003, Antoine and Dugourd, 2011]. It originates in the *quadrupole mass filter*, which was invented in 1953 by Paul and Steinwedel [Paul and Steinwedel, 1953]. They laid the basis for linear ion traps [Prestage et al., 1989]. A Paul trap constrains and selects charged particles in space by combining a DC with a radio-frequency AC electric field applied to a system of electrodes, arranged to follow the hyperbolic quadrupole field pattern. As depicted in Fig. (1.6), the mass filter was designed to confine the ions only in two dimensions, while the *3D Paul trap* captures charged particles.

Ions moving in such an instrument experience the alternating attraction and repulsion towards the electrodes, performing complex trajectories within the restricted space. Provided that an additional static electrical current is applied at the ends of the quadrupole filter, the ions can also be trapped (*"linear ion trap"*). In combination with a buffer-gas cooling technique ion clouds can be stably stored allowing for many different kind of experiments, e.g. action spectroscopy [Bian et al., 2010], formation and photodepletion of clusters [Brümmer et al., 2003] or ion mobility measurements [Uetrecht et al., 2010]. Many applications can be found in quantum information experiments [Monroe et al., 1995, Steane, 1997, Gulde et al., 2003, Chiaverini et al., 2005, Home et al., 2009] as well as in cold chemistry implementations [Willitsch et al., 2008a, Willitsch et al., 2008b]. Several groups realised laser-cooling of atoms [Mø lhave and Drewsen, 2000, Morigi et al., 2000] in traps. Moreover, the Collision-induced Dissociation (CID) technique in biomolecular physics also relies on ion trap setups [Yinon et al., 1997, Larsen et al., 2001, Demelbauer et al., 2004, Hogan et al., 2005]. Further applications of cold ion traps are used in laboratory astrophysics [Asvany et al., 2004, Snow and Bierbaum, 2008].

The development of a cryogenic linear ion trap, as in [Poitzsch et al., 1996, Okada and Wada, 2001, Schwarz et al., 2012], is of particular interest for this work, as it allows to prepare cold and dense samples of macromolecules. The up-coming chapters introduce the theoretical description of linear ion traps, give an overview of relevant trapping properties and cooling schemes, as well as considerations in relation to matter-wave

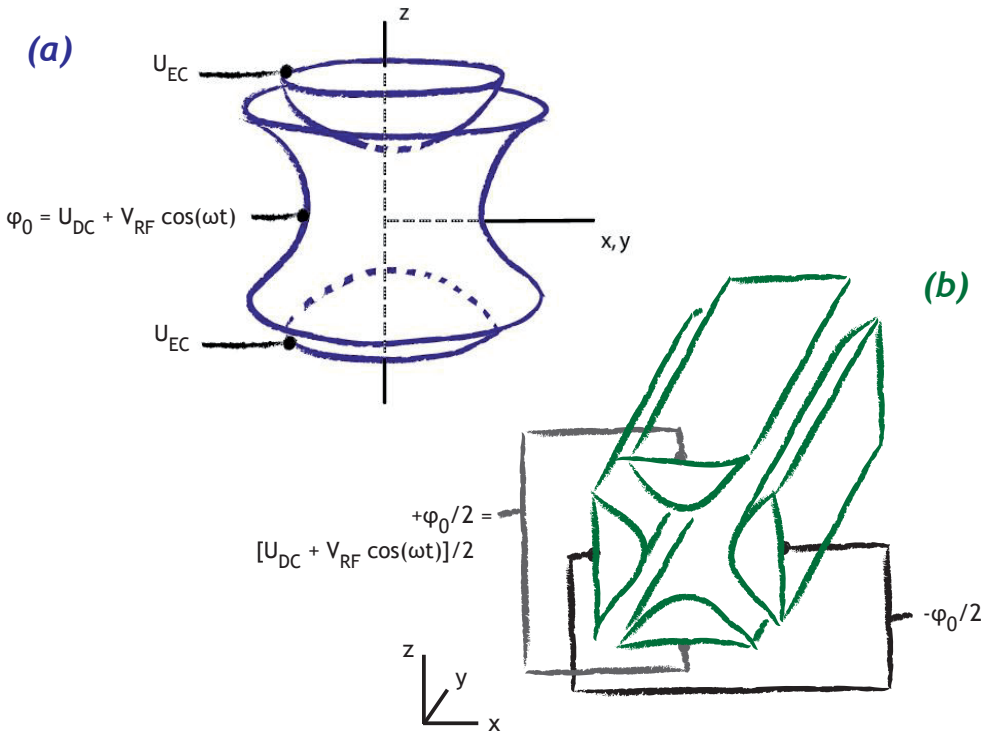

Figure 1.6: A sketch of the three-dimensional Paul trap, drawn in blue (a), and the quadrupole mass filter, drawn in green (b). The Paul trap consists of a ring-electrode with top and bottom caps of hyperbolic cross-section, following the quadrupole potential that confines charged particles in every spatial dimension. The quadrupole mass filter is composed of four elongated electrodes with hyperbolic cross-section as well, which are symmetrically arranged around an imaginary circle. Ions affected by the two-dimensional quadrupole potential will only be radially constrained.

interferometry. The conceived design of a cold ion trap system for massive molecular beams will be presented, which is subsequently simulated regarding its feasibility and cooling performance. Besides, experimental tests on a cryogenic setup are demonstrated, treating the requirements on low-temperature applications. Lastly, I will give an outlook on possible realisations of interference experiments with the discussed trapping system.

Chapter 2

Ion Trap Theory

2.1 Fundamental physics of ions in electromagnetic fields

In order to understand the motion of charged particles in oscillatory electric fields, particularly with regard to the subsequent discussion of multipole fields, a rather general treatment is presented, following [Friedman, 1982, Gerlich, 1992].

An ion carrying the charge e experiences the Lorentz force F when it traverses an electric field $\boldsymbol{\mathcal{E}}$ and magnetic field $\boldsymbol{\mathcal{B}}$

$$\mathsf{F} = e\left(\boldsymbol{\mathcal{E}} + \mathsf{v} \times \boldsymbol{\mathcal{B}}\right). \tag{2.1}$$

With Newton's law of motion the equations of motion of the ion can be derived from the Lorentz force (Eq. 2.1)

$$\mathsf{F} = m\frac{d^2\mathbf{r}}{dt^2} \tag{2.2}$$

In vacuum without free charges and no current densities the Maxwell equations read

$$\begin{aligned} \nabla \cdot \boldsymbol{\mathcal{E}} &= 0 & \nabla \times \boldsymbol{\mathcal{E}} &= -\frac{\partial \boldsymbol{\mathcal{B}}}{\partial t} \\ \nabla \cdot \boldsymbol{\mathcal{B}} &= 0 & \nabla \times \frac{1}{\mu_0}\boldsymbol{\mathcal{B}} &= \frac{\partial\left(\varepsilon_0 \boldsymbol{\mathcal{E}}\right)}{\partial t} \end{aligned} \tag{2.3}$$

where ε_0 is the vacuum permittivity and μ_0 is the permeability of free space.

In the case of electrical confinement in a Paul trap, a quasi-stationary electric field will be regarded, where induced magnetic fields are negligible. Therefore, it is sufficient

to use

$$\nabla \cdot \boldsymbol{\mathcal{E}} = 0 \qquad \nabla \times \boldsymbol{\mathcal{E}} = 0. \tag{2.4}$$

where the vector field $\boldsymbol{\mathcal{E}}$ can be derived from the divergence of the scalar potential φ

$$\boldsymbol{\mathcal{E}} = -\nabla \varphi (x, y, z) . \tag{2.5}$$

Hence, Newton's law of motion can be expressed as

$$\mathsf{F} = m\ddot{\mathbf{r}} = -e\nabla \varphi (x, y, z) . \tag{2.6}$$

2.1.1 Adiabatic approximation

We consider an ion[1] in a weak electric field, where the particle velocity is slow compared to the velocity of light. This quasistationary electric field $\boldsymbol{\mathcal{E}} (\mathbf{r}, t)$ is composed of a static $\boldsymbol{\mathcal{E}}_s (\mathbf{r})$ and a time-dependent electric field $\boldsymbol{\mathcal{E}}_0 (\mathbf{r}) \cos (\omega t + \delta)$, where the equation of motion can be set by

$$m\ddot{\mathbf{r}} = q\boldsymbol{\mathcal{E}}_0 (\mathbf{r}) \cos (\omega t + \delta) + q\boldsymbol{\mathcal{E}}_\mathrm{s} (\mathbf{r}) \tag{2.7}$$

where ω is the angular frequency, q is the electric charge and δ the phase of the oscillating field.

We chose with respect to the following derivation the electrostatic field as well as the phase of the oscillating field to be zero, thus $\boldsymbol{\mathcal{E}}_\mathrm{s} = 0$ and $\delta = 0$. In the case of a homogeneous field, $\boldsymbol{\mathcal{E}}_0$ is independent of $\mathbf{r}$ and the solution of the differential equation leads to a stationary oscillation with an amplitude that is inversely proportional of the mass and to the square of the frequency. Thus, the following Ansatz can be used

$$\mathbf{r} (t) = \mathbf{r} (0) - \cos (\omega t) \qquad \mathsf{A} = \frac{q\boldsymbol{\mathcal{E}}_0}{m\omega^2} \tag{2.8}$$

where A is the amplitude of the oscillation.

However, when operating electrodes differ (even slightly) from the ideal geometry, the electric field will become inhomogeneous. For a weakly inhomogeneous field, the amplitude is nearly unperturbed, while the charge would continuously adapt to the varying strength of the field, e.g. resulting in being slowly drawn outwards the electrical confinement.

[1] In the following "ion" will simply refer to a charged particle, if necessary the polarity will be specified.

2.1.2 The effective potential

The motion of an ion in an inhomogeneous radio-frequency field can be approximated by the assumption, that the field varies slowly as a function of the coordinate $\mathbf{r}$ and has a high frequency that keeps the amplitude $\mathbf{A}$ small (quasistatic motion). A solution of the equation of motion in Eq. (2.7) can be constructed by superimposing a slow drift $\mathbf{r}_{\mathrm{sec}}(t)$ (also called the *"macro- or secular motion"*) and a rapidly oscillating motion $\mathbf{r}_{\mathrm{mic}}(t)$ (the *"micromotion"*):

$$\mathbf{r}(t) = \mathbf{r}_{\mathrm{sec}}(t) + \mathbf{r}_{\mathrm{mic}}(t) \tag{2.9}$$

with

$$\mathbf{r}_{\mathrm{mic}}(t) = -\mathbf{a}(t)\cos\omega t. \tag{2.10}$$

We seek to solve Eq. (2.7) with this approximation by regarding only slow time variations in $\mathbf{A}$ and $\boldsymbol{\mathcal{E}}_0$. Calculations yield the differential equation for the non-oscillating motion $\mathbf{r}_{\mathrm{sec}}(t)$

$$m\ddot{\mathbf{r}}_{\mathrm{sec}} = -\frac{q^2}{4m\omega^2}\nabla\boldsymbol{\mathcal{E}}_0^2(\mathbf{r}_{\mathrm{sec}}) \tag{2.11}$$

which shows that an ion experiences a force caused by the inhomogeneity of the field, the *gradient force*. In addition, the relation indicates that charged particles will be pushed into regions of weak field strengths.

With Eq. (2.11) the time-invariant mechanical potential Φ_{eff}

$$\Phi_{\mathrm{eff}}(\mathbf{r}_{\mathrm{sec}}) = \frac{q^2\boldsymbol{\mathcal{E}}_0^2(\mathbf{r}_{\mathrm{sec}})}{4m\omega^2} + q\varphi_s(\mathbf{r}_{\mathrm{sec}}) \tag{2.12}$$

also known as the *effective* or *(pseudo)potential*. Thereby the smooth motion of a charged particle in an inhomogeneous oscillating potential can be derived from

$$m\ddot{\mathbf{r}}_{\mathrm{sec}} = -\nabla\Phi_{\mathrm{eff}}(\mathbf{r}_{\mathrm{sec}}). \tag{2.13}$$

To demonstrate the effect of the pseudopotential on a particle in the Paul trap and its dynamic stabilisation, a mechanical analogue device is shown in Fig. (2.1).

Integrating the relation Eq. (2.13) leads to the total energy E_{m}

$$\frac{1}{2}m\dot{\mathbf{r}}_{\mathrm{sec}}^2 + \frac{q^2\boldsymbol{\mathcal{E}}_0^2(\mathbf{r}_{\mathrm{sec}})}{4m\omega^2} + q\varphi_s(\mathbf{r}_{\mathrm{sec}}) = E_{\mathrm{m}}(\mathbf{r}_{\mathrm{sec}}) \tag{2.14}$$

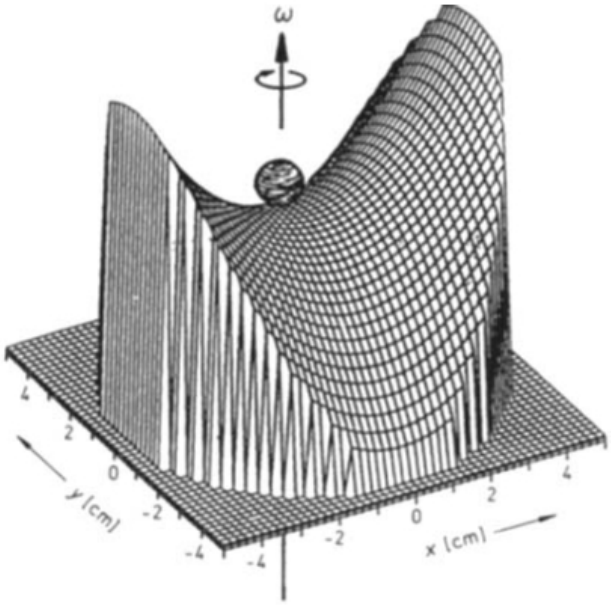

Figure 2.1: Mechanical analogon for the pseudopotential of the Paul trap. The model demonstrates dynamic stabilisation in the trap, where the equipotential lines form a saddle surface and the particle is represented by a ball. If the saddle rotates with the right frequency approprate to the potential parameters and mass of the ball, the ball stably oscillates on top of the surface. Figure taken from [Paul, 1990].

the adiabatic constant of ion motion. The ions experience a consecutive exchange between the involved forms of energy, the kinetic energies of the secular motion $1/2m\dot{r}^2_{sec}$, micromotion $1/2m\dot{r}^2_{mic}$ and the static potential energy $q\varphi_s$.

2.2 Confinement in a multipole ion trap

A setup with 2n ($n \in \mathbb{N}$) poles (e.g. rod-like electrodes) around a circle of radius r_0 composes a two-dimensional multipole ion guide. It is convenient to use cylindrical coordinates to describe the potential of the multipole[2].

[2]From now on the term "multipole" will be used as an abbrevation for both multipole ion guide and multipole ion trap.

Considering infinitely long cylindrical conductors the potential simplifies to

$$\varphi_n(r,\phi) = \varphi_0 \left(\frac{r}{r_0}\right)^n \cos(n\phi), \tag{2.15}$$

where φ_0 is the applied potential and r_0 is the trap radius [Gerlich, 1992, Ghosh, 1995]. For the applied voltage φ_0 we use the general form of

$$\varphi_0 = U_{\mathrm{DC}} - V_{\mathrm{RF}} \cos(\omega t), \tag{2.16}$$

where U_{DC} is the static (DC) field, V_{RF} is the amplitude of the radio-frequency (RF) field. The potential at two adjacent electrodes are $+\varphi_0$ and $-\varphi_0$.

The gradient of the potential φ furnishes the polar components of the electric field

$$\boldsymbol{\mathcal{E}} = \left(\mathcal{E}_r, \mathcal{E}_\phi\right) = -\left(\frac{\partial}{\partial r}\varphi, \frac{1}{r}\frac{\partial}{\partial \phi}\varphi\right) = \frac{\varphi_0}{r_0} n \left(\frac{r}{r_0}\right)^{n-1} (-\cos n\phi, \sin n\phi). \tag{2.17}$$

If we use the Cartesian representation of the electric field,

$$\left(\mathcal{E}_x, \mathcal{E}_y\right) = \frac{\varphi_0}{r_0} n \left(\frac{r}{r_0}\right)^{n-1} (-\cos(n-1)\,\phi, \sin(n-1)\,\phi), \tag{2.18}$$

and replace φ_0 by the relation in Eq. (2.16), we obtain the equations of motion in Cartesian coordinates

$$\ddot{x} + \frac{q}{m}\left[\frac{\varphi_0}{r_0} n \left(\frac{r}{r_0}\right)^{n-1} \cos((n-1)\phi)\right] = 0 \tag{2.19}$$

$$\ddot{y} - \frac{q}{m}\left[\frac{\varphi_0}{r_0} n \left(\frac{r}{r_0}\right)^{n-1} \sin((n-1)\phi)\right] = 0 \tag{2.20}$$

which are non-linear and coupled differential equations for $n > 2$. However, in the case of $n = 2$ the equations are linear and reduce to Eq. (2.28) and Eq. (2.29).

The absolute value of the amplitude of the RF field

$$|\boldsymbol{\mathcal{E}}_0| = \frac{V_{\mathrm{rf}}}{r_0} n \left(\frac{r}{r_0}\right)^{n-1} \tag{2.21}$$

and the static multipole potential φ_s

$$\varphi_s = q U_{\mathrm{DC}} \left(\frac{r}{r_0}\right)^{n-1} \cos n\Phi \tag{2.22}$$

are inserted into Eq. (2.12). Thus, the representation of the effective potential for a multipole of the n-th order is

$$\Phi_{\text{eff}}(r) = \frac{n^2 q^2 V_{\text{rf}}^2}{4 m r_0^2 \omega^2} \left(\frac{r}{r_0}\right)^{2n-2} + q\, U_{\text{dc}} \left(\frac{r}{r_0}\right)^{n} \cos(n\phi)\,. \tag{2.23}$$

If the static field is omitted, the multipole operates in the "RF-only" mode where the effective potential reduces to

$$\Phi_{\text{eff}}(r) = \frac{n^2 q^2 V_{\text{rf}}^2}{4 m r_0^2 \omega^2} \left(\frac{r}{r_0}\right)^{2n-2}. \tag{2.24}$$

In my work, I will describe only radio-frequency driven ion traps of multipole orders relevant to further discussion. The effective potentials of several multipole configurations of different order are shown in Fig. (2.2).

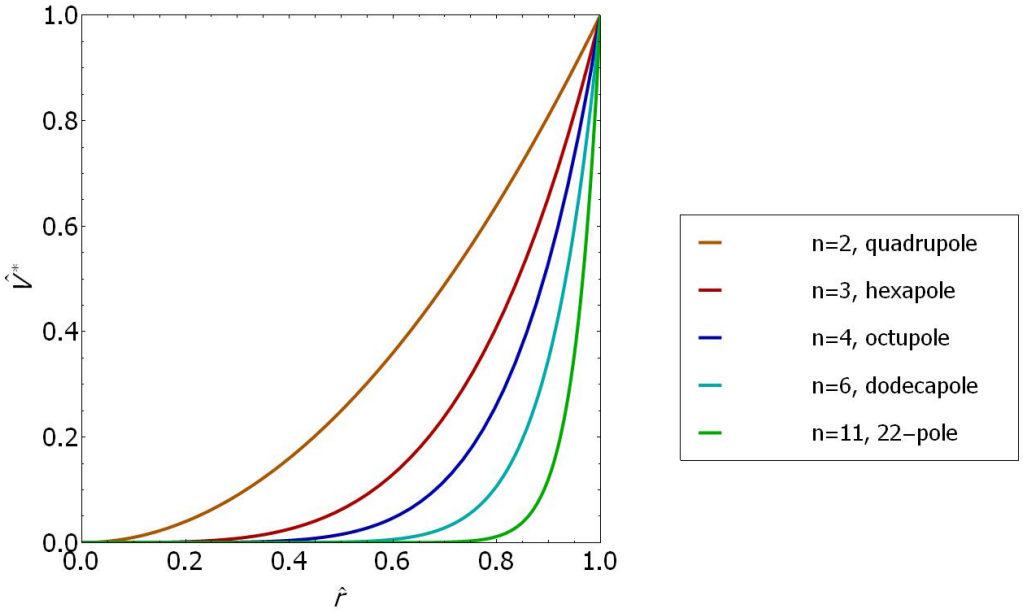

Figure 2.2: Comparison of the shapes of the effective potentials for multipoles of order n = 2, 3, 4, 6, 11. With increasing pole order the potential gets steeper.

2.2.1 The linear quadrupole field

Let's start by treating the two-dimensional quadrupole field ($n = 2$, cf. Eq. (2.15)),

$$\varphi_2(r, \phi) = \varphi_0 \left(\frac{r}{r_0}\right)^2 \cos(2\phi) \tag{2.25}$$

or in Cartesian coordinates

$$\varphi(x, y) = \frac{\varphi_0}{2r_0{}^2}\left(x^2 - y^2\right). \tag{2.26}$$

The corresponding equipotential lines generated are depicted in Fig. (2.3).

The potential can be realised with four equally shaped hyperbolic electrodes by applying a voltage of $\pm\varphi_0/2$ to one pair of opposite electrodes. In practice, rods of circular cross section are generally used, since the quadrupole field is well approximated at the surface of the round electrodes [Denison, 1971], even though at high resolution field distortions of sixth- and tenth-order may introduce precursor peaks to the mass spectrum [Dawson, 1970].

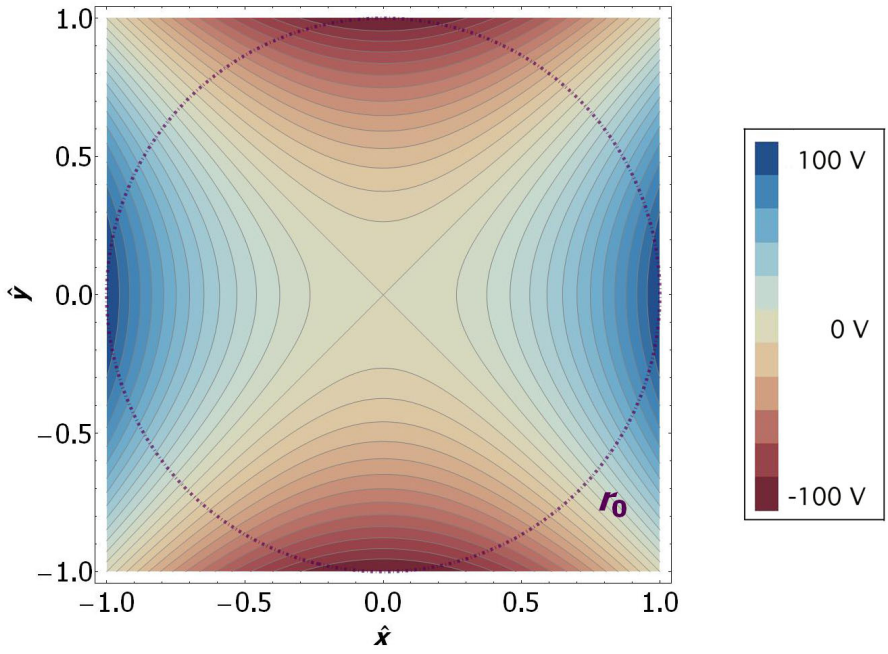

Figure 2.3: The quadrupole geometry. The equipotential surfaces emanate from $2n = 4$ symmetrically arranged electrodes with an inscribed radius of r_0 (broken line). The contours of the plot follow the potential given by Eq. (2.27), where an amplitude of $\varphi_0 = 100V$ has been assumed. The length scales $\hat{x}$, $\hat{y}$ are normalised. The color shading indicates the varying strength of the electrical field.

If the quadrupole field is created by a static DC voltage U_{DC} and a radio-frequency

voltage with an angular frequency of ω, the quadrupole potential has the form

$$\varphi(x, y, t) = (U_{DC} - V_{RF} \cos \omega t) \frac{x^2 - y^2}{2{r_0}^2}. \tag{2.27}$$

The associated equations of motion for a particle of mass m and charge e are given by

$$\ddot{x} + \frac{e}{m{r_0}^2} (U_{DC} - V_{RF} \cos \omega t)\, x = 0 \tag{2.28}$$

$$\ddot{y} - \frac{e}{m{r_0}^2} (U_{DC} - V_{RF} \cos \omega t)\, y = 0 \tag{2.29}$$

as introduced in [Ghosh, 1995].

Substituting in Eq. (2.28) and Eq. (2.29) with the following relations

$$\frac{4eU_{DC}}{mr_0^2\omega^2} =: a_M \quad \frac{2eV_{RF}}{mr_0^2\omega^2} =: q_M \quad \text{and} \quad \omega t =: 2\zeta \tag{2.30}$$

we obtain the Mathieu differential equations

$$\frac{d^2x}{d\zeta^2} + (a_M - 2q_M \cos 2\zeta)\, x = 0 \tag{2.31}$$

$$\frac{d^2y}{d\zeta^2} - (a_M - 2q_M \cos 2\zeta)\, y = 0 \tag{2.32}$$

which can be solved analytically.

Depending on the values of the parameters a_M and q_M the Mathieu equations lead to stable or unstable ion motion. A diagram can be made showing para- meter regions of stable motion in a certain direction (see Fig. (2.4), (a)). Since the only difference between Eq. (2.31) and Eq. (2.32) is the sign, the stability diagrams are mirrored about the q_M-axis (Fig. (2.4), (b)).

Stability has to be ensured in both the x- and in the y-direction. The corresponding zones overlap for small value ranges of a_M and q_M (Fig. (2.5), (a)). Usually low, positive values of a_M, q_M are used. Beyond the stable set of a_M/q_M ratio (i.e. $U_{DC}/V_{RF} = \text{const.}$), the ion trajectories become unstable and the ions will escape from the trap.

For fixed values of ω and r_0, and for a given amplitude V_{RF}, the q_M-value (2.30) can have a lower bound $q_{M,low}$ corresponding to an upper bound on (m/e), as well as $q_{M,high}$ associates with a lower bound on (m/e) (Fig.2.5(b)). Therefore only ions with (m/e)

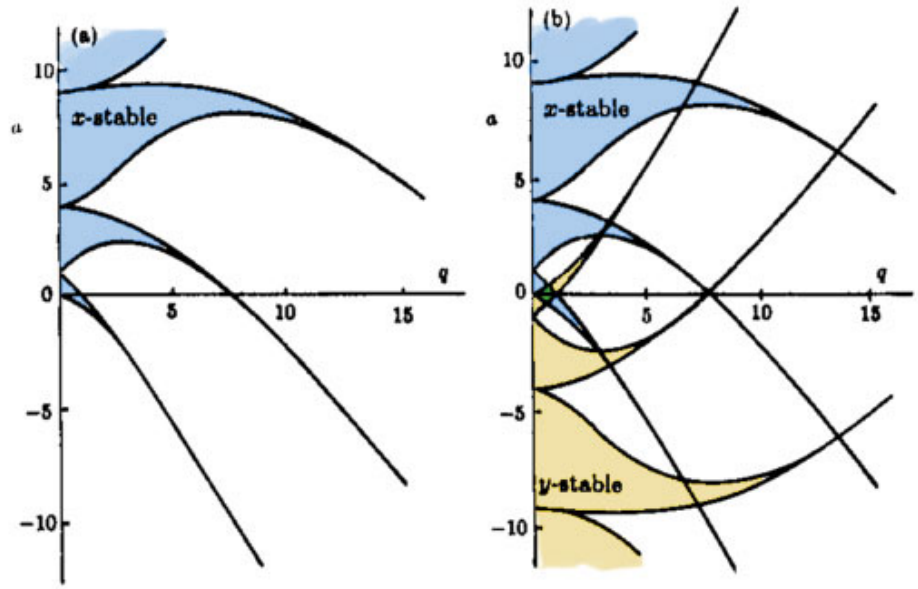

Figure 2.4: Stability diagram for the two-dimensional quadrupole field: (a) for x-motion, (b) for x- and y-motion. Figure adapted from [Ghosh, 1995].

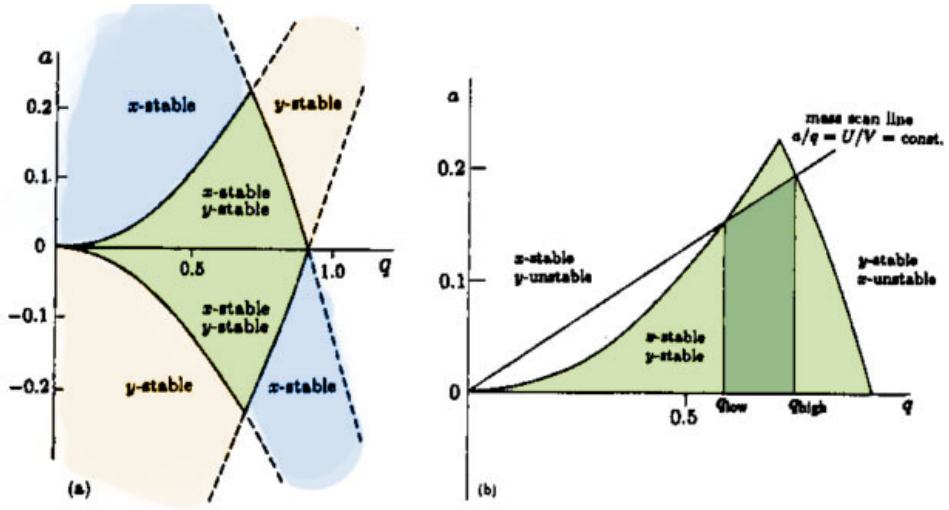

Figure 2.5: The lowest stability region (a) also in detail showing a mass scan line (b). Figure adapted from [Ghosh, 1995].

values within those bounds will be stably guided. Consequently, a given amplitude of the radio-frequency field V_{RF} constrains a $\Delta(m/e)$ spread around a specific mass-to-charge ratio, rejecting all particles that do not fit the chosen working range.

2.2.2 The hexapole field

Already with $n = 3$ the corresponding multipole potential

$$\varphi_3(r, \phi) = \varphi_0 \left(\frac{r}{r_0}\right)^3 \cos(3\phi) \tag{2.33}$$

leads to non-linear equations of motion. In Cartesian coordinates the x- and y-components of the potential are coupled

$$\varphi(x, y) = \frac{\varphi_0}{2r_0^3}\left(x^3 - 3xy^2\right). \tag{2.34}$$

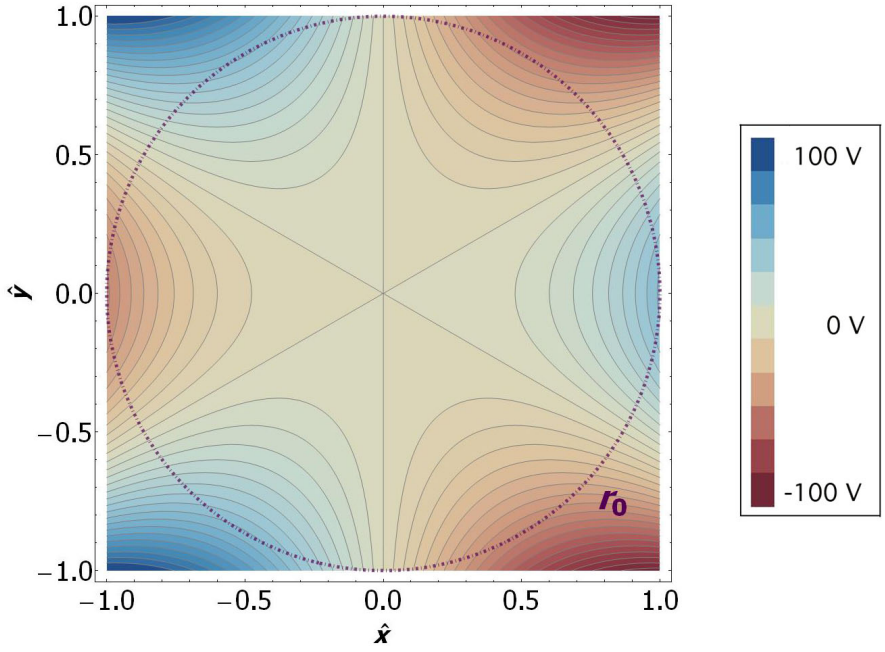

Figure 2.6: The hexapole geometry. The equipotential surfaces emanate from $2n = 6$ symmetrically arranged electrodes with an inscribed radius of r_0 (broken line). The amplitude was assumed to be $\varphi_0 = 100V$. The length scales $\hat{x}$, $\hat{y}$ are normalised. The color shading indicates the varying strength of the electrical field.

In comparison to the quadrupole field, the hexapole arrangement leads already to a wider low field region between the electrodes (see the equipotential lines in Fig. (2.6)). Since the ion cloud is still confined around the axis, a hexapole is often used as an ion guide in mass spectrometry [Douglas et al., 2005]. As will be seen in chapter 3, a hexapole can serve in the transfer and precooling of charged particles.

2.2.3 The dodecapole field

To provide more space for the ions to propagate conservatively, while the restraining potential should not be excessively steep letting particles to the vicinity of the electrodes, we considered a multipole of the order of $n = 6$ with

$$\varphi_6(r, \phi) = \varphi_0 \left(\frac{r}{r_0} \right)^6 \cos(6\phi) . \tag{2.35}$$

The potential $\varphi(x, y)$ of the dodecapole can be written as

$$\varphi(x, y) = \frac{\varphi_0}{2r_0^6} \left(x^6 - 15x^4y^2 + 15x^2y^4 - y^6 \right) \tag{2.36}$$

which leads to the equipotential diagram in Fig. (2.7).

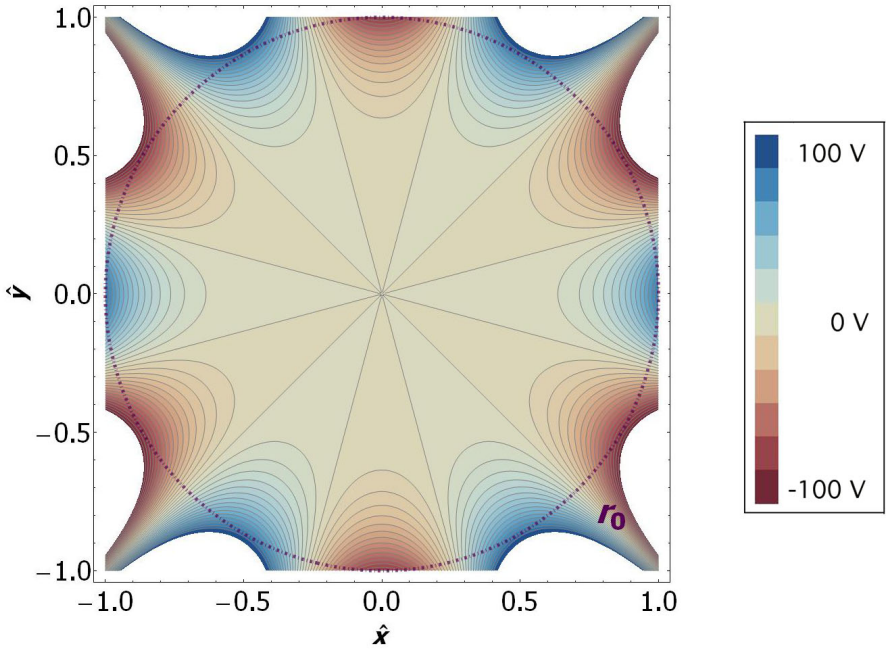

Figure 2.7: The dodecapole geometry. The equipotential surfaces emanate from $2n = 12$ symmetrically arranged electrodes with an inscribed radius of r_0 (broken line). The amplitude was assumed to be $\varphi_0 = 100V$. The length scales $\hat{x}$, $\hat{y}$ are normalised. The color shading indicates the varying strength of the electrical field.

2.2.4 The adiabaticity parameter

A continuously driven oscillation can augment the particle energy until nonadiabatic and unstable motion occurs. Therefore the effective potential approximation looses

its applicability. A stability criterion analogous to Fig. (2.5) cannot be extended to the ion motion in a general multipole field. The related equations of motion become nonlinear and couple different spatial components (see Sec. (2.2.1)). Several works described stable working ranges for specific multipole setups [Friedman, 1982, Hägg and Szabo, 1986], and attempted to define a_M, q_M-like parameters. However, Gerlich argued [Gerlich, 1992], that a rigorous characterisation of stability is not possible in multipole fields, since the initial conditions always determine the ion motion.

Yet, stable operating conditions can be assigned to a multipole arrangement, if one regards the range of validity of the effective potential approximation. In order for the ions to behave adiabatically, the approximations allow only slow changes over time. Quantifying this requirement, it is convenient to introduce a dimensionless parameter. One defintion is based on the assumption of a slow spatial variation of the electric field, as used in the derivation of the effective potential. The change of the field has to be smaller than the field amplitude over the distance passed per one oscillation period, where $2\mathbf{A}$ is in the sense of Eq. (2.8):

$$|2\,(\mathbf{A}\nabla)\,\boldsymbol{\mathcal{E}}_0| < |\boldsymbol{\mathcal{E}}_0|. \tag{2.37}$$

Teloy and Gerlich [Teloy and Gerlich, 1974, Gerlich, 1986] set the ratio to be the function $\eta\,(\mathbf{r})$

$$\eta\,(\mathbf{r}) = \frac{|2\,(\mathbf{A}\nabla)\,\boldsymbol{\mathcal{E}}_0|}{|\boldsymbol{\mathcal{E}}_0|} \ll 1 \tag{2.38}$$

that depends on the spatial coordinate $\mathbf{r}$ of the ion movement.

Using Eq. (2.8) and simplifying it with a basic vector analysis identity leads to the definition of the *adiabaticity parameter*

$$\eta\,(\mathbf{r}) = \frac{2q|\nabla\boldsymbol{\mathcal{E}}_0|}{m\omega^2}. \tag{2.39}$$

For a certain mass-to-charge ratio m/q and frequency ω of the field, the parameter η depends only on the inhomogeneity of the quasistatic field $\boldsymbol{\mathcal{E}}_0$. As a consequence thereof, if η is too high, the field is rather inhomogeneous leading to an increasingly unstable motion of the ions. For practical applications, an empirical limit for η was derived to be

$$\eta_m < 0.3. \tag{2.40}$$

where the subscript m indicates the maximum tolerable limit for the adibaticity parameter. There is still a probability to encounter unstable regions below $\eta < 0.3$, since this value is based on numerical simulations and experiments rather than a strict mathematical proof.

For the specific arrangement of the multipole it can be written as

$$\eta = 2n\,(n-1)\,\frac{q\,V_{\mathrm{RF}}}{m\,\omega^2 r_0^2}\left(\frac{r}{r_0}\right)^{n-2} \tag{2.41}$$

and stable multipole trapping can be achieved for

$$\begin{aligned} \frac{r}{r_0} &< 0.8 \\ \eta &< 0.3 \end{aligned} \tag{2.42}$$

where ion trajectories r/r_0 within the multipole should not exceed the intrinsic electrode arrangement to remain bound [Gerlich, 1992].

2.3 Heating effects

The translational energy is continuously exchanged between the micro- and the secular motion of the ions. If the ion movement is disturbed inside the radio-frequency field, as for example with collisions, some of the kinetic energy of the RF-driven micromotion will be scattered incoherently into the secular motion. The particles may experience *RF heating*, the increase of the translational energy and therefore the temperature of the ions [Moore, 2002].

The total kinetic energy composed of both translational modes is

$$E_{\mathrm{kin}}\,(t) = \frac{1}{2}m\left[\dot{\mathbf{r}}_{\mathrm{sec}}\,(t) + \dot{\mathbf{r}}_{\mathrm{mic}}\,(t)\right]^2 \tag{2.43}$$

where the slow $\mathbf{r}_{\mathrm{sec}}$ and radio-frequent $\mathbf{r}_{\mathrm{mic}}$ translational components are assumed to run in parallel. With the relations in Eq. (2.14) and substituting the effective potential Φ_{eff} in the kinetic energy of the oscillatory motion $\frac{1}{2}m\dot{r}_{\mathrm{sec}}^2 = 2\Phi_{\mathrm{eff}}\sin^2\omega t$, the total kinetic energy calculates to

$$E_{\mathrm{kin}}\,(t) = \left[\left(E_m - \Phi_{\mathrm{eff}}\right)^{1/2} + \left(2\Phi_{\mathrm{eff}}\right)^{1/2}\sin\omega t\right]^2 \tag{2.44}$$

with E_m being the initial kinetic energy before entering the effective potential. Particles moving in the nearly field-free region of the trap have a total kinetic energy identical to E_m while undergoing one complete round-trip inside the trap, E_{kin} ranges between 0 and maximally $3E_m$. Numerical simulations [Gerlich, 1992] showed that the forces caused by the fast oscillating field have a negligible effect on the energy distributions of a buffer-gas cooled ensemble as long as the working conditions for the adiabatic approximation is satisfied.

In practice, parasitic low frequency fields may penetrate and lead to the acceleration of ions. The translational modes of the trapped ions are further subject to distortions through collisions with residual or buffer-gas particles. Inside the field-free region the ions thermalise through energy exchange with a cold gas (see Sec. (2.5.3)). But if collisions occur within the RF field, the energy between the ion and the RF field can not be exchanged adiabatically. Moreover, excitations due to imperfections in the confining field, such as for instance caused by surface patch effects (i.e. local distortions of the electrode work function) are a heating channel. As discussed in [Gerlich, 1992], local deviations from the average surface potential can be as small as ±100 mV and yet attract ions into high-field regions, causing them to heat.

2.4 Charge density and Coulomb repulsion

The density of charges is primarily limited due to the Coulomb repulsion. Additionally, dissipative mechanism like RF heating and collisions with ions or residual gas molecules can restrain the charge storage capability of the trap.

Assuming that ions are regularly distributed within the trap we expect a particle cloud that resembles a rotation ellipsoid with a maximal volume of

$$V_{ion} = \frac{4}{3}\pi \mathbf{z}_0 \mathbf{r}_0^2 \tag{2.45}$$

where r_0, z_0 stand for the radial and axial extension of the ensemble [Dehmelt, 1967]. In thermal equilibrium [Dubin and O'Neil, 1999] the ion density distribution at a temperature T is expected to be

$$\rho(r) = \rho_0 \exp\left[-\frac{q}{k_B T}\left(\Phi_{eff}(r) + \Phi_{sc}(r)\right)\right], \tag{2.46}$$

where $\rho(r)$ is the charge density as a function of r, ρ_0 is the charge density for r = 0 and Φ_{sc} is the electrostatic potential due to the ions (*space charge*). Therefore, the proportion of the effective potential in relation to the space charge can be seen if Eq. (2.46) is reformulated to

$$\Phi_{sc}(r) = -\frac{k_B T}{q} \ln\left[\frac{\rho(r)}{\rho_0}\right] - \Phi_{eff}(r) \tag{2.47}$$

At zero temperature the effective potential would exactly counterbalance the space charges

$$\Phi_{eff}(r) + \Phi_{sc}(r) = 0 \tag{2.48}$$

where the radial profile of the ion density can be derived from Poisson's equation

$$\rho(r) = \frac{\epsilon_0}{q} \nabla^2 \Phi_{eff}(r) \tag{2.49}$$

Calculating Eq. (2.49) with the potential in Eq. (2.24) leads to the low-temperature approximation of the ion density [Champenois, 2009, Majima et al., 2012]

$$\rho(r) = n^2 (n-1)^2 \frac{\epsilon_0 V_{RF}^2}{m\omega^2 r_0^4} \left(\frac{r}{r_0}\right)^{2n-4}. \tag{2.50}$$

Another useful relation resulting is the charge per unit length l of a multipole

$$q_l(r) = \pi\epsilon_0 (n-1) \frac{q}{m} \left(\frac{n V_{RF}}{\omega r_0}\right)^2 \left(\frac{r}{r_0}\right)^{2n-2} \tag{2.51}$$

that can be extended to an upper boundary for stored charges, presupposing stable trapping conditions $\eta(r_q) < 1$ for the ion cloud radius r_q

$$Q_l(r_q) = \frac{1}{2}\pi\epsilon_0 n\, \eta(r_q)\, V_{rf} \left(\frac{r_q}{r_0}\right)^n < q_{max} \tag{2.52}$$

with $Q_{max} = \frac{1}{2}\pi\epsilon_0 n V_{rf}$ the maximal charge in the trap [Tolmachev et al., 2000].

2.5 Cooling techniques

Long storage times in ion traps require stability and resistance of the trapped particles to RF excitation, which can be attained by cooling the ions to the low field regions. Several

methods have been developed to achieve this feature. We distinguish between slowing, which affects only the translational modes, and cooling processes, damping the external and the internal states of the ions. Various cooling methods have been developed [Itano et al., 1995], for example laser cooling [Diedrich and Bergquist, 1989], resistive cooling [Church and Dehmelt, 1969], active-feedback cooling [White and Malmberg, 1982], and collisional cooling [Major and Dehmelt, 1968].

2.5.1 Optical cooling

Laser cooling has been leading the way, but the particles must provide a clearly resolvable electronic level structure, featuring a distinctive transition that can be addressed by resonant radiation [Stenholm, 1986, Wineland et al., 1987]. With the *Doppler-cooling* scheme the atom absorbs the energy $\hbar\omega$ which induces a transition to an excited state. The laser will be off-resonant detuned to compensate for a Doppler-shift in the spectrum of the moving atom. The atom gets a momentum $\hbar\mathbf{k}$ along the direction of the light propagation and experiences another one due to the isotropic emission of a spontaneously emitted photon. Successive absorption processes, followed by momentum recoil in random directions, leads to the dissipation of momentum in the direction of the incident light beam.[3]

The momentum exchange is velocity dependent, where the achievable temperature T is limited by photon diffusion. The *Doppler-limit* is given by $k_B T = \hbar\gamma/2$, with γ being the inverse of the excited state life time, the natural line width of the transition. The Doppler temperature limit can be overcome by *polarisation gradient cooling* [Dalibard and Cohen-Tannoudji, 1989, Kuppens et al., 1998], while *Raman cooling* [Kasevich and Chu, 1992, Lee et al., 1996] allows for laser cooling below the recoil limit. These cooling schemes protect the atom from the momentum diffusion due to spontaneous emission (recoil heating).

Whereas this method has been successfully realised for several atoms [Diedrich and Bergquist, 1989], it could only be extended to some diatomic molecules [Bahns et al., 1996, Rosa, 2004, Shuman et al., 2010]. Complex molecules exhibit numerous degrees of freedom, not only electronic, but also rotational and vibrational states. With increasing complexity of the molecular composition it is practically not possible to excite cyclic

[3] A comprehensive treatment can be found in [Arimondo et al., 1993].

transitions. Furthermore, rotational and vibrational levels in the electronic ground state have long lifetimes, and the molecule cannot fully release its absorbed energy. Therefore irradiating a molecule with a laser beam primarily leads to an increase of internal energy and most likely to thermal decomposition.

Ensuing from works by the group of H. Ritsch [Horak et al., 1997] cavity assisted laser cooling (*cavity cooling*) is a further scheme which utilises a cavity field to cool translational modes of a polarisable particle. By now, the method has been demonstrated for high-mass nanoparticles of the size of 10^{10} amu [Kiesel et al., 2013, Asenbaum et al., 2013]. The use of an external cavity compensates for the non-existent cycling transitions in the particles, where the momentum exchange takes place between light and matter. This technique works well in slowing mesoscopic objects in their transverse as well as longitudinal velocity. However, particles have to be polarisable and their internal states may even be heated up [Barker and Shneider, 2010].

2.5.2 Sympathetic cooling

At low temperatures and high density a regular array of ions A can form a *Coulomb crystal* [Wuerker et al., 1959, Drewsen et al., 2003]. If a second ion species B can simultaneously be trapped with the crystal, the ions A + B couple via their Coulomb repulsion. In practice, the ions of A are laser-cooled atoms and the substituent B molecular ions, which interact with the cooling laser indirectly. Thus, the translation of the particles of interest can be dampened by embedding them into the crystal [Bowe et al., 1999]. Here, even complex molecules can be involved [Ryjkov et al., 2006, Ostendorf et al., 2006].

Sympathetic cooling can prepare translationally cold particles in the range of mK – μK. Since the long-range Coulomb interaction does not provide internal state relaxation, particles in a Coulomb crystal can be internally hot [Bertelsen et al., 2006]. Furthermore, trapping of two different ion types is practically limited to a range of mass-to-charge ratios. Despite those challenges, some works have shown molecules already in the mass range of $10^2 - 10^3$ amu like organic compounds [Ryjkov et al., 2006] or fullerenes C_{60} [Ostendorf et al., 2006] to be sympathetically cooled by Mg^+, or Ba^+, down below 1 K.

Collisions of molecular ions with laser-cooled atoms lead to the advancement of

sympathetic cooling which combines the merits of both laser and collisional cooling. Thereby even complex particles could reach ultracold temperatures where internal as well as external degrees of freedom will be cooled down [Hudson, 2009].

2.5.3 Collisional cooling

Collision-induced relaxation with a bath gas of electrically neutral particles is a more general method being applicable to a broad range of even complex samples which is independent on the exact energy level pattern of the to-be-cooled species, also been referred to *buffer-gas cooling* [Major and Dehmelt, 1968, Sulkes et al., 1980]. Here, thermalisation takes effect on all degrees of freedom via elastic and inelastic collisions with cold particles being lighter in mass than the target. The sole prerequisite is that the sample is capable of experiencing numerous collisions in the course of reaching a thermal ensemble with the gas molecules where it does not dissociate.

When estimating the number of collisions N that are needed to cool the ions by the buffer gas particles, we can assume the conservation of momentum and energy and a hard-sphere model:

$$N = -\mu \cdot \ln\left(\frac{T_N - T}{T_0 - T}\right) \tag{2.53}$$

where

$$\mu = \frac{\left(m + m_{\mathrm{bg}}\right)^2}{2m \cdot m_{\mathrm{bg}}}, \tag{2.54}$$

m_{bg} stands for the mass of the buffer-gas and m for the mass of the trapped ion [DeCarvalho et al., 1999, Egorov et al., 2002].

For nanoparticles, in the range of $10^4 - 10^8$ amu, excited to 1 eV, thermalisation with a helium He buffer-gas at 4 K would need several thousands of collisions (see therefore Fig. (2.8)). At gas densities of 10^7 to $10^{16}\,\mathrm{cm}^{-3}$, which correspond to pressures of 10^{-11} to 10^{-2} mbar for an ideal gas at 4 K, cooling can occur between minutes to a few milliseconds [Gerlich, 2008a, Gerlich, 2008b].

Since we are interested in the time it takes for massive particles to cool down in a light-weight bath gas at cryogenic temperature we consider the *mean free path* ℓ of a

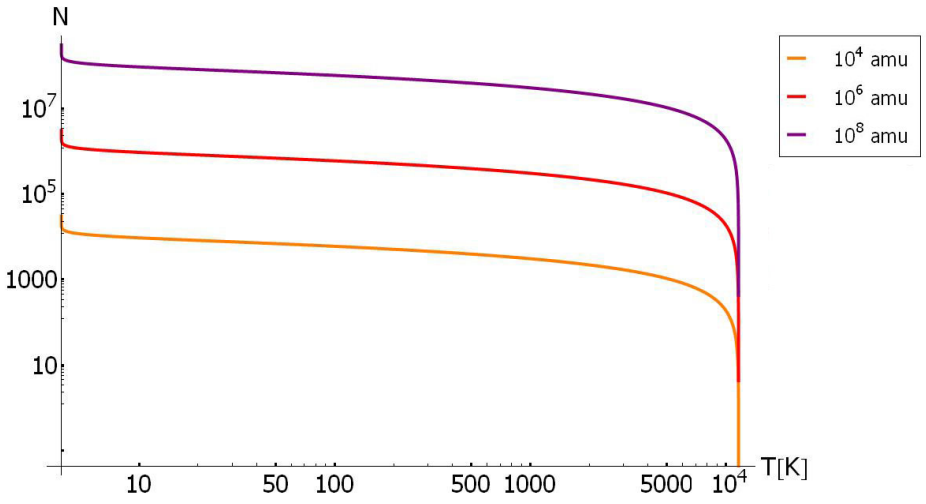

Figure 2.8: The number of necessary collisions N to cool an ion of 10^4, 10^6 *and* 10^8 *amu mass (indicated by the colors orange, red or purple respectively) with* 1 eV *kinetic energy down to a specific temperature with a helium buffer-gas at 4 K. The abscissa shows the temperature* T_N *the regarded sample possesses.*

particle in the gas of density n

$$\ell = \frac{1}{\sigma \cdot n} \tag{2.55}$$

with the collision cross-section σ. It suffices to regard the geometrical cross-section $\sigma_{geo} = \pi \left(r + r_{bg}\right)^2$ that can be computed from the radii of the massive particles and the buffer-gas, respectively. The ideal gas law relates $n = \frac{p}{k_B \cdot T_{bg}}$ with the pressure p and temperature T_{bg} of the gas. For spherical clusters, the particle radius $r = \sqrt[3]{\frac{3m}{4\pi\rho}}$ is defined by the material density ρ.

The period for a particle to move freely in the buffer-gas (*mean free time*), the mean relative velocity of the gas molecules and ions has to be included [Demtröder, 2008]

$$\tau = \frac{\ell}{\langle v \rangle} = \frac{1}{\sigma \cdot n \cdot \overline{\Delta v}} = \frac{1}{\sigma \cdot n \cdot \sqrt{2\left(v_{bg}^2 + v_{ion}^2\right)}} \tag{2.56}$$

where we consider ions of $m > 10^4$ amu with an initial kinetic energy on the order of 1 eV. Then, the velocity of the buffer-gas is smaller than the velocity of the ions, $v_{bg} > v_{ion}$.

Since the buffer gas particles are presumably in a thermal equilibrium, their velocity can be calculated from the most probable velocity of a Maxwell-Boltzmann distribution

$$v_{\mathrm{bg}} = \sqrt{\frac{2k_{\mathrm{B}}T_{\mathrm{bg}}}{m_{\mathrm{bg}}}} \tag{2.57}$$

which would be 130 m/s for helium at 4 K temperature. The thermalisation time then reads

$$t_{\mathrm{cool}} = N \cdot t_{\ell} \tag{2.58}$$

which becomes Eq. (2.59) after inserting the relations from above

$$t_{\mathrm{cool}} = N \cdot \sqrt{\frac{m_{\mathrm{bg}}k_{\mathrm{B}}T_{\mathrm{bg}}}{2}} \cdot \frac{1}{\pi p \left(r_{\mathrm{bg}} + \sqrt[3]{\frac{3m}{4\pi\rho}}\right)^2}. \tag{2.59}$$

In Fig. (2.9) densities of silica SiO_2 ($\rho_{SiO_2} = 2.65$ g/cm^3) and gold ($\rho_{\mathrm{Au}} = 19.32$ g/cm^3) were chosen to show to which extent the compactness of the particle contributes to the cooling performance. The buffer-gas pressure was supposed to be 10^{-3} or 10^{-5} mbar . While the density of the particle composition has a minor effect on the thermalisation time, the buffer gas pressure predominantly determines the cooling period.

Buffer-gas cooling serves well for trapped ions and is quite universal as it is compatible with many different molecular species. However, the thermalisation is limited to the condensation temperature of the bath gas that is used. Nevertheless, Gerlich et al. [Gerlich, 2008a, Gerlich and Borodi, 2009] using the directed pulse of a cold neutral gas crossing the trapped ion cloud. The effusive beam of previously cooled helium was velocity selected and only the slowest tail of the Maxwell-Boltzmann distribution was allowed to pass. Cutting off nearly 90 % of the thermal distribution still enables enough collisions while in combination with cryopumping, a very low gas consumption with a small overall gas load for the setup as a whole is possible to achieve. Here, the slow beam of buffer-gas at temperatures below 1 K successfully cooled atomic ions in a 22-pole trap. A further discussion of the feasibility of the buffer-gas cooling technique in connection with the requirement of a decoherence-free environment will follow in Sec. (3.3).

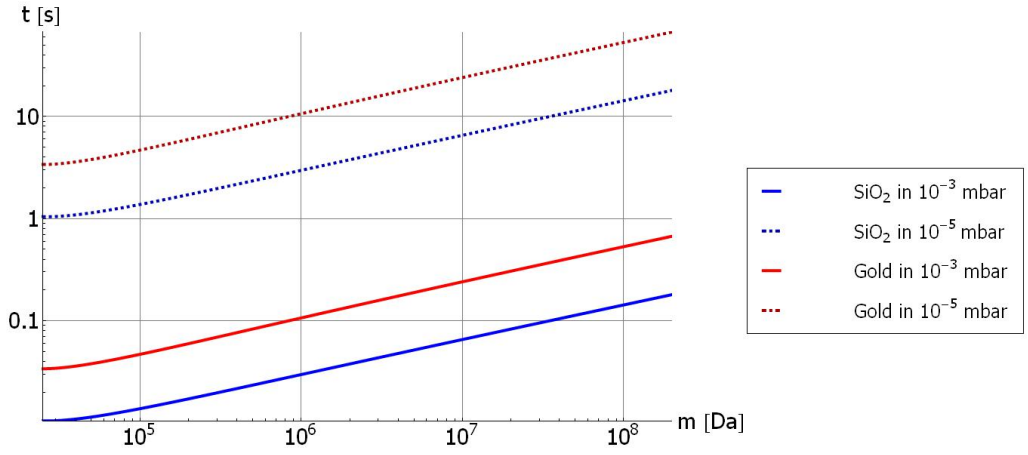

Figure 2.9: The time it takes a particle to thermalise in a 4K He buffer-gas. Two types of particles in terms of density $\left[\mathrm{m/cm^3}\right]$ *were regarded. As an example for a low density particle* SiO_2 *was chosen while gold represents a nanoparticle of high density. Furthermore two cases of buffer gas pressure were exemplary treated,* 10^{-3} *mbar (solid line) and* 10^{-5} *mbar (dashed line).*

Chapter 3

Trap Design

3.1 Experimental scheme

Aiming at future matter-wave experiments, a compact design of combined ion optical devices has been conceived and simulated. The setup (see Fig. (3.1)) consists of four main parts, linked by electrostatic lenses (here triples of ring-electrodes, namely *Einzellenses* will be used), starting with a quadrupole ion trap (i) for mass-selection and accumulation of the incoming particles. Here, ions will already be de-excited by collisional cooling with gas of ambient temperature. Leaving the quadrupole, the ion cloud travels into a cold hexapole trap (ii) to be further cooled by a pulse of cryogenic buffer-gas at $T = 65$ K. In the next step, the pre-cooled ion beam will be guided by several electrodes, focussed and bent by a quadrupole deflector (iii) permitting a way of minimising overall gas ballast and providing optical access. After passing the third Einzellens, the ions find themselves in the dodecapole ion trap (iv) which will be employed for the preparation of a dense particle cloud and the final cryogenic buffer-gas cooling at $T = 4$ K.

The proposed setup should be capable of preparing cold massive molecular beams and it holds the potential to enclose a matter-wave interferometer within the cooling trap (see also Ch. 5.3).

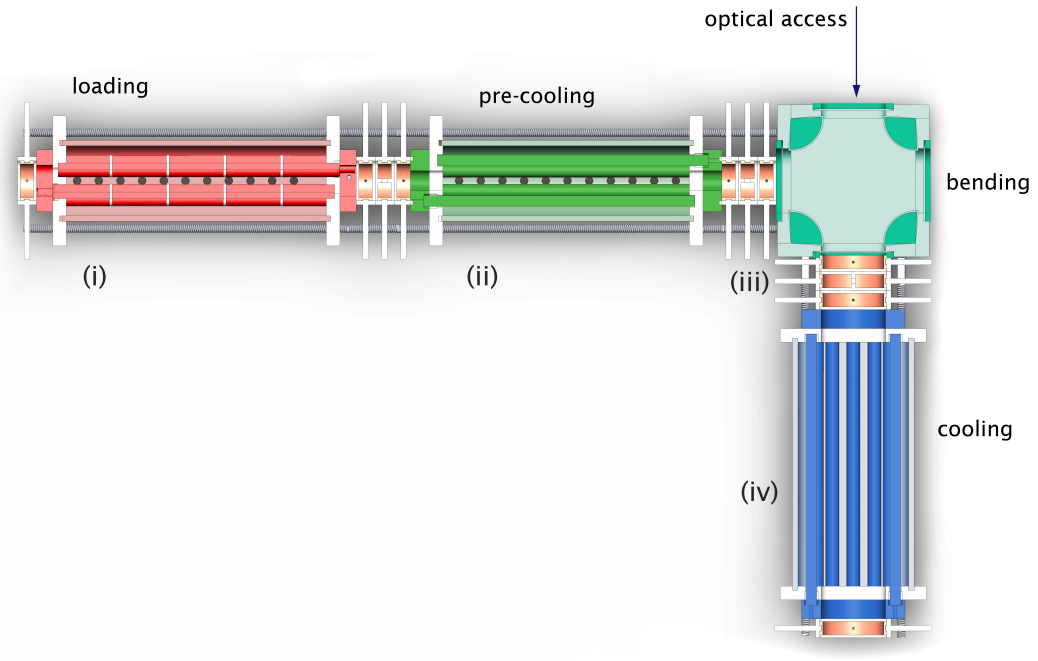

Figure 3.1: Schematic view of the Cold Ion Trap System. The red area indicates the quadrupole ion trap (i) with its buffer-gas cell and segmented electrodes. The hexapole ion trap (ii) follows in green. Then the turquoise field illustrates the quadrupole bender (iii), while the blue section stands for the dodecapole trap (iv) also surrounded by a buffer-gas cell. All light-brown fields depict ring electrodes that are, on the one hand, endcap electrodes and, on the other hand, parts of an Einzellens.

3.2 Load particles

The suitable approach of loading particles into the experiment primarily depends on the choice of particles. Here, the generation of dense ensembles with a narrow and well-selected mass distribution is to achieve.

Pure metal or semiconductor clusters can be produced by *cluster aggregation sources* (CAS) [Haberland et al., 1991, Pratontep et al., 2005] where generous amounts of atomic samples are sputtered and stochastically bonded into larger compounds. The particles ($M_n = 1 \ldots 10^5, n \in \mathbb{N}$ the number of metal atoms) can be ionised by single photons with energies of 4-7 eV for pure semi-conducters and 10-12 eV for oxides. When employing soft ionisation of those clusters typically less energy than for photofragmentation is required.

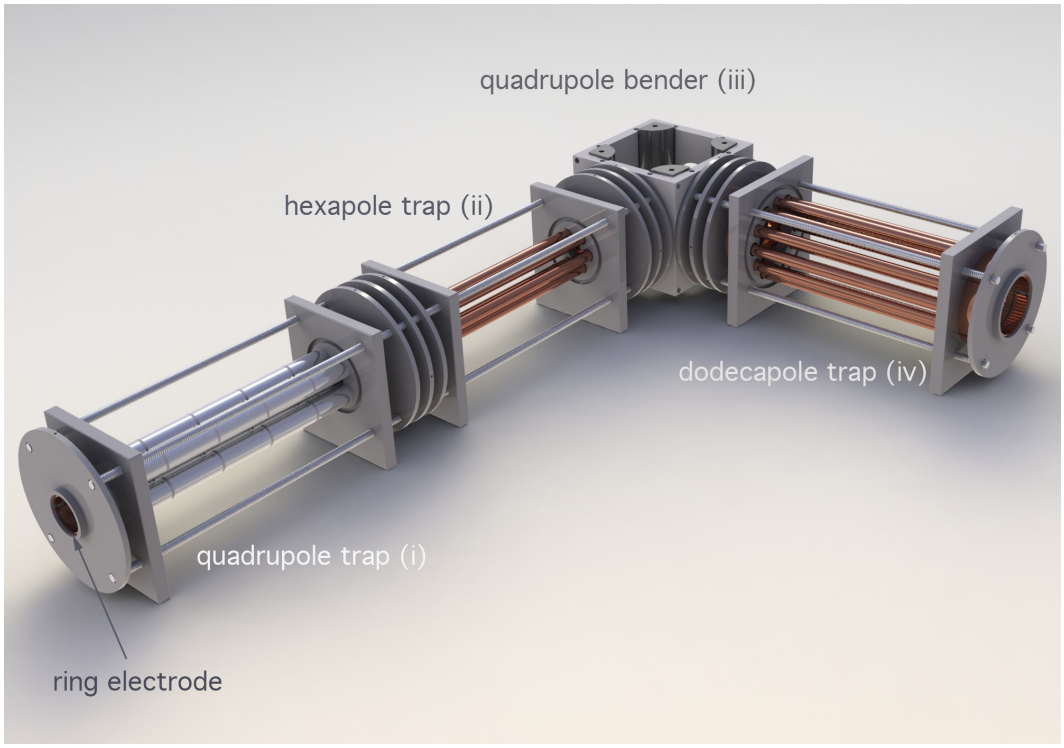

Figure 3.2: The open structure of the Cold Ion Trap System without the buffergas shells and top cover of the quadrupole bender. Ring electrodes used both as endcaps and Einzellenses are embedded into large insulator disks.

Many particles may be launched using *laser-induced acoustic desorption* (LIAD) providing low charge or even neutral states of the massive entities in the gas-phase with an efficient energy transfer to break the bonds between adsorbate and surface [Golovlev et al., 1997]. It is assumed that through mechanical forces and strong local acceleration the analyte particles will be detached from a surface-bound state. This method has already been successfully shown for viruses and cells, i.e. up to a mass range of 10^9 amu in works of Peng et al. [Peng et al., 2004a, Peng et al., 2006]

While *biomolecular particles* are advantageous in being pre-selected in mass and functionality by nature, proteins, viruses or cells may undergo various structural and electronic modifications when absorbing an ultraviolet (UV) or vacuum ultraviolet (VUV) photon. Fragmentation is a common obstacle in the volatilisation of biomolecular samples. This is aggravated by the rather high ionisation energies needed to obtain charged biomolecules (8-15 eV). Yet, there are soft ionisation techniques which are efficient in

launching biomolecules into the gas-phase.

Here, *electrospray ionisation* (ESI) provides particle fluxes of large compounds ranging from proteins over oligonucleotides [Fenn et al., 1989] to whole viruses and bacteria [Bothner and Siuzdak, 2004, Meetani and Shin, 2007]. The formation process at atmospheric pressure gives negatively and positively charged entities albeit the resulting mass-to-charge distribution is rather broad. Furthermore, ESI is known to produce very high charge states for single particles (e.g. over 100 e), wherefore different ways of charge reduction have been conceived. While the attachment or removal of electrons tends to destabilise biomolecules, it has been shown that charge reduction by exposure to a gas of bipolar ions can be utilised [Scalf et al., 1999].

However, the need for a collision free space for interferometry at pressures as low as $10^{-10} - 10^{-12}$ mbar is in contrast to volatilisation at atmospheric pressure. ESI bears promises as a continuous source for a matter-wave experiment and some technological challenge with regard to the vacuum constraints. Differential pumping can solve this problem.

Aside from that, loading of organic material with *matrix-assisted laser desorption ionisation* (MALDI) [Karas and Hillenkamp, 1988, Tanaka et al., 1988] is a standard technique in molecular biology and exhibits a mass range of far beyond 10^6 amu [Cai et al., 2002]. Particles are desorbed from a surface prepared sample by shining a pulsed laser onto it. The use of a matrix-analyte mixture permits a controllable transfer of energy whereby the analyte should be isolated in the matrix. In the process of desorption chemical reactions promote the ionisation of the analyte molecules [Karas and Krüger, 2003]. Since MALDI mostly delivers lowly charged particles, it is a convenient method of creating samples for the trap system.

3.3 Buffer-gas cells

As described in see [Doyle et al., 1995, p. R2515], buffer-gas cooling needs rather high gas densities, typically pressures of $10^{-2} - 10^{-4}$ mbar [Douglas and French, 1992]. Since ultra-high vacuum conditions are required for the operation of the ensuing interference experiments, ways have to be found to keep the overall gas load arising from the buffer-gas cooling as small and concentrated as possible.

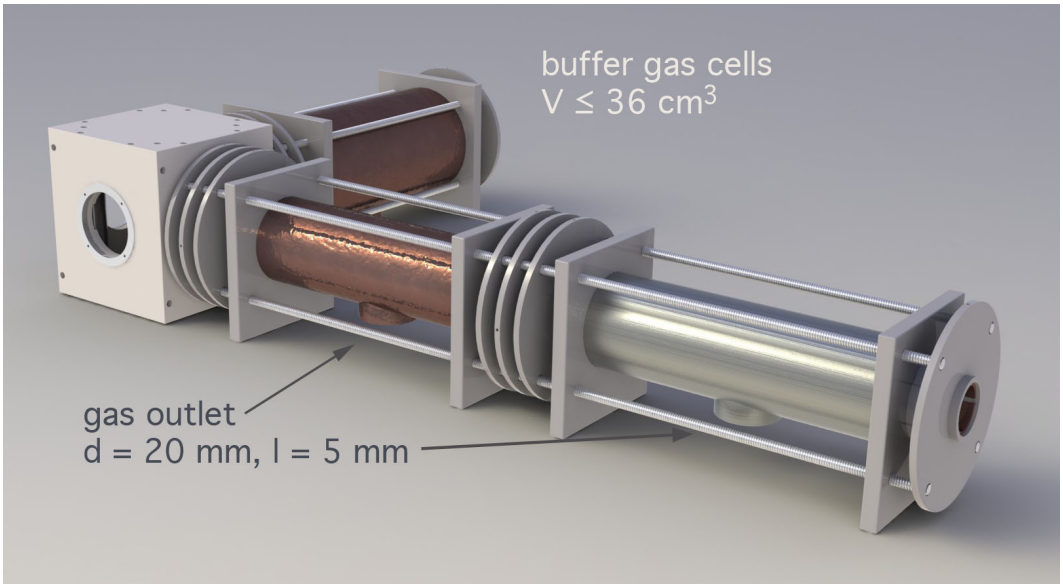

Figure 3.3: The cold ion trap setup with buffer-gas cells reducing the active gas volume for enhancing cooling performance and overall pressure improvement.

For the application of dense buffer-gas ensembles the active gas volume will be reduced by the insertion of a container[1] around the ion trap. Then, with the employment of an additional turbomolecular pump that promotes enhanced pumping of the enclosed space, the difficulties could be surmounted in admittedly finite time.

Vacuum pumps exhibit constant volume flow rates, described by their *pumping speed* S [Jousten, 2006, O'Hanlon, 2003]. The pumping time for reaching a final pressure p_f from the initial p_i is given by

$$t_{\text{pump}} = \frac{V}{S_{\text{eff}}} \ln\left(\frac{p_i}{p_f}\right) \tag{3.1}$$

where the effective pumping speed S_{eff} includes the molecular conductance C which accounts for the reduced efficiency of the vacuum pump with

$$S_{\text{eff}} = \frac{S}{1 + S/C} \,. \tag{3.2}$$

For the calculation of the molecular conductance C, the several kinds of flow concerned in the particular setup and how the vacuum pump is connected to a container have to

[1] In the following will be referred to "buffer-gas cell".

be regarded. The molecular flow through a circular aperture C_B can then be estimated over

$$C_B = \frac{\bar{c}}{4} \cdot A \tag{3.3}$$

where $\bar{c}$ denotes the average velocity of the gas particles at a given temperature and A is the area of the opening. We consider the simple case of the vacuum pump to be directly connected to the gas outlet which is a short pipe of circular cross-section. Therefore, the conductance C is

$$C = C_B \cdot P \tag{3.4}$$

with the transmission probability inside the outlet tube $P = 1 - \frac{l}{d}$ set up by the ratio of the length l and the diameter d of it.

For the designed configuration in Fig. 3.3, the dodecapole could be covered by a copper tube of ø 40 mm and of 90 mm length that has a circular gas outlet of ø 20 mm and 5 mm length. In Fig. 3.4 the time it would take to evacuate the buffer gas cell starting from two different background pressures is illustrated. The graph assumes a pumping speed of 58 l/s, which corresponds to a small turbomolecular pump at helium gas load [Pfeiffer Vacuum, 2015].

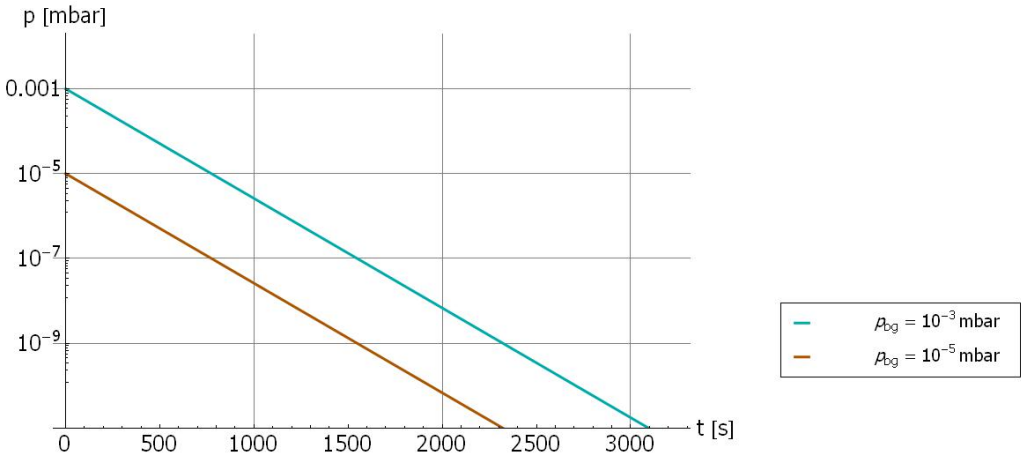

Figure 3.4: Pumping the volume of the buffer-gas cell with a 70 l/s turbo pump starting from a gas pressure of 10^{-3}, 10^{-5} *mbar. A difference of two order of magnitudes in the initial pressure leads only to a small variation in the pumping time reaching values relevant for the interferometer.*

3.4 Mass selection and accumulation

Starting from a continuous influx of particles, beam cleaning will be implemented by a quadrupole mass filter. As described in Sec. 2.2.1, the instrument filters out ions having unstable trajectories regarding their mass-to-charge ratio (m/q) in relation to the operating Mathieu parameters a_M, q_M. In the usual configuration, the quadrupole filter uses a combination of a time-independent (DC) and time-dependent (AC) electrical field, making the use of mutual stability conditions on the particles. Hence, it performs like a bandpass filter [Miller and Denton, 1986]. If the device is used in the RF-only mode, meaning $a_M = 0$, the quadrupole filter acts as a high pass mass filter. In this case a broad range of (m/q) is accepted.

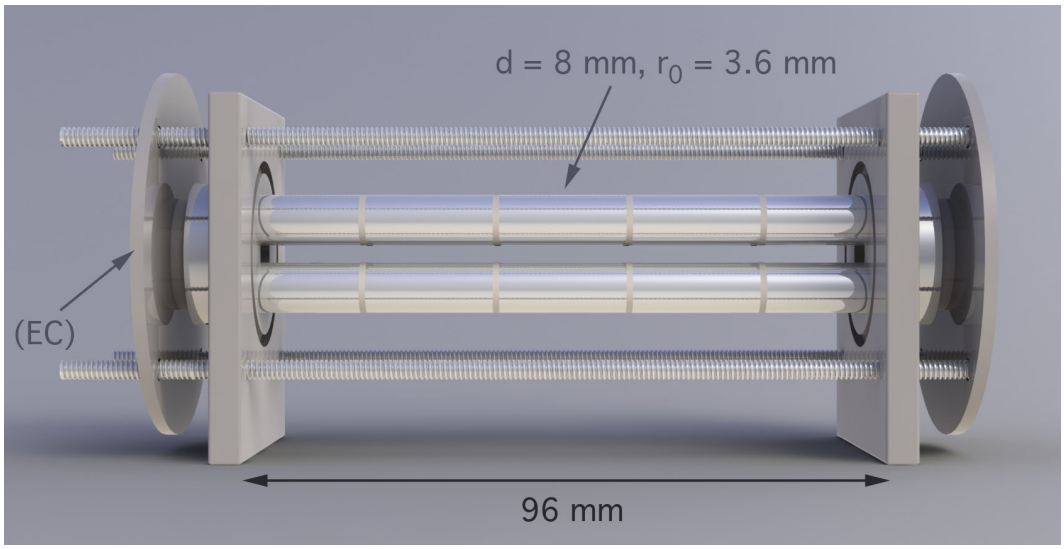

Figure 3.5: The quadrupole ion trap consists of segmented circular rods which will be connected at the ring-like tailpieces; each associated with one of the two phases of the RF field. The rod segments are individually contacted with the power supply. Inside the large insulator disks, both at the front and at the end of the trap, the endcap electrodes (EC) are situated.

This preparatory ion trap (see Fig. (3.5)) is designed of segmented circular rods that consist of metallic hollow cylinder parts being slipped on smaller ceramic poles. The electrode segments possess individual voltage connectors and are electrically separated by ceramic disks. The DC end-electrodes and the einzellenses consist of metallic rings that are embedded in insulator disks. A buffer-gas pulse at room temperature serves to enhance stability of the ion's motion. However, as ion-optical simulation showed

(see Ch. 4.5), the thermalised particles are not likely to propagate out of the trap when the axial confinement is switched off. Thus, if the ions have to be ejected from the quadrupole trap. The use of an additional DC field is needed to guide them in the preferred direction. With this, particles will be again accelerated what counteracts to some extent the previous cooling process.

A possible solution is the gradual shrinking and shifting of the ion cloud. This can be achieved by increasing the static voltages to parts of the ion trap rods in several steps. With the use of segmented electrodes the described manipulation of the ion cloud can be realised, similar to [Herfurth et al., 2001]. Since the phase-space volume of the trapped ions always stays constant, the abrupt raise of the potential would lead to instabilities in their motion unless the added kinetic energy could be diffused. Hence, the compression of the ion cloud has to be conducted during the buffer-gas cooling process.

3.5 Pre-cooling and guiding

In the presence of buffer-gas cooling it is convenient to have the particles in a region of nearly conservative forces. For that reason multipoles of higher order $n > 2$ are favorable, since they provide a wider field-free core (see Sec. 2.1.2). A compromise between a large volume for cooling collisions and the confinement of the ions close to the trap axis for further transport is the hexapole field (Sec. 2.2.2).

The hexapole design is shown in Fig. (3.6). Its elements are chosen to be made from copper meeting the requirements of low-temperature applications (see Ch. 4.5). The purpose of this device is to cool the ions by transferring them in a surrounding of cryogenic helium gas at 4 K to achieve small particle velocities. Shuffeling the ions between the stages leads to a gain in kinetic energy which can be reduced after the transfer.

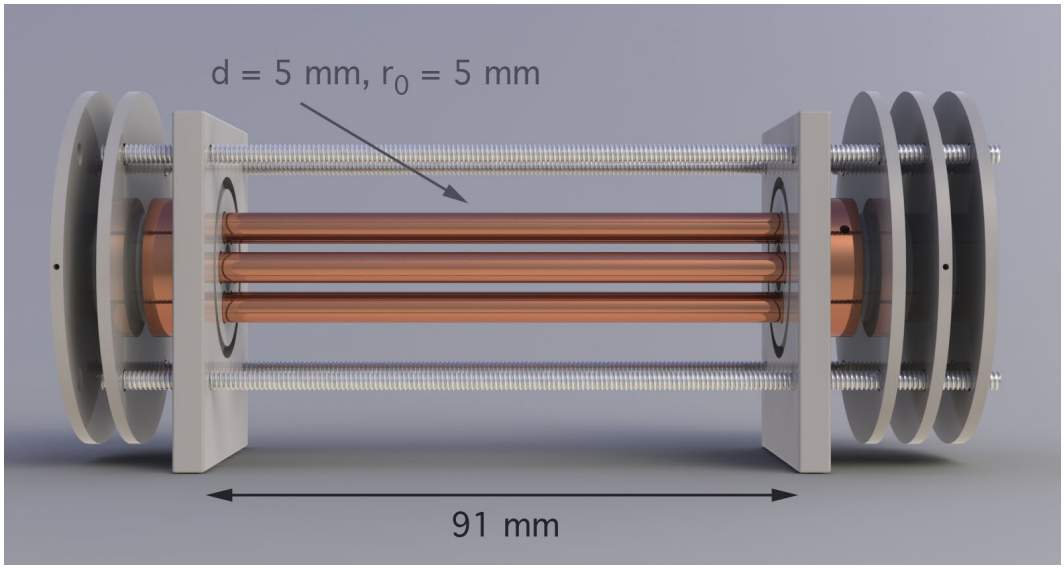

Figure 3.6: The designed hexapole ion trap encompassed with several ring-electrodes, some being part of the einzellenses.

3.6 Bending the ions

The devised matter-wave experiment requires optical access to the cooled ion cloud. This cannot be achieved in the hexapole trap. Performing the experiment in another ion trap connected linearly to the previous ones is not an option: The laser pulses of the experiment have to be directed along the axes of the ion trap. Hence, the ions in the quadrupole and hexapole would also be illuminated. This would lead to severe heating of the molecules, photofragmentation and electron detachment. An alternative is to bend particle beam around the corner of a *quadrupole ion deflector* [Farley, 1985] into another ion trap. In doing so, it can be garanteed that only the ions in the last ion trap are affected by the intense laser light. However, the ideal quadrupole geometry does not allow for sufficient space for a broad laser beam. Hence, our deflector (illustrated in Fig. (3.7)) features electrodes whose diameter is smaller then the inscribed radius. In addition, ring-electrodes on either side of the deflector allow to apply a DC potential.

The sketch in Fig. (3.8) shows to what extent the electrodes (radius r) of the conceived deflector deviate from the quadrupole geometry. Since the actual electrode radius r_s is smaller than r, the charged particles will not simply follow the ideal field pattern. During a 90 degree turn the particles will come nearer to the surface of one the

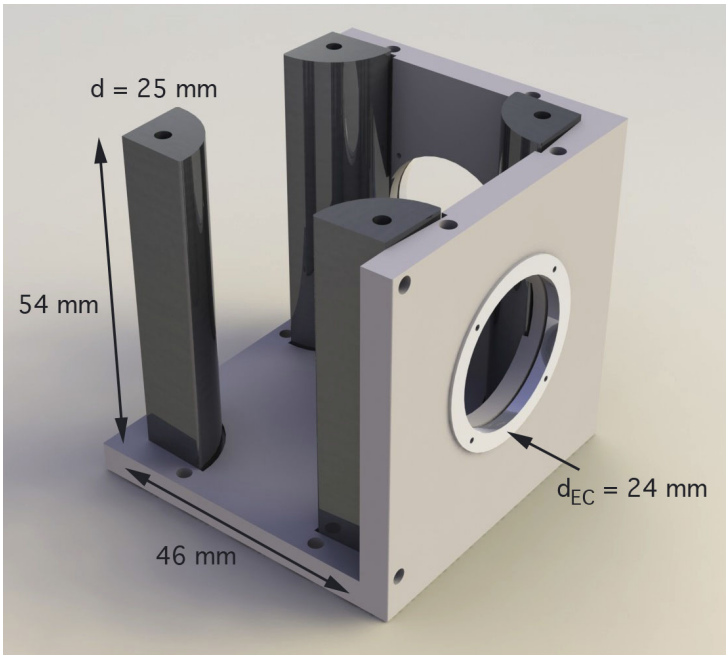

Figure 3.7: The designed quadrupole ion bender, partly open.

bending electrodes. Experiencing a stronger field at the attractive rod, the ion crosses an effectively asymmetric field pattern, leading to translational heating.

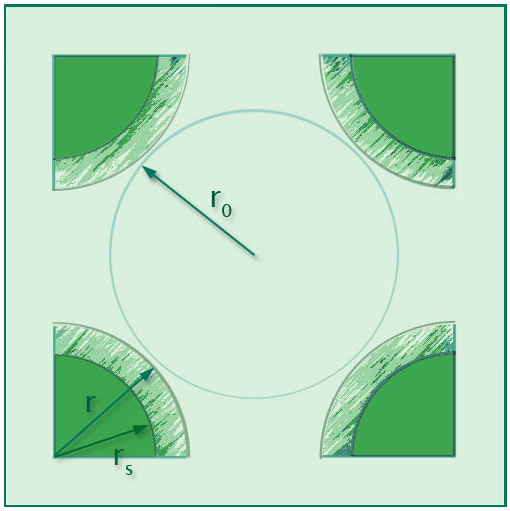

Figure 3.8: The rod diameter comparison - ideal quadrupole field

3.7 Cooling stage

The ion trap for the last cooling step of the experiment has to provide an even larger field free region in view of an efficient collisional cooling while the effective potential (see Fig. (2.2)) should not push the ions to the vicinity of the trap electrodes. In the current design a multipole of the order $n = 6$ has been discussed where the corresponding dodecapole potential was already shown in Sec. 2.2.3.

Buffer-gas cooling could be pursued in two ways: One may use a buffer-gas pulse of lower pressure whereby the thermalisation time (in Eq. (2.58)) increases. For instance, a gas pulse producing a pressure of 10^{-5} mbar inside the buffer-gas cell of the dodecapole would lead to a cooling time of at least 18.2s (see Sec. 2.5.3). This would extend the duty cycle for gas influx and subsequent pumping unreasonably. The reduction in pressure is not a favourable strategy for realising buffer-gas cooling in this arrangement.

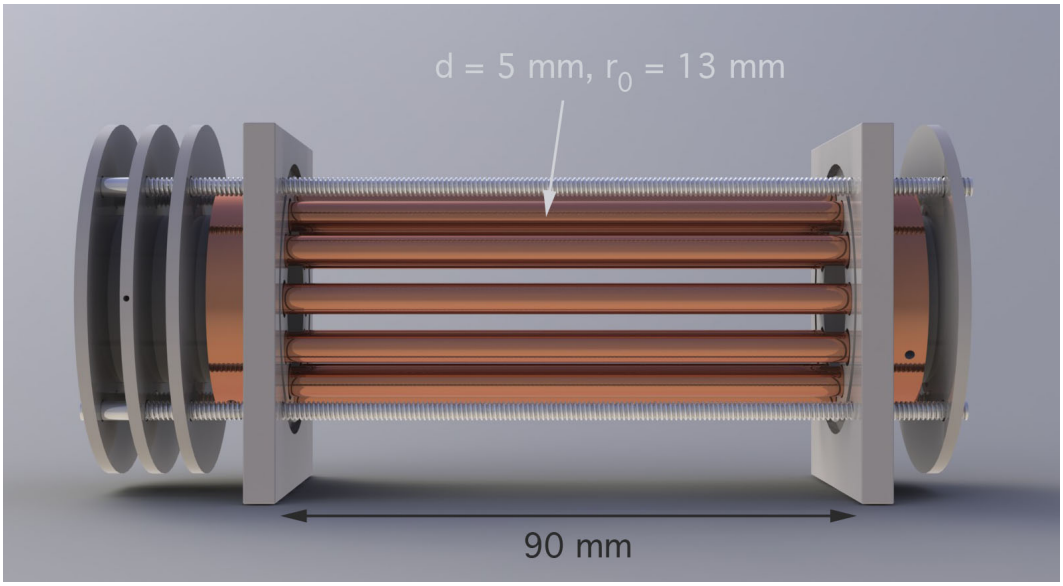

Figure 3.9: The designed dodecapole (12pole) ion trap.

The cold effusive beam method (cf. Sec. 2.5.3) can be applied by injecting a velocity-selected pulse of very slow helium gas transversely into the cryogenic multipole (as in [Gerlich and Borodi, 2009]). Keeping the gas load small in order to readily attain sufficiently low background pressures is possible with the implementation of the precise buffer-gas cooling technique, in addition to the previously described solutions.

3.8 Interference experiment

The purpose and the design of the Cold Ion Trap System was chosen to serve as a source for a subsequent matter-wave experiment of the high mass nanoparticles. Apart from the option to extract the well-prepared and cooled ion cloud from the cold multipole, to be neutralised and forwarded into an existing interferometer, we considered the possibility to perform interferometry inside the multipole trap after the cooling process. Based on OTIMA [Haslinger, 2013], three successive laser pulses would be applied to the molecular cloud for the diffraction procedure. Therefore, the optical access at the side of the quadrupole bender could be used to shoot the interference laser along the last multipole trap onto a mirror that is mounted behind it. Further discussion on the interferometric scheme and its potential will be given in Ch. 5.3.

3.9 Detection

The detection scheme strongly depends on the choice of the used particles. Several methods are available for detecting nanoparticles in a mass range of up to 10^7 amu with acceptable efficiency. For ions charge-sensitive detection is straightforward when they are accelerated towards a channeltron ion counter [Fricke et al., 1980]. When already employing secondary electron generation, time-of-flight measurements can also be accomplished [Campbell et al., 1998]. Neutral particle can be post-ionised prior to a charge detection via subjection to a plasma [Ishitani et al., 1978], an electron impact source [Matt et al., 1997], or utilising photoionisation by shining on a laser of short wavelength as in [Hontañón and Kruis, 2008]. However, all methods mentioned have in common that the detection efficiency decreases with increasing mass [Liu et al., 2014].

Many ion experiments with biomolecules use the *laser-induced fluorescence, LIF* [Kinsey, 1977, Peng et al., 2004b] to optically detect them [Peng et al., 2003, Friedrich et al., 2004]. Suitable particles are either fluorescent or tagged with dye fluorophores. Since the applicability of dye-labeling for LIF detection is not restricted to any certain composition or size of the sample, the LIF detection method is essentially not limited in mass range. Therefore this technique is wide-spread in applications working with nano-sized materials and high-mass biomolecules. Moreover, the sensitivity of detecting the fluorescence can be very high depending on the used optical exposure unit, allowing even single-molecule resolution, if the particles are deposited onto a surface.

Chapter 4

Simulation

4.1 Initiation

To explore the feasibility of the system of linear traps and guiding electrodes in terms of particle transfer and thermalisation, ion optics simulations were carried out using the software package SIMION [Dahl, 2000]. The full assembly of conductors is put into the simulation and the voltage, timing and particle parameters are configured by a self-written user program[1].

The amplitude V_{RF} and angular frequency ω of the RF field are set after Eq. (2.24) while taking account of stable operating requirements (see Eq. (2.43)). Considering only singly-charged particles the working parameters of the three ion traps for certain mass values are

ion mass [amu]	10^4	10^6	10^8
$q = 0.3$; frequency of quadrupole [kHz]	196	20	2
$\eta = 0.15$; frequency of hexapole [kHz]	307	31	3
$\eta = 0.15$; frequency of dodecapole [kHz]	491	49	5

Table 4.1: Frequencies for stable operation of the ion traps of introduced geometry at $V_{RF} = 150$ V and different ion masses.

The particle trajectories are composed of points which approximate the solution to Laplace's equation for each time step. They include further information on position,

[1] The details of the chosen set of parameters will be given in the Appendix.

momentum and kinetic energy of each regarded ion at a certain time step.

Buffer-gas cooling can be included by installing the module for calculating the ion-neutral collisions (cf. page 77 in the Appendix). To adjust the thermalisation process the geometrical properties of the gas particles and the effective cross-section of the collision partners have to be set up. Since the simulation program uses a hard-sphere collision model it is convenient to estimate the geometrical cross-sections for nanoparticles that are sphere-like clusters. Thereby collisions of gold particles with He are characterised by the following cross-sections, each corresponding to the mass sizes of prior calculation in Tab.(4.1).

mass of the cluster [amu]	10^4	10^6	10^8
collisional cross section σ $\left[\mathrm{m}^2\right]$	$1.673 \cdot 10^{-18}$	$2.602 \cdot 10^{-17}$	$5.185 \cdot 10^{-16}$

Table 4.2: The calculated collisional cross-sections σ for helium gas with gold nanoparticles. Here, the hard-sphere model uses the geometrical cross-section $\sigma_{\mathrm{geo}} = \pi\left(r_{\mathrm{A}} + r_{\mathrm{B}}\right)^2$ *of two entities A and B with circular extent.*

The designed device is analysed in four different ways. First, we study the outcoupling of the cooled ion beam from the linear quadrupole. Further on, a cold hexapole is tested on how well a single cooling trap works. Then, the simulations focus on the viability of transferring the ions across the Cold Ion Trap System through the quadrupole bender. Finally, the cooling performance of the multipoles is evaluated.

4.2 Outcoupling from the Quadrupole Ion Trap

To test the extraction of buffer-gas cooled ions from a linear ion trap, the quadrupole (cf. Fig. (3.5)) is separately simulated to look at the divergence and velocity distribution of the particle beam. The working parameters for the quadrupole of Tab. (4.1) apply. We start by simulating positively charged particles of 10^6 amu trapped and cooled by a helium gas pulse of 5 ms duration and 10^{-3} mbar pressure at 295 K temperature. An ensemble of 30 ions starts inside the quadrupole with the kinetic energy set to 0.25 ± 0.05 eV, where the energy is Gaussian distributed. Coulomb repulsion has been included.

"Opening" the axial confinement of the quadrupole after 15 ms of trapping by switching off the DC potential at the endcap (electrode 2), should result in the ions leaving the trap. However, the radio-frequency field suffices to capture the thermalised ions for long time. Thus, the particles only drip out of the trap disjointedly. Moreover, the charged particles escape in a solid angles of up to 2π because the ions exhibit varyingly strong radial velocity components due to motion in the RF field.

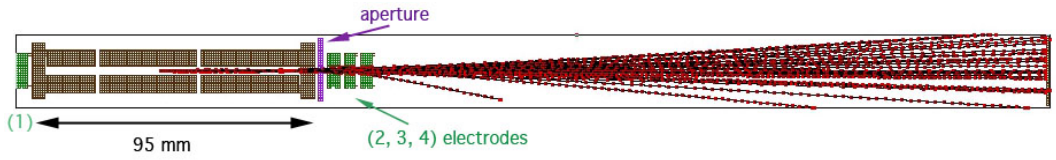

Figure 4.1: Ions freely moving out of the quadrupole ion trap after switching off the endcap electrodes.

Figure (4.1) demonstrates the set of simulated trajectories emerging from the linear trap. They form a conical beam and each ion needs at least 35 ms to reach the detector plate at 200 mm distance. The average particle velocity is.. The data show that the ions proceed with a divergence of $\sigma_\alpha = \pm 47$ mrad approximates the histogram in Fig. (4.2).

One way of extracting the ions on a well-defined track is to use DC electrodes to accelerate them along the trap axis. Including a stack of electrostatic lenses after the aperture and making use of the segmented rods of the quadrupole, the ion cloud can be bunched and guided outside the trap.

Here, the electrodes (2-4) behind the orifice are put on a potential after the period of trapping to build an Einzellens with -50 // 2 // -50 Volts at each ring respectively. For successful out-coupling of the ions, also the aperture is set to $U_{\text{disk}} = -10$V. Additionally, the front endcap (electrode 1) is ramped on a strong repulsive potential to push the ions ($U_{\text{ECpush}} = 100$V).

As can be seen in Fig. (4.3), the stream gets more contracted while the ions are ejected all together within about 8 ms. The bend trajectories at the screen plate indicate that due to the strong amplification some ions get even deflected. Generating once more a histogram and Gaussian distribution curve for the transmitted particles in Fig. (4.4), angles of up to $\sigma_\alpha = \pm 12$ mrad beam divergence occur. Thus, extracting the ions with

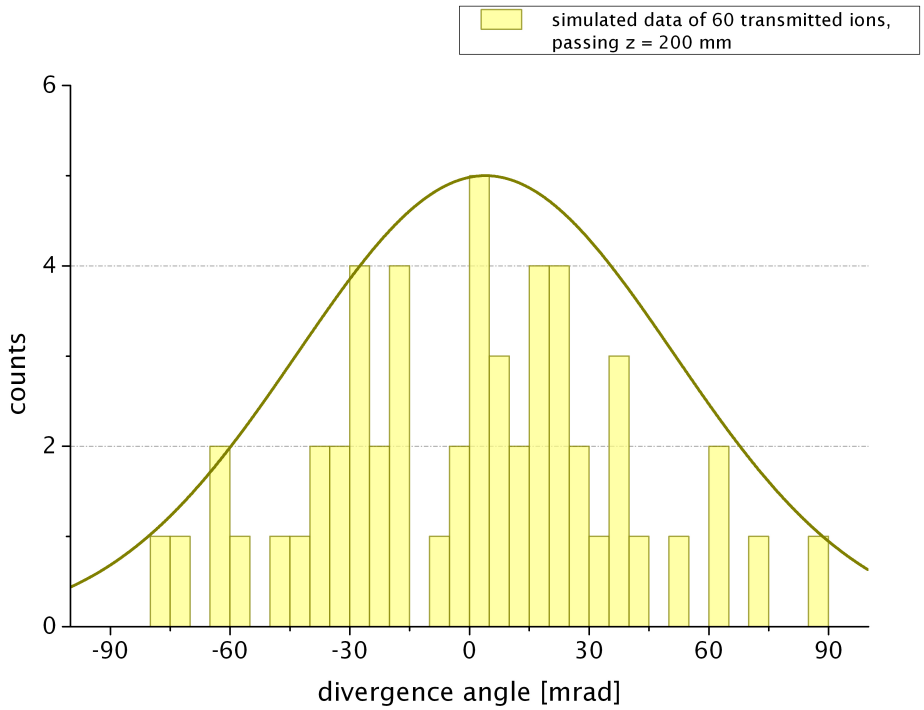

Figure 4.2: Divergence of ions moving out of the quadrupole trap. The standard deviation of the Gaussian distribution curve σ_α is ±47 mrad.

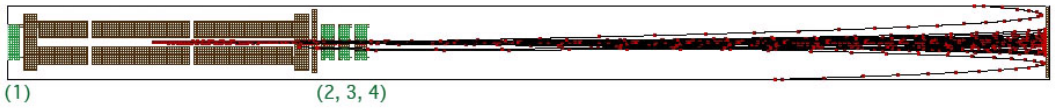

Figure 4.3: Ions extracted due to acceleration with attractive DC voltages out of the quadrupole trap.

electrostatic lenses can visibly reduce the divergence of the outcoming particle stream.

While the average divergence of the beam decreases with increasing DC voltages, the forward velocity is also enhanced. The ion velocities in direction of the trap axis are plotted against the position z (starting inside the quadrupole $z_0 = 60$ mm) in Fig. (4.5). The velocities grow by a factor of 100 (circumscribed part) as compared to the drift velocity in the quadrupole. After diverging from the electrostatic potential (slow decrease until $z = 640$ mm where the detector plate is situated), the ions revert to their starting speed.

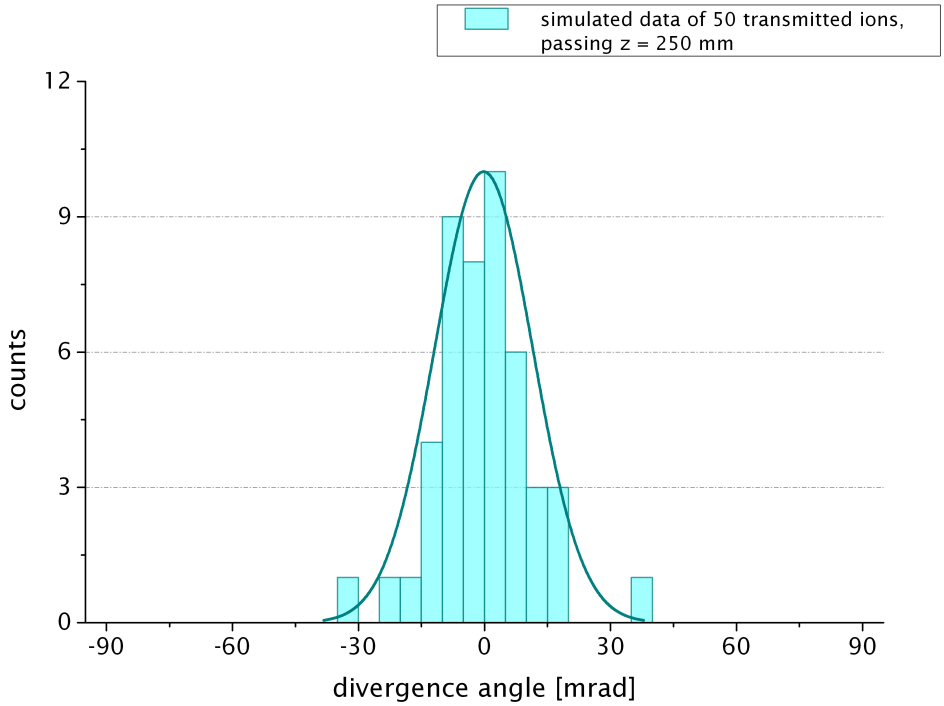

Figure 4.4: Distribution of divergence angles of ions being driven out of the quadrupole trap. The standard deviation of σ_α is ± 12 mrad.

However, the maximal velocity of objects being acceptable for the discussed interferometers, as already given in the introduction, sets a limit for the velocity. Therefore the particles cannot be accelerated arbitrarily high in order to reduce the divergence. Considering the previous results, while the angular spread of the particle beam would be in the scope of the KDTLI, for objects of 10^6 amu mass, the forward velocity is still of about two orders of magnitudes higher than required (see Fig. (1.5)).

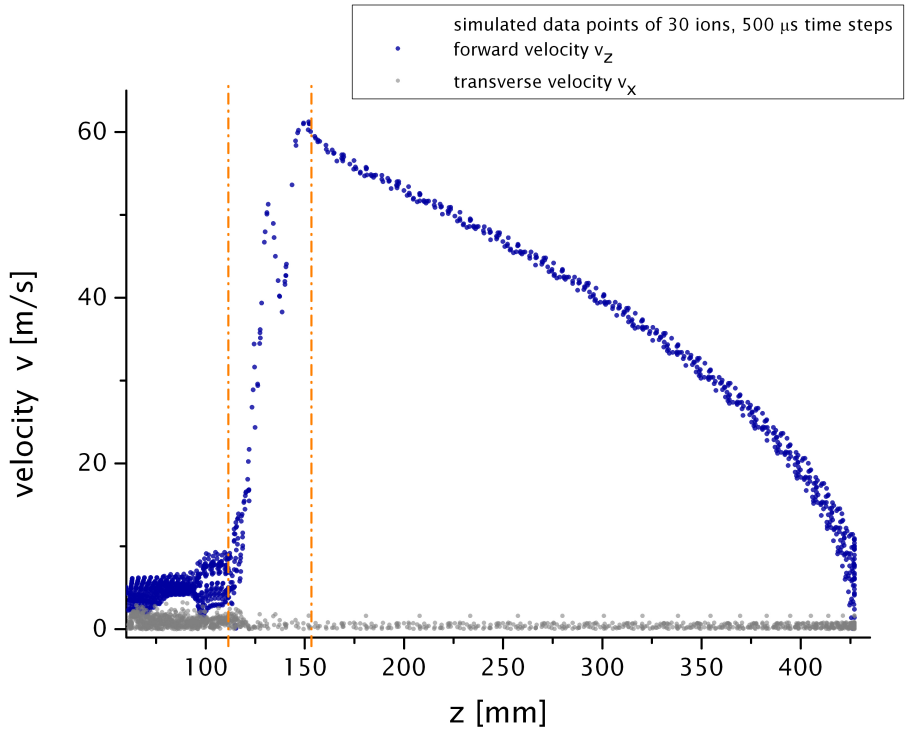

Figure 4.5: The forward and transverse velocities of the simulated ions during their acceleration outside the quadrupole. The broken orange lines indicate the position of the Einzellens.

4.3 Simulating the Quadrupole Bender

The quadrupole deflector is separately characterised to optimise transmission between the hexapole and the dodecapole trap. The bender (see Fig. (3.7)) is preceded by an Einzellens to focus the ions into the device. The particles are then deflected by the static quadrupole potential of $\pm\, U_{\text{bend}}$ onto a grounded plate in 200 mm distance behind the bender. A thick beam of 100 ions with a circular cross-section of 2 mm diameter is simulated where the initial kinetic energy spread is set to 0.25 ± 0.05 eV with inherent Coulomb repulsion. The electrodes of the bender are put alternately on $U_{\text{bend}} = \pm\, 2.35$ V and the Einzellens is set to $1.7//-5//1.7$ Volts. The ions leaving the electrostatic bender build up a broad beam, but form a quite symmetrical distribution (see Fig. (4.6) and (4.7)).

When we evaluate the divergence by looking at the angular spread of the ions, we find diagram in Fig. (4.8). The distribution has a standard deviation of $\sigma_\alpha = 19$ mrad, narrow enough for the following dodecapole trap.

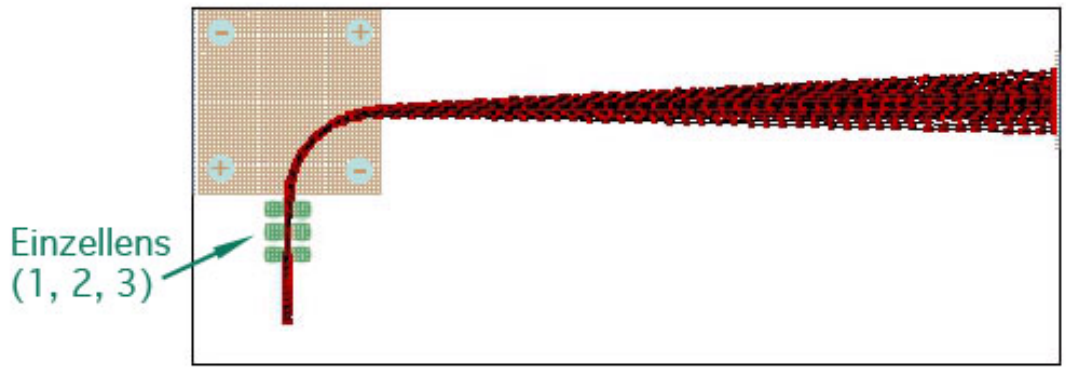

Figure 4.6: Top view of the ion trajectories exiting the quadrupole bender. Polarity of the electrodes set for positvely charged ions.

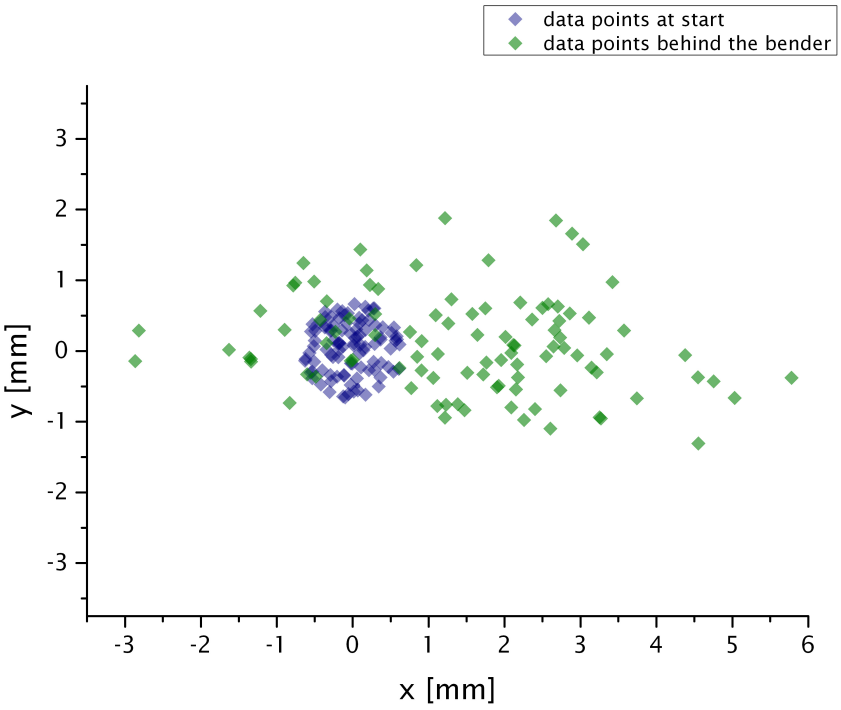

Figure 4.7: Looking into the ion beam, demonstrating the deformation of the initially circular cross-section when passing the quadrupole bender.

Further on, the forward velocity of the ions that move through the deflector is plotted

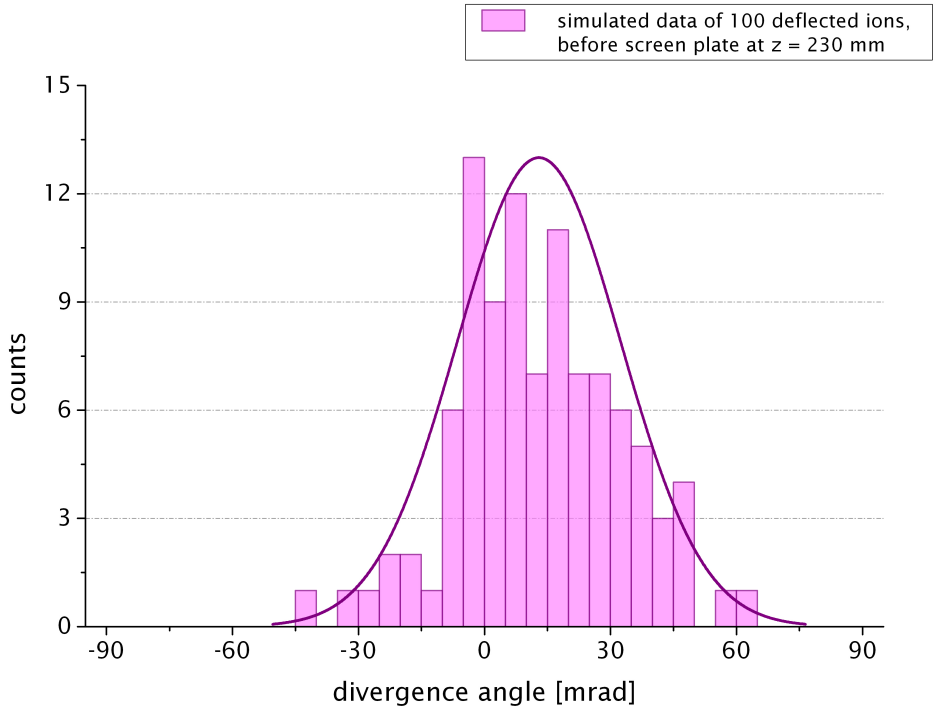

Figure 4.8: Divergence of ions being deflected by the quadrupole bender. The standard deviation of σ_α is $\pm$19 mrad.

against the recorded time steps in Fig. (4.9). Since the particles get turned about 90 degree both velocity components v_x and v_y are considered. In addition, the kinetic energy of every ion is drawn. The first peak in v_x and E_{kin} correspond to the acceleration due to the Einzellens, which acts conservatively. It skrinks when the ions leave the potential. The ions are then bend around 90 degrees, leading to a decrease in v_x with the simultaneous increase in v_y. The kinetic energy also rises, and does not completely fall back to the initial value after the ions exit the bender.

The forward velocities are higher than required for objects of 10^6 amu, however with demonstrating the conservative transfer through an Einzellens and the slight gain in kinetic energy, the quadrupole bender can be realised in this arrangement for the complete setup of the Cold Ion Trap System.

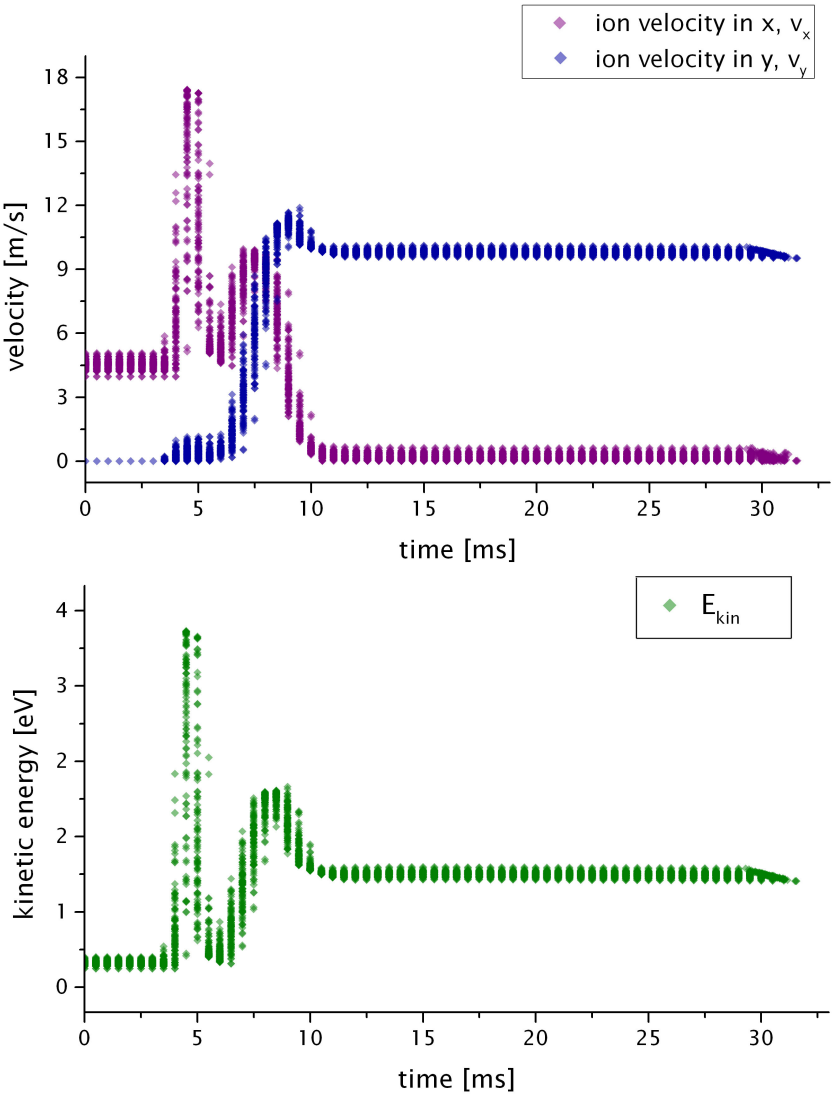

Figure 4.9: Velocity as well as kinetic energy distributions for 100 simulated ions of 10^6 amu *mass focussed by an Einzellens and transmitted by the quadrupole deflector. The first peak in* v_x *and* E_{kin} *correspond to the acceleration due to the static potential of the Einzellens. Once the ions move inside the deflector and their trajectories are bend around 90 degrees, the ions' forward velocity in x decreases with increasing velocity in y. While the kinetic energy rises again when the ions enter the bender (second peak at the green curve), it does not fully decline to its start value after the ions leave the device.*

4.4 The Cold Ion Trap System

The Cold Ion Trap System is introduced in SIMION to simulate the buffer-gas cooling and consecutive transfer of the nanoparticles. The objective of the simulation is to find parameter which allows the trapping, cooling, and ejection of the ions during the transit of the ions through the setup. In the last stage (12-pole) a dense and cold cloud of ions should be prepared. This is illustrated in Fig. (4.10). The transfer of ions inside the entire setup was optimised by performing many individual runs where the DC strength at the transferring electrodes has been varied. The simulations are conducted for several particle masses and buffer-gas pressure values (cf. Tab. (4.3), (4.4), (4.5)). The working parameters for the ion traps as in Tab. (4.1) apply.

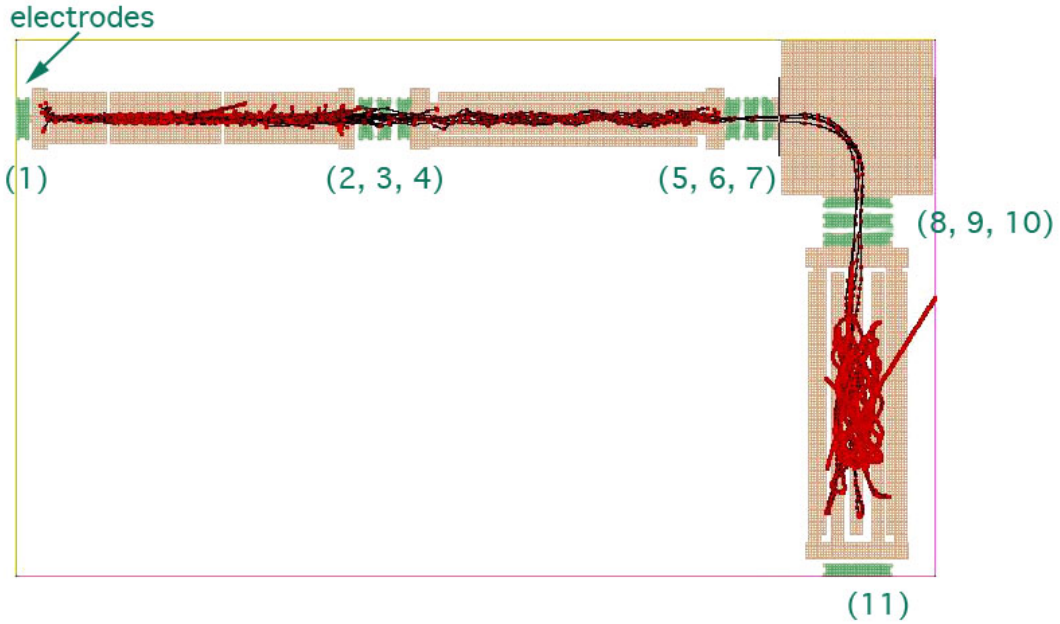

Figure 4.10: Typical simulation graph. Here 50 ions of 10^6 amu *mass were buffer-gas cooled at 295 K // 5K // 5 K. The pressure used for the thermalisation was* 10^{-3} mbar *at every cooling step.*

Particles being launched by MALDI can exhibit kinetic energies of the order of 10 eV. To shorten calculation time, we start with an ion beam of $E_{\text{kin}} = 1.0 \pm 0.1$ eV that emerges inside the quadrupole trap. The preferred direction of the ion's movement is set to the position of the following hexapole. The thermalisation times of the helium bath gas at 10^{-3} mbar and room-temperature are calculated in Tab. (4.3).

$E_{kin} = 1eV \rightarrow 295K$	ion mass [amu]	10^4	10^6	10^8
	thermalisation time [ms]	100	650	3300

Table 4.3: Thermalisation time in the quadrupole, for ions of different mass to be cooled with a He buffer-gas at 10^{-3} mbar *from a kinetic energy of 1 eV to 295 K.*

During the influx of buffer-gas, a DC gradient is stepwise ramped upon the segmented rods to shift and compress the axial extent of the ion cloud into the last third of the trap. Thereby, the ions are bunched close to the Einzellens to improve the process of particle transfer into the hexapole. The particular DC voltages on the ring electrodes have been varied to optimise the transmission efficiency, where the acceleration of the ions should not be too high. In the following the ions will be guided through the hexapole whilst a low temperature (5 K) buffer-gas pulse of 20 ms at 10^{-3} mbar pressure is applied. Then the second Einzellens (electrodes 5-7) directs the ions into the quadrupole deflector which in turn bends the beam around the corner of the construction. The thermalisation times to get ions of several masses cryogenically cold are shown in Tab. (4.4).

$E_{kin} = 295K \rightarrow 5K$	ion mass [amu]	10^4	10^6	10^8
	thermalisation time [ms]	20	130	655

Table 4.4: Thermalisation time in the hexapole, for ions of different mass to be cooled with a He buffer-gas at 10^{-3} mbar *from a kinetic energy corresponding 295 K to 5K.*

Thereafter, the particles reach the dodecapole where they should only experience slight acceleration in the transmission. If yet buffer-gas is needed, it would be appropriate to employ a velocity-selected beam of neutrals to do so, as in [Gerlich and Borodi, 2009]. However, in the course of the next sections, the usual implementation of buffer-gas will be investigated. In the case of applying less pressure, e.g. 10^{-5} mbar, the thermalisation from ions being excited due to the transfer to 5 K would require times as calculated in Tab. 4.5. Here, we assume the practical value of $E_{kin} = 200meV$ based on prior simulations.

$E_{kin} = 200meV \rightarrow 5K$	ion mass [amu]	10^4	10^6	10^8
	thermalisation time [s]	2.8	18.2	91.2

Table 4.5: Thermalisation time in the dodecapole, for ions of different mass to be cooled with a He buffer-gas at 10^{-5} mbar *from a kinetic energy of 200 meV to 5 K.*

As has been discussed in Sec. 3.7, the necessary buffer-gas influx durations which were calculated above are not expected to be convenient. Nevertheless, different settings in the final cooling trap have been simulated which should serve for the comparison and for the proof of concept. Initially 30 ions of 10^6 amu mass were simulated, again starting with a kinetic energy spread of 1.0 ± 0.1 eV for practical reasons. Each buffer-gas pulse was implemented with a pressure of 10^{-3} mbar.

This simulation disregards the thermalisation and trapping time (cf. Tab. (4.4)) of the particles in the hexapole. Here, the ions will only pass the hexapole and experience a short-time injection of buffer-gas at 5 K. Next, a comparable run has been made with the same starting conditions whereas the third buffer-gas pulse used a pressure of 10^{-5} mbar correspondent to the longer duration of gas influx of several seconds (cf. Tab. (4.5)). Both cases resulted in the successful thermalisation of the ions whose kinetic energy distributions are plotted against time in Fig. (4.11) and Fig. (4.12).

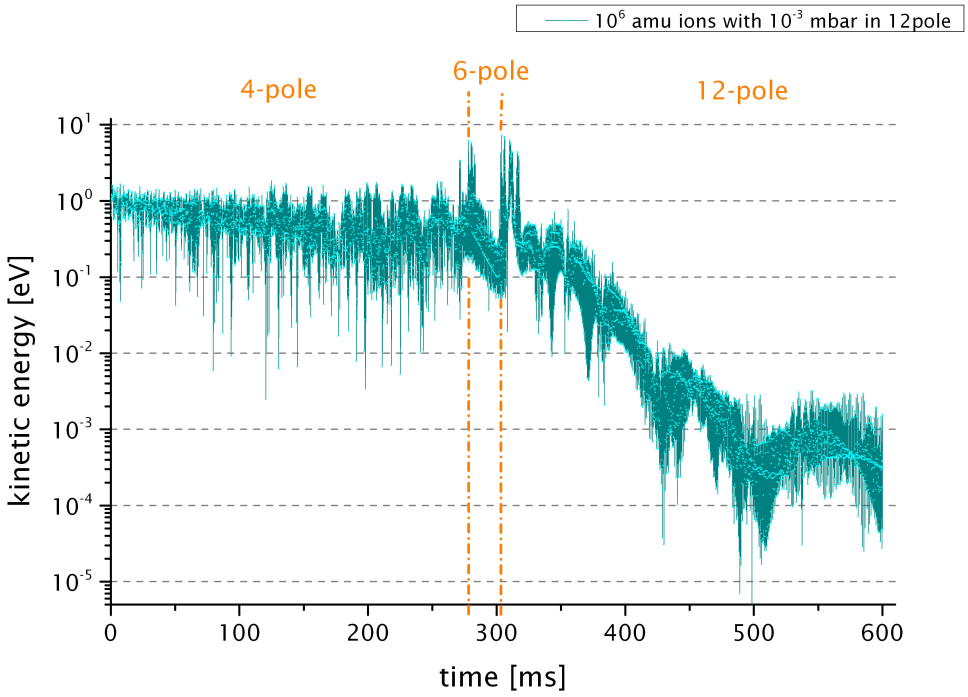

Figure 4.11: Buffer-gas cooling in Cold Ion Trap System. The gas pressure in the dodecapole trap was set to 10^{-3} mbar. *The data of 5 ions, which were successfully trapped by the dodecapole, is shown. The final value of* 0.4 meV *corresponds to a thermal value of 5 K.*

Especially in Fig. (4.11) the three cooling stages and also the passages inside the setup can clearly be seen (see orange lines). At first, the ions are buffer-gas cooled in the quadrupole where the spectrum broadens in direction of lower kinetic energy. Then, after a short excitation due to accelerating of the particles through an Einzellens (narrow peak at around 290 ms), they traverse the hexapole filled with cryogenic buffer-gas (the distribution shows an almost linear decrease in kinetic energy). Successively, the charged objects are guided by the Einzellenses and quadrupole deflector, represented by the distinct peak around 300 ms. The energy gain drops off when the ions continue to the dodecapole. Here, the last buffer-gas pulse performs the main cooling where for $p = 10^{-3}$ mbar or $p = 10^{-5}$ mbar, thermalisation to several meV or beneath occurs.

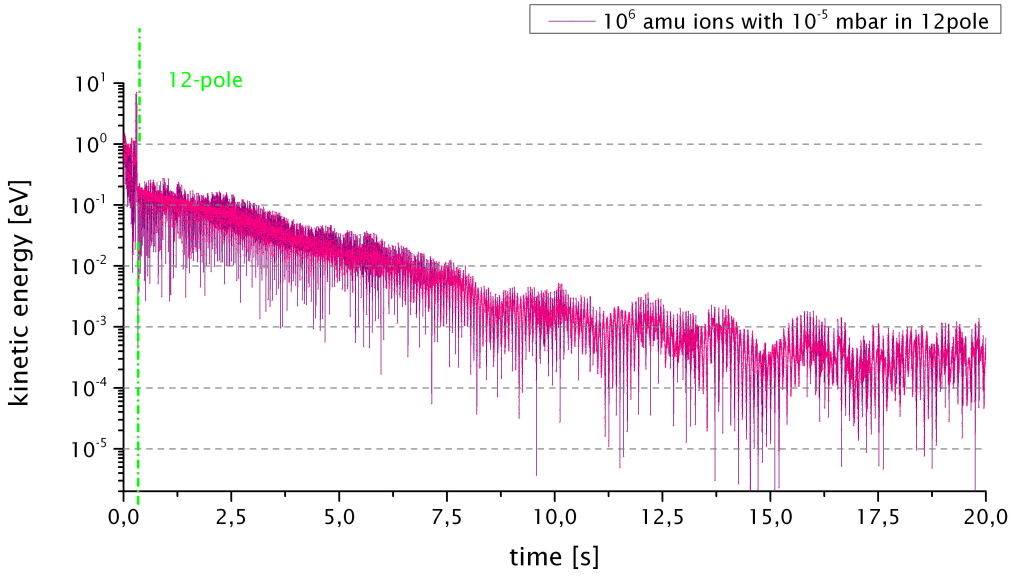

Figure 4.12: Buffer-gas cooling in Cold Ion Trap System, set the gas pressure in the dodecapole trap to be 10^{-5} mbar. *The data of a single ion, that was trapped by the dodecapole, is shown. The final value of* 0.8 meV *corresponds to a thermal value of 9 K.*

The particle cloud contracts in the course of thermalisation. We see that by plotting the radius and length of the ion distribution against time in Fig. (4.13).

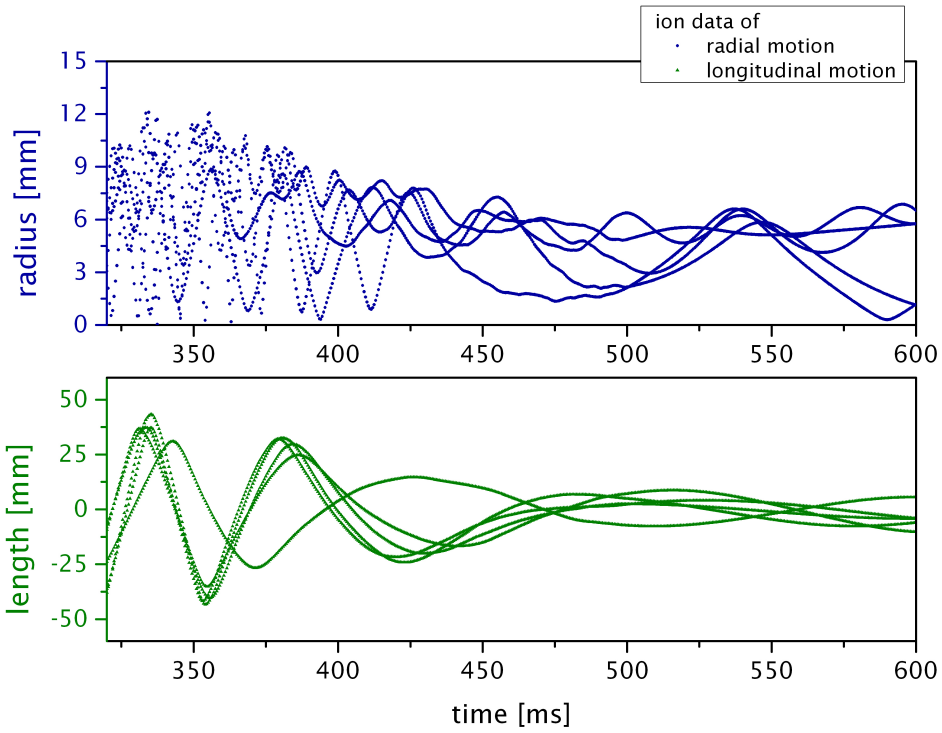

Figure 4.13: Changes in the dimensions of the cloud 30 ions of 10^6 amu *mass when employing buffer-gas cooling in the dodecapole trap at a pressure of* 10^{-3} mbar.

I conclude the analysis of the cooling procedure tracing the kinetic energy along the ion trajectory in 3D, Fig. (4.14). The kinetic energy was converted to a temperature. The graph shows thermalisation and that the lowest temperature region is always at the reversal points of the trap.

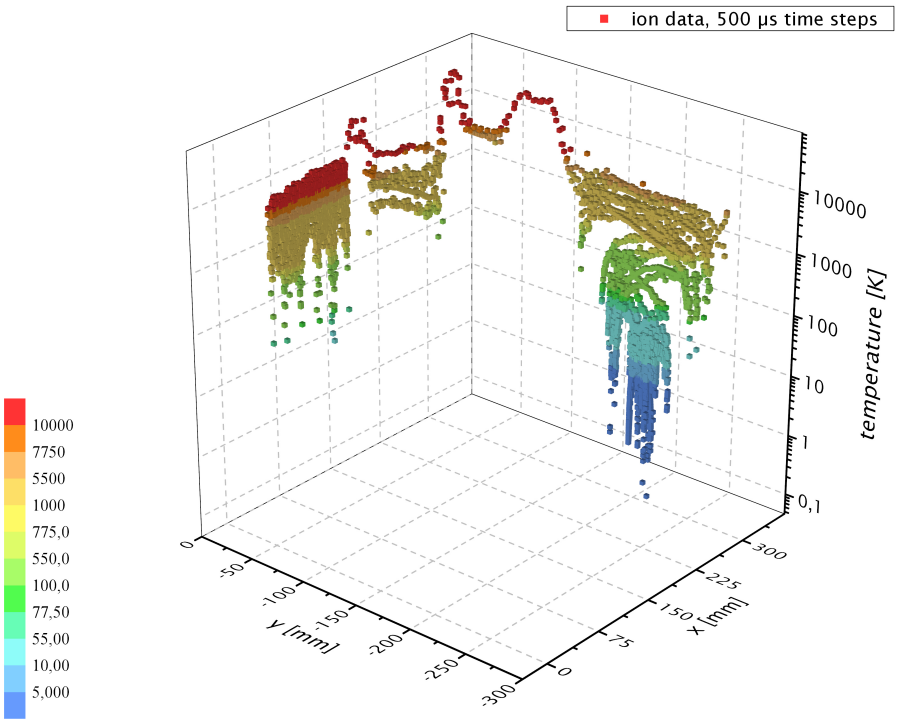

Figure 4.14: 3D graph showing the temperature that corresponds to the kinetic energy distribution of 10^6 amu *ions in the Cold Ion Trap System against the x and y coordinates.*

4.5 Simplified setup: Cold hexapole arrangement

With the need of successive cooling of the to-be-manipulated macromolecules, the concept of a consolidated setup of several ion optical elements, serving as progressively cooling stages, has been conceived. In principle, already the conjunction of a quadrupole with a hexapole trap provides the conditions for efficient buffer-gas cooling of mass-selected ion bunches. To investigate the feasibility of the cooling process in the simplified setup of a cold hexapole, simulations analogous to before were performed.

For the reduction of gas ballast aerodynamic lenses [Liu et al., 1995, Zhang et al., 2002] could be employed at the outlet of the setting, which is represented by the Einzellens behind the hexapole. Additionally, a set of circular collimating electrodes ("apertures") with decreasing opening diameter is included in the simulation of this linear arrangement (see Fig. (4.15)).

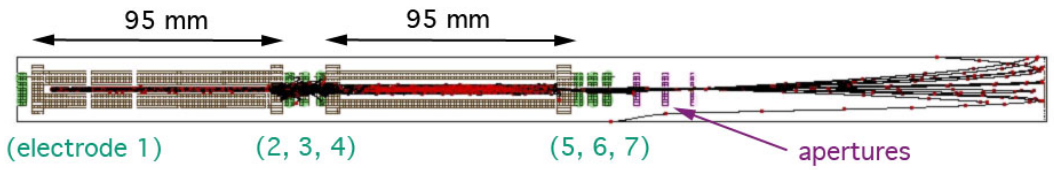

Figure 4.15: The simulated cold hexapole arrangement with 10^4 amu *ions. The electrodes (1), (2) and (4), (5) were set to* $V_{EC} = 20$ V *to work as endcaps. If switched to Einzellens, three neighboring electrodes were put on - 10 V || 2 V || -10 V.*

In respect of the possibility to apply a linear ion trap device to the KDTLI, ions of 10^4 amu mass were simulated for giving a hint about the feasibility of the regarded configuration. Therewith the transmitted ions are analysed in their kinetic energy and forward velocity distributions.

We start with a beam of 50 ions with a distribution of 0.25 ± 0.05 eV kinetic energy inside the quadrupole trap. Considering the thermalisation times for particles at 10^4 amu mass in Tab. (4.3), (4.4), (4.5), the charged objects are subject to buffer-gas pulses of some milliseconds inside the quadrupole and the hexapole. After buffer-gas cooling, the electrode Nr. 5 at the hexapole is switched together with the remaining ring electrodes to act as an Einzellens. The apertures are also set onto a small attractive potential (- 1 Volts). With this small acceleration, the ions are drifting out of the setup to impinge

onto a plate situated 200 mm behind. Here, the plate was implemented to act as a screen to look at the divergence, but is not necessarily required.

Similar to the treatment in Sec. 4.4 the kinetic energy distribution of the successfully transferred and cooled particles is illustrated in Fig. (4.16) along with the ion velocity. A spatially resolved graph can be generated where the kinetic energy is plotted against the axial position z. Once more the cooling stages are clearly distinguishable in Fig. (4.17).

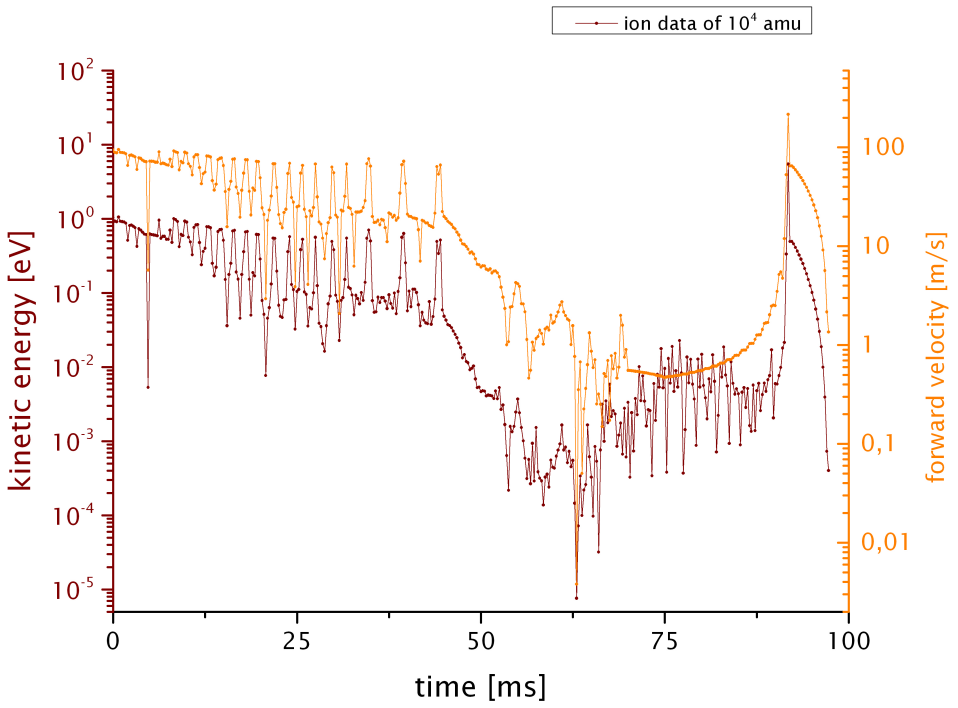

Figure 4.16: Velocity and kinetic energy distribution of 10^4 amu *mass ions in the cold hexapole trap. The peak in both curves around 90 ms corresponds to the acceleration of the ions and the DC electrodes.*

Both diagrams show a similar outcome related to the analysis of the velocity distribution in Fig. (4.5) of Sec. 4.3. It seems, that once ejected from the trap, the particles assume the kinetic energy they had before approaching the Einzellens (electrodes 5, 6, 7). According to this, the simplified cold trap arrangement would be feasible as well to cool down nanoparticles in the high mass range. However, without

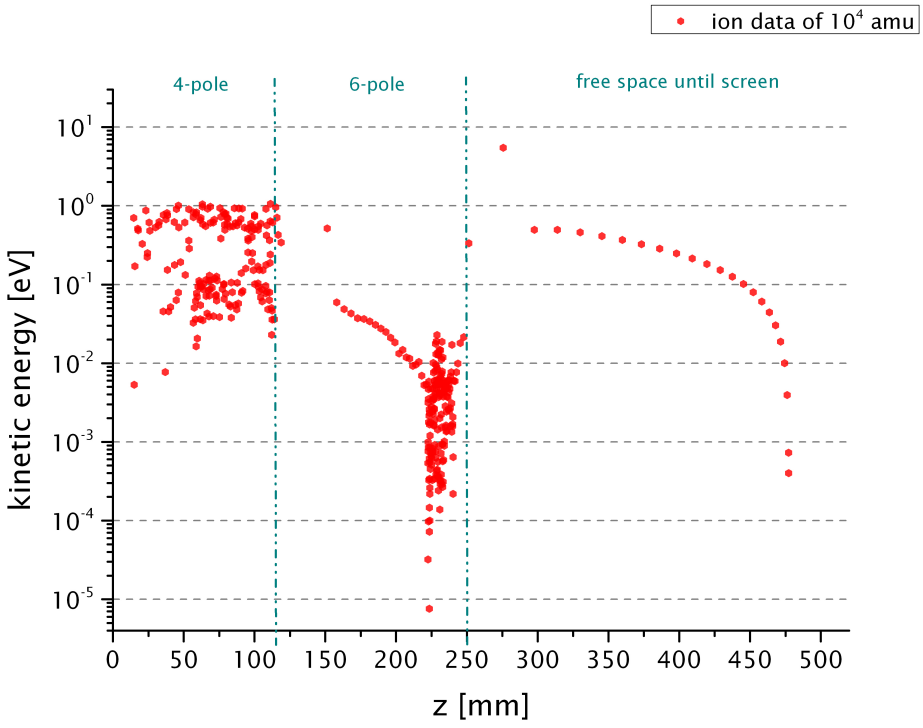

Figure 4.17: Spatially resolved graph showing the kinetic energy distribution of 10^4 amu *ions, buffer-gas cooled inside the cold hexapole, and after eject ion.*

an apparent channel to diffuse the translational energy gained due to the ejection, those results are uncertain. If the nanoparticles remain internally cold and are slowed afterwards in a proper way, this setup could still be of interest for an application with the KDTLI.

Chapter 5

Cooling Technology

5.1 Cryogenic setup

In order to operate an ion trap at very low temperatures (below -270°C or 3 K) it is indispensable to implement a proper environment. The materials have to withstand rather strong temperature gradients, be resistant to thermal cycling and as a matter of the experiment, be appropriate for vacuum. The setup has to shield against heating, too.

Our cryogenic design is similar to a system employed in the group of T. Pfeifer in Heidelberg [Schwarz, 2012, Schwarz et al., 2012]. Thermal radiation shields suspended by thin material spokes are robust and flexible enough to isolate mechanical vibrations. As shown in Fig. 5.2, the temperature decline is inbound, where a frame at room-temperature (295 K) holds the two-stage shielding structure. Each closed box corresponds to a cooling stage of the connected pulse tube refrigerator (PTR)[1] removing heat load with a power of $P_{\mathrm{PTR,\,i}} = 30$ W at 65 K for the first, and $P_{\mathrm{PTR,\,ii}} = 0.5$ W at 4 K for the second stage respectively.

Besides vacuum suitability, efficient thermal contact with the cryocooler has to be ensured. The setup together with the gas and electrical feedthroughs should be comprised of a material with very good thermal conductivity κ. Copper (especially OFHC *oxygen-free high thermal conductivity* copper) with $\kappa = 350 - 400\ \frac{\mathrm{W}}{\mathrm{m \cdot K}}$ is the metal of choice for cryogenic applications [Van Sciver, 2012]. In the case of electric insulating material the aluminium oxide sapphire Al_2O_3 and the ceramic shapal would

[1] Model RP-062ES from the company *Sumitomo Heavy Industries, Ltd.*

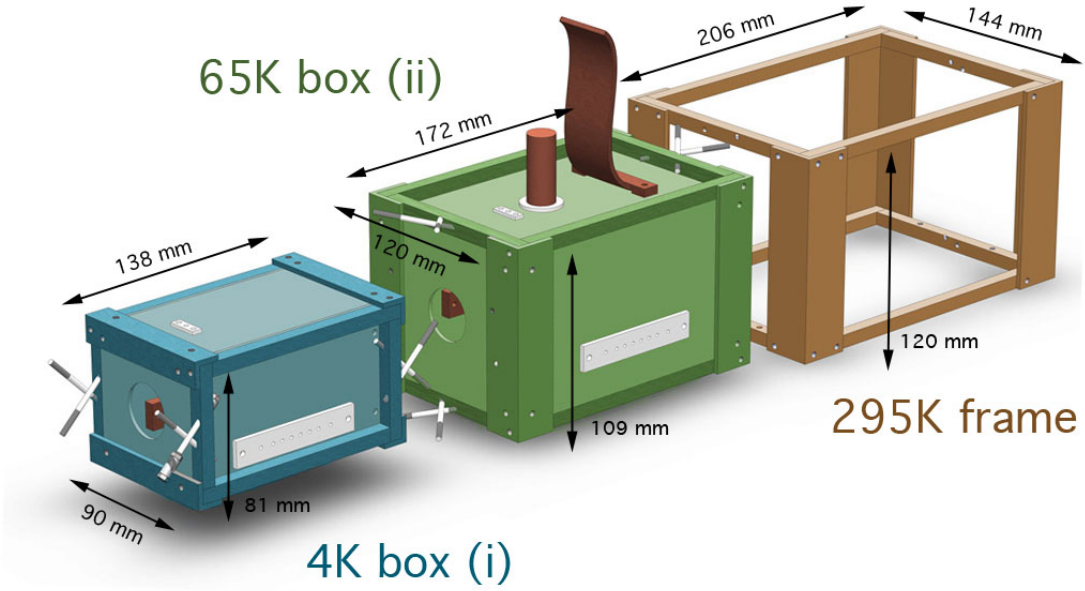

Figure 5.1: Exploded view of the interlaced cryogenic setup.

be appropriate.

If different materials are combined, the thermal expansion properties have to be considered. Here, the components were chosen to consist of customary stainless steel parts for the frames and 2 mm thin copper plates for the shields. Both metals have similar expansion factors [Shackelford and Alexander, 2010].

While thermal conduction between the cryocooler and the shield is essential, heat bridges among the boxes have to be prevented. The suspension of the shield is made from thin PEEK rods, with thermal conductivity of $\kappa = 0.25\ \frac{\mathrm{W}}{\mathrm{mK}}$ [der Vegt and Govaert, 2003].

The heat conduction from one box to the other is calculated from the temperature gradient ΔT in the material of cross-section A, as in [Pobell, 1996], to be

$$\dot{Q} = -\kappa\, A\, \frac{\Delta T}{l} \tag{5.1}$$

where $\dot{Q}$ is the amount of heat transferred per unit time [W] and l is the length of the

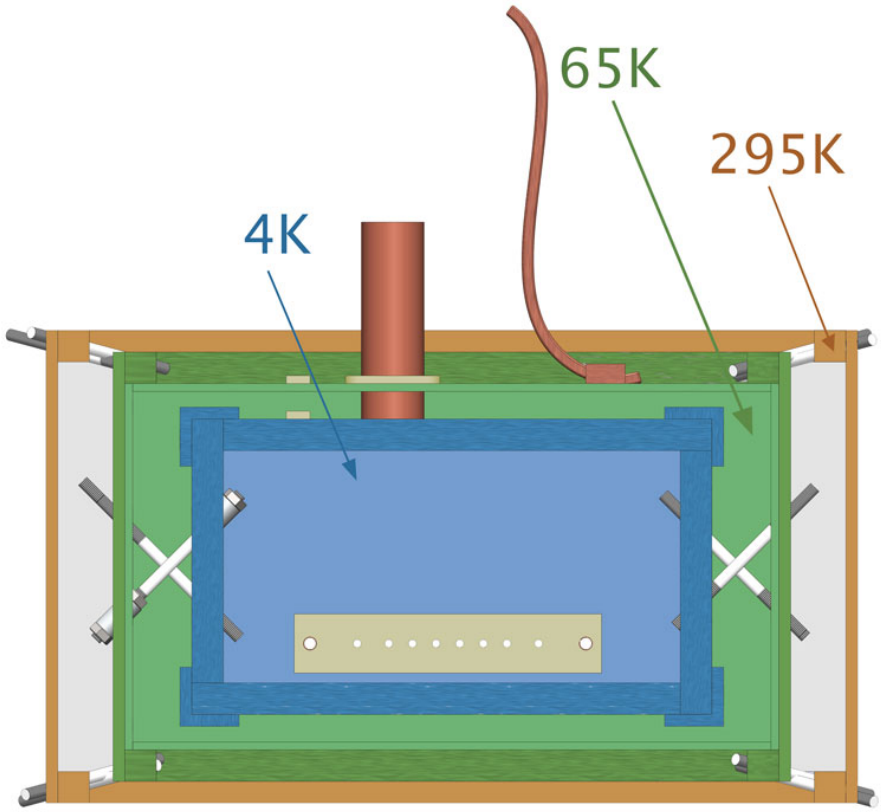

Figure 5.2: Schematic view of the cryogenic shields.

regarded object. For a total of 8 PEEK spokes of 3 mm diameter and 55 mm length holding each box, this gives a thermal load of $P_{\text{conduction, i}} = 0.24$ W for the first, and $P_{\text{conduction, ii}} = 0.07$ W for the second cooling stage.

The cryogenic container is designed to shield the thermal radiation, where the absorbed black body radiation power P is given by

$$P = \epsilon(\nu)\,\sigma A\left(T^4 - T_0^4\right) \tag{5.2}$$

with $\epsilon(\nu)$ being the emissivity of the material in dependence of the frequency ν, and σ is the Stefan-Boltzmann constant, A is the radiating surface area, and the difference in T being the deviation from an ambient temperature.

The area of the first cooling shields is $A_{65\text{K box}} = 0.085$ m^2 while for the second stage it is $A_{4\text{K box}} = 0.047$ m^2. Considering the copper plates to be oxidised, an emissivity of

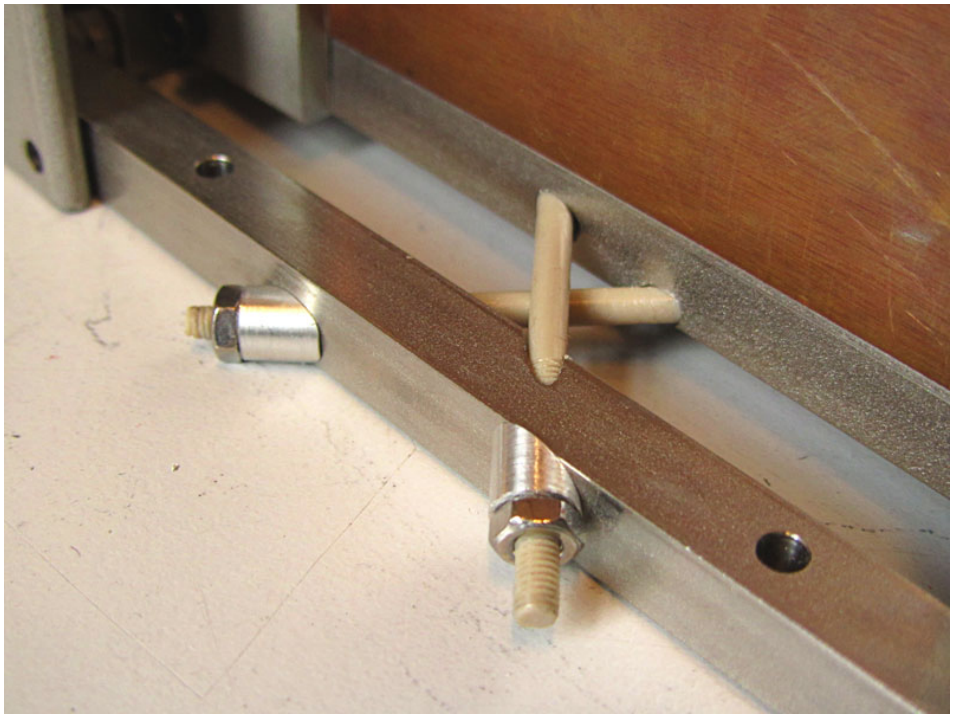

Figure 5.3: A detail of the PEEK suspension.

$\epsilon_{Cu,ox} = 0.87$ is taken into the calculation. The emittance power can then be estimated to be $P_{radiation,\,Cu,\,i} = 33.8$ W for the outer box and $P_{radiation,\,Cu,\,ii} = 60$ mW for the 4K box.

Since the external heat leak is quite extensive, concerning the moderate power of the pulse tube cooler, it has been expedient to use several layers of aluminised Mylar-Foil for thermal insulation[2]. This material has a very low emissivity of $\epsilon_{Myl} = 0.044$ and is well suited to reflect most of the black body radiation [Domen, 1991]. Calculating the radiation power of the Cryobox again gives $P_{rad,\,Myl,\,i} = 1.7$ W and $P_{rad,\,Myl,\,ii} = 3$ mW for the first and second stage respectively.

On the downside, multi layer insulation is known to be a significant outgassing source [Glassford and Liu, 1980, Glassford et al., 1984] which affects the cooling effectiveness in return. To balance both effects a trade-off between sufficient radiation shielding and minimisation of vacuum compromising materials has been made.

[2] This mylar foil consists of *biaxially-oriented polyethylene terephthalate* [Amborski and Flierl, 1953]

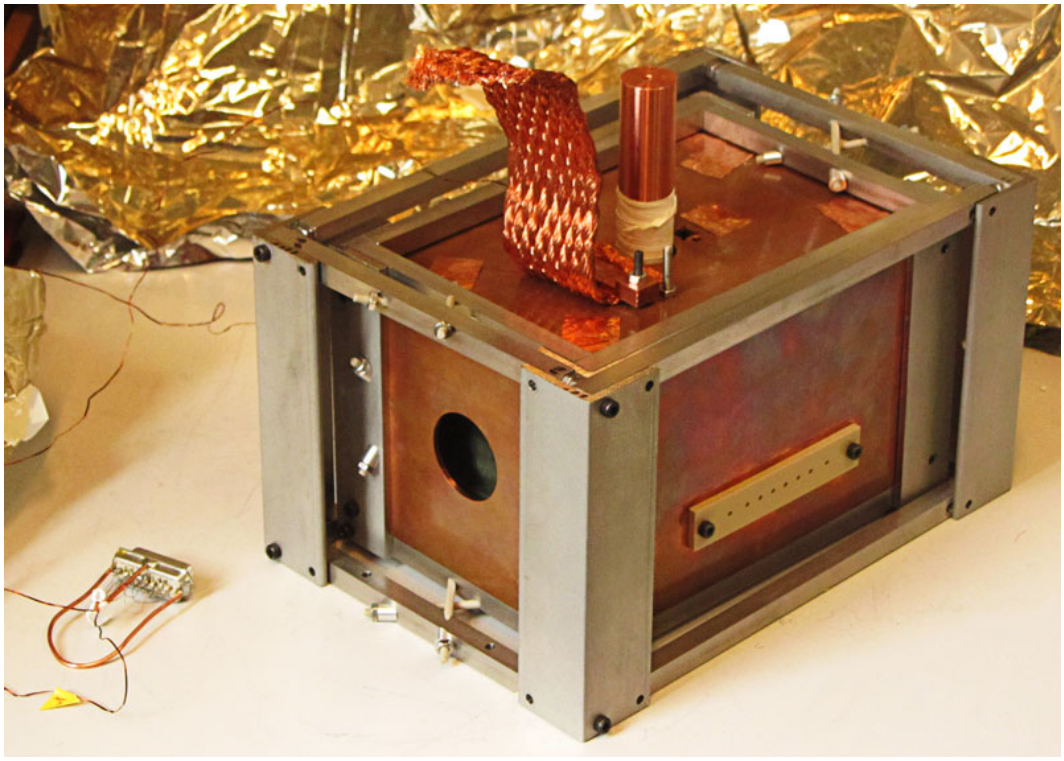

Figure 5.4: The assembled cryogenic setup - "Cryobox".

Finally, we can estimate the time it takes for the Cryobox to cool down. Considering the power of the pulse tube cooler and the specific heat capacity of the associated materials. We find

$$t = \frac{c \cdot m\,\Delta T}{P_{\text{eff}}} \tag{5.3}$$

where c stands for the specific heat capacity[3] and m for the mass of the box. ΔT is the temperature gradient that can be achieved by the cooler of power P.

We regard the cooling process to be double-staged, where the two seperated boxes can be treated individually. Thus, two points in time can be calculated: when (i) the first box reaches the temperature level at 65 Kelvin and (ii) the final temperature of 4 Kelvin is accomplished for the second. Since the Cryobox is composed of stainless steel and copper, the specific heats of both will be approximated by $c_{295K\to100K} \simeq 400\ \frac{\text{J}}{\text{kgK}}$,

[3] Actually the specifiy heat capacity is a function of temperature.

$c_{100K\to65K} \simeq 170\ \frac{\mathrm{J}}{\mathrm{kgK}}$ and $c_{65K\to4K} \simeq 85\ \frac{\mathrm{J}}{\mathrm{kgK}}$ for lower temperatures [Marquardt et al., 2002, Franck et al., 1961]. With the full power of the cryocooler and the mass of $m_{4\mathrm{K\,box}} \simeq 1.6$ kg and $m_{65\mathrm{K\,box}} \simeq 2.8$ kg for the boxes (i) and (ii), this would lead to cooling times of $t_{\mathrm{i}} = 2.2$ h for cooling the first and $t_{\mathrm{ii}} = 5.9$ h the second stage respectively.

However, the cooling efficiency is subject to leakage which has been estimated before (see above) and will be factored in the cooling power by subtracting it

$$\mathrm{P_{eff}} = \mathrm{P_{PTR}} - \mathrm{P_{radiation}} - \mathrm{P_{conduction}} \tag{5.4}$$

Hence the corresponding cooling power is (i) $\mathrm{P_{eff,i}} \simeq 28$ W and (ii) $\mathrm{P_{eff,ii}} \simeq 0.4$ W, leading to corrected cooling times of $t_{\mathrm{eff,\,i}} = 2.4$ h and $t_{\mathrm{eff,\,ii}} = 7.2$ h.

5.2 Cooling test

In the following, results of the cooling performance of the Cryobox will be presented. To measure the temperature within the cryogenic setup two silicon diodes[4] were connected to the two boxes. They were read by temperature controllers [5].

An additional sensor was connected to the second stage of the pulse tube (*cold head*) for monitoring the cooling progress. The simultaneous measurement of three temperature values and the base pressure of the vacuum chamber has been automatically executed by a self-written LabView program. The outcome of the continuous monitoring of all sensors every 10 seconds is shown in Fig. 5.5.

The point of turning off the cooler is clearly recognizable by the short-term pressure increase and the rising temperature of the cold head (broken blue curve). Although the desired low temperatures were not yet achieved at the walls of the Cryobox (due to remaining heat leakages at the cables), the setup clearly features a compact and convenient design for holding a cryogenic apparatus.

The measurement of the cooling process demonstrates the expected behaviour of the temperature and pressure curves, albeit the desired cooling performance of the Cryobox could not be achieved until now. Here, the main sources of error were still existing heat

[4] Model DT-670B-CU from the company *LakeShore Cryotronics, Inc.*
[5] Model 331 and 335

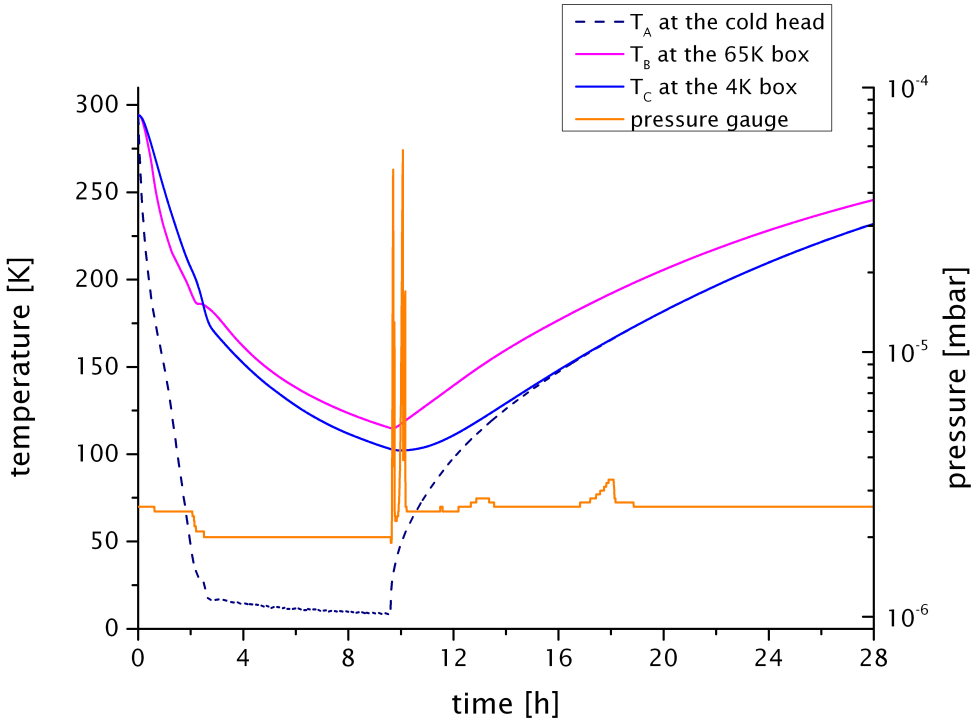

Figure 5.5: Cooling performance of the Cryobox. The broken line monitors the cold head. The base pressure is indicated by the orange line. The temperature at both diodes is continously recorded. The pink line stands for the 65 K box and the blue one for the 4 K box. After 9h the pulse tube cooler was switched off.

bridges between the temperature stages due to thermally conducting cables and yet insufficient thermal insulation.

5.3 Vibrational analysis

In addition to the cooling experiments a demonstration of the efficiency of the threaded design to decouple the construction from exterior mechanical vibrations, e.g. jittering of turbomolecular pumps, measurements with an accelerometer was done. For this purpose the Cryobox was placed near the vibrating of the miscellaneous technical equipment. An piezoelectric sensor[6] was used to determine the machine-driven noise. The sensor was at first mounted onto the optical table the instruments were standing on, then on the room-temperature (295 K) frame, and finally on top of the 65 K box.

[6] Model 480E09 from the company *PCB Piezotronics, Inc.*

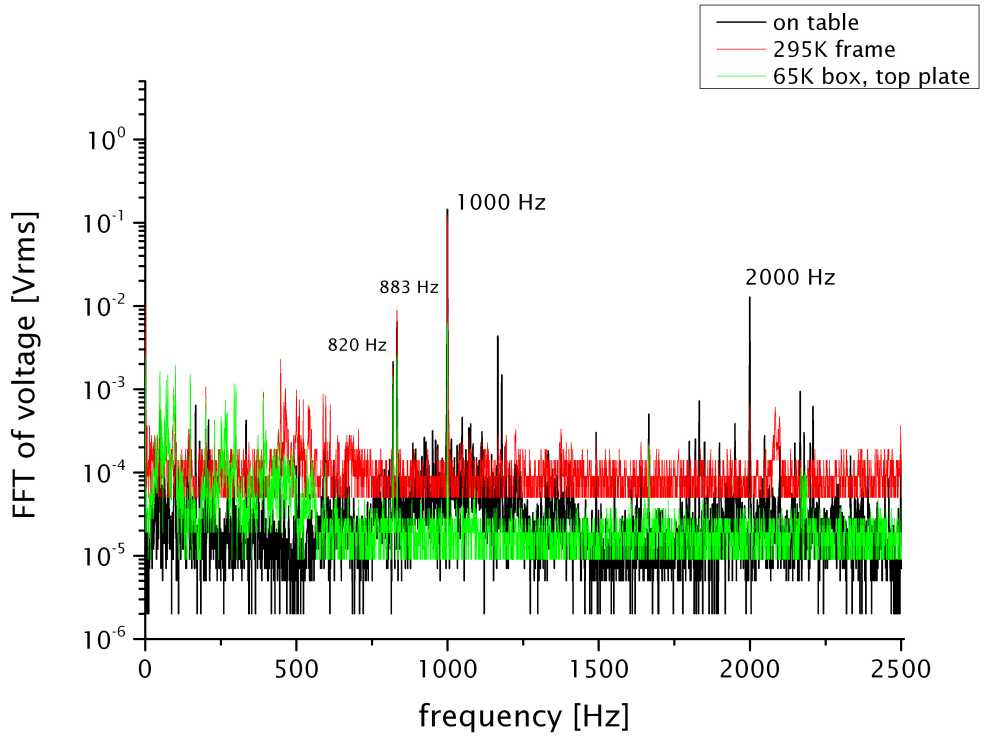

Figure 5.6: Measurement of the mechanical vibrations at the Cryobox. For a range of 0 – 2500 Hz *the frequencies are recorded by the accelerometer[6]. The vibrational background at the optical table is shown as the black line. Higher frequencies, as for the doubled signal of a turbomolecular pump at* 2000 Hz*, are softened at the 300 K frame (red curve). Damping by more than one order of magnitude is attained at the top plate of the 65 K box (green curve).*

A signal reduction was clearly visible when changing from the unfiltered vibrations to the Cryobox (see Fig. 5.6). While already the sturdy frame of the setup is able to dampen some vibrations, the suspension of the first cooling shield enhances the isolation effect by up to a factor of 10 or more in comparison to the background.

Chapter 6

Outlook & Conclusion

Our considerations on how to implement the designed setup in a matter-wave experiment lead to two probable designs. On the one side, the cooled particles could be extracted from a cold multipole arrangement, undergoing (photo)neutralisation and collimation, to be further passed on to the interferometric region. Otherwise, it would be conceivable to cool the particles in the Cold Ion Trap System and to perform the diffraction directly inside the last trap. Both options, their advantages as well as possible obstacles will be briefly discussed in this chapter.

Interferometry behind the trap

We start by focussing on the possibility of constructing a source for a generalised TL interferometer with an ion-based source of mass-selected nanoparticles that are internally and externally cold. As discussed in the introduction, all interferometers necessitate low velocities for massive objects, both normal and parallel to the grating. The particle velocity can be reduced by buffer-gas cooling inside the ion trap.

KDTLI and OTIMA require also rather collimated beams. Since charged particles accumulate various velocity components due to their motion inside the RF-potential, the leaving ions are quite divergent, even if the ion cloud was initially confined on the trap axis (e.g. in a quadrupole). When passing the fringe fields at the end of the trap electrodes, the ion beam can be significally broadened. Therefore, focussing and collimation of the transmitted ions is necessary. This can be achieved with a set of Einzellenses at the exit of the trap, or by a strong acceleration into the forward direction. The previous analysis in Sec. 4.2, determined divergence angles in the mrad range for

ions emitted from a cold hexapole. This is acceptable for KDTLI (cf. Eq. (1.5), (1.4)). The kinetic energy gained leads, however, to an enhanced forward velocity. Moreover the ion trap is more likely to be operated as a pulsed source which condradicts the requirement of KDTLI to use a continous source.

Interferometry inside the trap

Rather than extracting the cooled particles, interference could be performed in the trap itself by illuminating the ion cloud with three successive laser pulses, followed by particle detection. The nanoparticles could be loaded, manipulated and cooled in the negative-ion mode and then be illuminated by the first laser grating which neutralises the diffracted molecules. Extracting out the remaining anions by the use of an extracting voltage, the neutral particles are illuminated again by the second pulsed laser grating. Here, the transmitted particles are positively charged who will be again removed from the active area. The neutral molecules which are ionised by the third laser grating are then chosen for detection, whereas the ion trap will be switched to positive-ion mode to re-trap them.

For this configuration the Cold Ion Trap System was designed in such a way that at the end of the final trap the interference mirror is to be mounted. In order to have an accessible optical path through the ion cloud towards the mirror it is possible to implement a broad quadrupole bender (cf. Sec. 3.6). The length of the dodecapole trap is mainly determined by the coherence length l_C of the laser grating. It should not exceed $l_C/2$ as all ions should be hit by the standing laser wave and contribute to the particle interference.

Further considerations

An additional cooling process would certainly increase the feasibility of a future interference experiment. One may consider to combine the ion trap with cavity-assisted laser cooling for further velocity damping [Smith et al., 2005].

Résumé

Within the scope of this master thesis, the essentials of an accumulative device are presented which will be able to prepare cold and slow nanoparticles in the high to ultra-high mass range. At the same time it holds the possibility of enclosing an interference

experiment inside the setup as well. Exploiting buffer-gas cooling in radiofrequency-driven ion traps allows to not only to damp the translational energy of the captured objects but also to cool their internal excitation through thermalisation to cryogenic temperatures.

An ion-based system source for future matter-wave experiment has been designed that, aside from estimations, was tested in its feasibility with ion-optical simulations. As the simulations showed, singly-charged particles of 10^4 to 10^6 amu mass can efficiently be thermalised with 5 K helium buffer gas and transferred between the traps.

Furthermore, a two-stages thermal shielding structure has been constructed and tested in the laboratory. With gaining experience about the challenges in cryogenic technology, the cooling performance of the individual stages has been studied. Moreover, the stability of the construction against mechanical shocks was demonstrated.

Finally, this work sketches the outline of possible implementations of the regarded designs whether the cold multipole arrangement serves as a preparation device for an existing interferometer or, with a maybe more spacious construction, contains the interferometric region even within itself.

Appendix A

SIMION Simulation Parameters

```
    The SIMION [Dahl, 2000] lua workbench program for simulating the Cold Ion Trap System.
For the elastic ion-neutral collisions the HS1 model by collision_hs1.lua[1]
    for SIMION 8 (REVISION-6-2009-10-02) was used.

simion.workbench_program()
    local HS1 = simion.import "collision_hs1.lua"

Variables adjustable only at beginning of flight:
    adjustable phase_angle_deg = 0.0     entry phase angle of ion [deg]

    adjustable _freq_quadru = 1.96E+4
    adjustable _freq_hexa = 3.07E+4
    adjustable _freq_dodeca = 4.91E+4     RF frequency of 4 / 6 / 12-pole [Hz]

    adjustable _rf_quadru = 150
    adjustable _rf_dodeca = 150
    adjustable _rf_hexa = 150     RF amplitudes of 4 / 6 / 12-pole [V]

Static potentials (all voltages are given in [V]):
    adjustable _dc1 = 0.5
    adjustable _dc2 = 1
    adjustable _dc3 = 1.5     at the 4-pole segments

    adjustable endcap_dc = 20     at the endcaps
    adjustable endcap_push_dc = 30     higher voltage for pushing out ions

    adjustable lens1_dc = -15     at outer lens electrodes
```

[1] Copyright 2004-2012 Scientific Instrument Services, Inc.

```
    adjustable lens1_m_dc = 1     at center lens electrode, einzellens # 1

    adjustable lens2_dc = -15     at outer lens electrodes
    adjustable lens2_m_dc = 1     at center lens electrode, einzellens # 2

    adjustable bend_dc = 1.5     at quadrupole bender
    adjustable lens_bend_dc = 0     at bender ring electrodes, optional

    adjustable lens3_dc = -15     at outer lens electrodes
    adjustable lens3_m_dc = 1     at center lens electrode, einzellens # 3


Timing parameters (all times are given in [μs]):
    adjustable step1 = 20000
    adjustable step2 = 40000
    adjustable step3 = 60000
    adjustable step4 = 80000     timesteps for toggling the 4-pole segments

    adjustable endcap1_2_on = 1000     endcaps at 4-pole switched on

    adjustable lens1_on = 105000     endcap # 2 at 4-pole off / einzellens # 1 on
    adjustable start_hexa = 105000     6-pole switched on
    adjustable endcap4_on = 105000     endcap # 4 (backside) at 6-pole on

    adjustable endcap1_off = 115000     endcap # 1 (frontside) at 4-pole off
    adjustable stop_quadru = 115000     4-pole switched off
    adjustable lens1_off = 115000     einzellens # 1 switched off

    adjustable lens2_on = 130000     einzellens # 2 at 6-pole on
    adjustable bend_on = 130000     q-bend switched on
    adjustable lens3_on = 130000     einzellens # 3 at 12pole on
    adjustable start_dodeca = 130000     12-pole switched on
    adjustable endcap6_on = 130000     endcaps # 5 and # 6 at 12-pole switched on

    adjustable lens2_off = 160000     einzellens # 2 off
    adjustable lens3_off = 160000     einzellens # 3 off
    adjustable stop_hexa = 160000     6-pole switched off
    adjustable endcap3_off = 160000     endcap # 3 (frontside) of 6-pole off
    adjustable bend_off = 160000     q-bend switched off
    adjustable switch_off = 400000     12-pole and final switch off

Parameters for the buffer gas
(times in [μs], pressures in [Pa] and temperatures in [K]):
```

```
    adjustable _BGtime1 = 0         buffer gas on
    adjustable _BGtime2 = 100000     buffer gas off ...pulse 1 at 4-pole

    adjustable _BGtime3 = 110000     buffer gas on
    adjustable _BGtime4 = 130000     buffer gas off ...pulse 2 at 6-pole

    adjustable _BGtime5 = 175000     buffer gas on
    adjustable _BGtime6 = 225000     buffer gas off ...pulse 3 at 12-pole

    adjustable bg_pressure1 = 0.1
    adjustable bg_pressure2 = 0.1
    adjustable bg_pressure3 = 0.001     pressures of first, second and third bg pulse

    adjustable _temperature_k_4 = 295.0
    adjustable _temperature_k_6 = 5.0
    adjustable _temperature_k_12 = 5.0     temperature of the buffer gas


function HS1.pressure()
    return
        (ion_time_of_flight >= _BGtime1 and ion_time_of_flight <= _BGtime2) and bg_pressure1
        or (ion_time_of_flight >= _BGtime3 and ion_time_of_flight <= _BGtime4) and bg_pressure2
        or (ion_time_of_flight >= _BGtime5 and ion_time_of_flight <= _BGtime6) and bg_pressure3
        or 0
    end

function HS1.temperature()
    return
        (ion_time_of_flight >= _BGtime1 and ion_time_of_flight <= _BGtime2) and
        _temperature_k_4 or
        (ion_time_of_flight >= _BGtime3 and ion_time_of_flight <= _BGtime4) and
        _temperature_k_6 or
        (ion_time_of_flight >= _BGtime5 and ion_time_of_flight <= _BGtime6) and
        _temperature_k_12 or 295.0
    end

    local last_pe_update = 0.0     last potential energy surface update time
```

SIMION segment called by SIMION to set adjustable electrode voltages in the current potential array instance. NOTE: this is called frequently, multiple times per time-step (by Runge-Kutta), so performance concerns here can be important.

```
function segment.fast_adjust()
    local omega_4 = _freq_quadru * (1E-6 * 2 * math.pi)
    local omega_6 = _freq_hexa * (1E-6 * 2 * math.pi)
```

```
    local omega_12 = _freq_dodeca * (1E-6 * 2 * math.pi)
    local theta = phase_angle_deg * (math.pi / 180)

    local tempvolts_4 = sin(ion_time_of_flight * omega_4 + theta) * _rf_quadru
    local tempvolts_6 = sin(ion_time_of_flight * omega_6 + theta) * _rf_hexa
    local tempvolts_12 = sin(ion_time_of_flight * omega_12 + theta) * _rf_dodeca


Apply adjustable voltages to rod electrodes.

4-pole ion trap RF electrodes (rods & power rings):
    adj_elect01 = ion_time_of_flight < stop_quadru and tempvolts_4 or 0     power ring I

    adj_elect02 =
        ion_time_of_flight < step1 and tempvolts_4 or
        (ion_time_of_flight >= step1 and ion_time_of_flight < step2) and _dc1 + tempvolts_4 or
        (ion_time_of_flight >= step2 and ion_time_of_flight < step3) and _dc2 + tempvolts_4 or
        (ion_time_of_flight >= step3 and ion_time_of_flight < step4) and _dc3 + tempvolts_4 or
        (ion_time_of_flight >= step4 and ion_time_of_flight < stop_quadru) and
        _dc3 + tempvolts_4 or 0

    adj_elect03 =
        ion_time_of_flight < step2 and tempvolts_4 or
        (ion_time_of_flight >= step2 and ion_time_of_flight < step3) and _dc1 + tempvolts_4 or
        (ion_time_of_flight >= step3 and ion_time_of_flight < step4) and _dc2 + tempvolts_4 or
        (ion_time_of_flight >= step4 and ion_time_of_flight < stop_quadru) and
        _dc2 + tempvolts_4 or 0

    adj_elect04 =
        ion_time_of_flight < step3 and tempvolts_4 or
        (ion_time_of_flight >= step3 and ion_time_of_flight < step4) and _dc1 + tempvolts_4 or
        (ion_time_of_flight >= step4 and ion_time_of_flight < stop_quadru) and
        _dc1 + tempvolts_4 or 0

    adj_elect05 =
        ion_time_of_flight < step4 and tempvolts_4 or
        (ion_time_of_flight >= step4 and ion_time_of_flight < stop_quadru) and
        _dc1 + tempvolts_4 or 0

    adj_elect06 =
        ion_time_of_flight < step1 and tempvolts_4 or
        (ion_time_of_flight >= step1 and ion_time_of_flight < step4) and _dc1 + tempvolts_4 or
        (ion_time_of_flight >= step4 and ion_time_of_flight < stop_quadru) and
        tempvolts_4 or 0

    adj_elect07 =
        ion_time_of_flight < step1 and tempvolts_4 or
        (ion_time_of_flight >= step1 and ion_time_of_flight < step2) and _dc1 + tempvolts_4 or
        (ion_time_of_flight >= step2 and ion_time_of_flight < step3) and _dc2 + tempvolts_4 or
        (ion_time_of_flight >= step3 and ion_time_of_flight < step4) and _dc3 + tempvolts_4 or
```

```
    (ion_time_of_flight >= step4 and ion_time_of_flight < stop_quadru) and
    _dc3 + tempvolts_4 or 0

adj_elect08 =
    ion_time_of_flight < step2 and tempvolts_4 or
    (ion_time_of_flight >= step2 and ion_time_of_flight < step3) and _dc1 + tempvolts_4 or
    (ion_time_of_flight >= step3 and ion_time_of_flight < step4) and _dc2 + tempvolts_4 or
    (ion_time_of_flight >= step4 and ion_time_of_flight < stop_quadru) and
    _dc2 + tempvolts_4 or 0

adj_elect09 =
    ion_time_of_flight < step3 and tempvolts_4 or
    (ion_time_of_flight >= step3 and ion_time_of_flight < step4) and _dc1 + tempvolts_4 or
    (ion_time_of_flight >= step4 and ion_time_of_flight < stop_quadru) and
    _dc1 + tempvolts_4 or 0

adj_elect10 =
    ion_time_of_flight < step4 and tempvolts_4 or
    (ion_time_of_flight >= step4 and ion_time_of_flight < stop_quadru) and
    _dc1 + tempvolts_4 or 0

adj_elect12 =
    ion_time_of_flight < step1 and tempvolts_4 or
    (ion_time_of_flight >= step1 and ion_time_of_flight < step4) and _dc1 + tempvolts_4 or
    (ion_time_of_flight >= step4 and ion_time_of_flight < stop_quadru) and
    tempvolts_4 or 0     phase I

adj_elect22 = ion_time_of_flight < stop_quadru and - tempvolts_4 or 0     power ring II


adj_elect16 =
    ion_time_of_flight < step1 and - tempvolts_4 or
    (ion_time_of_flight >= step1 and ion_time_of_flight < step2) and _dc1 - tempvolts_4 or
    (ion_time_of_flight >= step2 and ion_time_of_flight < step3) and _dc2 - tempvolts_4 or
    (ion_time_of_flight >= step3 and ion_time_of_flight < step4) and _dc3 - tempvolts_4 or
    (ion_time_of_flight >= step4 and ion_time_of_flight < stop_quadru) and
    _dc3 - tempvolts_4 or 0

adj_elect15 =
    ion_time_of_flight < step2 and - tempvolts_4 or
    (ion_time_of_flight >= step2 and ion_time_of_flight < step3) and _dc1 - tempvolts_4 or
    (ion_time_of_flight >= step3 and ion_time_of_flight < step4) and _dc2 - tempvolts_4 or
    (ion_time_of_flight >= step4 and ion_time_of_flight < stop_quadru) and
    _dc2 - tempvolts_4 or 0

adj_elect14 =
    ion_time_of_flight < step3 and -tempvolts_4 or
    (ion_time_of_flight >= step3 and ion_time_of_flight < step4) and _dc1 - tempvolts_4 or
    (ion_time_of_flight >= step4 and ion_time_of_flight < stop_quadru) and
    _dc1 - tempvolts_4 or 0

adj_elect13 =
    ion_time_of_flight < step4 and - tempvolts_4 or
```

```
    (ion_time_of_flight >= step4 and ion_time_of_flight < stop_quadru) and
    _dc1 - tempvolts_4 or 0

adj_elect11 =
    ion_time_of_flight < step1 and - tempvolts_4 or
    (ion_time_of_flight >= step1 and ion_time_of_flight < step4) and _dc1 - tempvolts_4 or
    (ion_time_of_flight >= step4 and ion_time_of_flight < stop_quadru) and
    -tempvolts_4 or 0

adj_elect21 =
    ion_time_of_flight < step1 and -tempvolts_4 or
    (ion_time_of_flight >= step1 and ion_time_of_flight < step2) and _dc1 - tempvolts_4 or
    (ion_time_of_flight >= step2 and ion_time_of_flight < step3) and _dc2 - tempvolts_4 or
    (ion_time_of_flight >= step3 and ion_time_of_flight < step4) and _dc3 - tempvolts_4 or
    (ion_time_of_flight >= step4 and ion_time_of_flight < stop_quadru) and
    _dc3 - tempvolts_4 or 0

adj_elect20 =
    ion_time_of_flight < step2 and - tempvolts_4 or
    (ion_time_of_flight >= step2 and ion_time_of_flight < step3) and _dc1 - tempvolts_4 or
    (ion_time_of_flight >= step3 and ion_time_of_flight < step4) and _dc2 - tempvolts_4 or
    (ion_time_of_flight >= step4 and ion_time_of_flight < stop_quadru) and
    _dc2 - tempvolts_4 or 0

adj_elect19 =
    ion_time_of_flight < step3 and - tempvolts_4 or
    (ion_time_of_flight >= step3 and ion_time_of_flight < step4) and _dc1 - tempvolts_4 or
    (ion_time_of_flight >= step4 and ion_time_of_flight < stop_quadru) and
    _dc1 - tempvolts_4 or 0

adj_elect18 =
    ion_time_of_flight < step4 and - tempvolts_4 or
    (ion_time_of_flight >= step4 and ion_time_of_flight < stop_quadru) and
    _dc1 - tempvolts_4 or 0

adj_elect17 =
    ion_time_of_flight < step1 and - tempvolts_4 or
    (ion_time_of_flight >= step1 and ion_time_of_flight < step4) and _dc1 - tempvolts_4 or
    (ion_time_of_flight >= step4 and ion_time_of_flight < stop_quadru) and
    -tempvolts_4 or 0     phase II
```

6-pole ion trap RF electrodes:

```
adj_elect27 =
    (ion_time_of_flight >= start_hexa and ion_time_of_flight < stop_hexa) and
    tempvolts_6 or 0

adj_elect28 =     (ion_time_of_flight >= start_hexa and ion_time_of_flight < stop_hexa) and
    tempvolts_6 or 0

adj_elect29 =
    (ion_time_of_flight >= start_hexa and ion_time_of_flight < stop_hexa) and
    tempvolts_6 or 0

adj_elect30 =
```

```
    (ion_time_of_flight >= start_hexa and ion_time_of_flight < stop_hexa) and
    tempvolts_6 or 0     phase I

adj_elect31 =
    (ion_time_of_flight >= start_hexa and ion_time_of_flight < stop_hexa) and
    -tempvolts_6 or 0

adj_elect32 =
    (ion_time_of_flight >= start_hexa and ion_time_of_flight < stop_hexa) and
    -tempvolts_6 or 0

adj_elect33 =
    (ion_time_of_flight >= start_hexa and ion_time_of_flight < stop_hexa) and
    -tempvolts_6 or 0

adj_elect34 =
    (ion_time_of_flight >= start_hexa and ion_time_of_flight < stop_hexa) and
    -tempvolts_6 or 0     phase II

DC voltages on endcaps & lenses
adj_elect23 =
    (ion_time_of_flight >= endcap1_2_on and ion_time_of_flight < lens1_on) and
    endcap_dc or (ion_time_of_flight >= lens1_on and ion_time_of_flight < endcap1_off) and
    endcap_push_dc or 0     endcap # 1 at 4-pole

adj_elect24 =
    (ion_time_of_flight >= endcap1_2_on and ion_time_of_flight < lens1_on) and
    endcap_dc or (ion_time_of_flight >= lens1_on and ion_time_of_flight < lens1_off) and
    lens1_dc or 0     endcap # 2 at 4-pole & einzellens # 1

adj_elect25 =
    (ion_time_of_flight >= lens1_on and ion_time_of_flight < lens1_off) and
    lens1_m_dc or 0

adj_elect26 =
    (ion_time_of_flight >= lens1_on and ion_time_of_flight < lens1_off) and
    lens1_dc or (ion_time_of_flight >= lens1_off and ion_time_of_flight < endcap3_off) and
    endcap_dc or 0     einzellens # 2 and endcap # 3 at 6-pole

adj_elect35 =
    (ion_time_of_flight >= endcap4_on and ion_time_of_flight < lens2_on) and
    endcap_dc or (ion_time_of_flight >= lens2_on and ion_time_of_flight < lens2_off) and
    lens2_dc or 0     endcap # 4 at 6-pole & einzellens # 2

adj_elect36 =
    (ion_time_of_flight >= lens2_on and ion_time_of_flight < lens2_off) and
    lens2_m_dc or 0

adj_elect37 =
    (ion_time_of_flight >= lens2_on and ion_time_of_flight < lens2_off) and
    lens2_dc or 0

adj_elect46 =
```

```
    (ion_time_of_flight >= lens3_on and ion_time_of_flight < lens3_off) and
    lens3_dc or 0     einzellens # 3

adj_elect47 =
    (ion_time_of_flight >= lens3_on and ion_time_of_flight < lens3_off) and
    lens3_m_dc or 0

adj_elect48 =
    (ion_time_of_flight >= lens3_on and ion_time_of_flight < lens3_off) and
    lens3_dc or (ion_time_of_flight >= lens3_off and ion_time_of_flight < switch_off) and
    endcap_dc or 0     einzellens # 3 & endcap # 5 at 12-pole


adj_elect63 =
    (ion_time_of_flight >= endcap6_on and ion_time_of_flight < switch_off) and
    endcap_dc or 0     endcap # 6 at 12-pole

DC voltages on q-bend
adj_elect43 =
    (ion_time_of_flight >= bend_on and ion_time_of_flight < bend_off) and
    bend_dc or 0

adj_elect44 =
    (ion_time_of_flight >= bend_on and ion_time_of_flight < bend_off) and
    bend_dc or 0     reflective parts (positive for cations)

adj_elect42 =
    (ion_time_of_flight >= bend_on and ion_time_of_flight < bend_off) and
    -bend_dc or 0

adj_elect45 =
    (ion_time_of_flight >= bend_on and ion_time_of_flight < bend_off) and
    -bend_dc or 0     attractive parts


adj_elect38 =
    (ion_time_of_flight >= bend_on and ion_time_of_flight < bend_off) and
    lens_bend_dc or 0

adj_elect39 =
    (ion_time_of_flight >= bend_on and ion_time_of_flight < bend_off) and
    lens_bend_dc or 0

adj_elect40 =
    (ion_time_of_flight >= bend_on and ion_time_of_flight < bend_off) and
    lens_bend_dc or 0

adj_elect41 =
    (ion_time_of_flight >= bend_on and ion_time_of_flight < bend_off) and
    lens_bend_dc or 0     rings before bender

Electrodes at ground:  bender housing
adj_elect64 = 0
adj_elect65 = 0
adj_elect66 = 0
```

```
adj_elect67 = 0
adj_elect68 = 0
adj_elect69 = 0

12-pole ion trap RF electrodes
adj_elect49 =
    (ion_time_of_flight >= start_dodeca and ion_time_of_flight < switch_off) and
    tempvolts_12 or 0

adj_elect50 =
    (ion_time_of_flight >= start_dodeca and ion_time_of_flight < switch_off) and
    tempvolts_12 or 0

adj_elect51 =
    (ion_time_of_flight >= start_dodeca and ion_time_of_flight < switch_off) and
    tempvolts_12 or 0

adj_elect52 =
    (ion_time_of_flight >= start_dodeca and ion_time_of_flight < switch_off) and
    tempvolts_12 or 0

adj_elect53 =
    (ion_time_of_flight >= start_dodeca and ion_time_of_flight < switch_off) and
    tempvolts_12 or 0

adj_elect54 =
    (ion_time_of_flight >= start_dodeca and ion_time_of_flight < switch_off) and
    tempvolts_12 or 0

adj_elect55 =
    (ion_time_of_flight >= start_dodeca and ion_time_of_flight < switch_off) and
    tempvolts_12 or 0     phase I of RF

adj_elect56 =
    (ion_time_of_flight >= start_dodeca and ion_time_of_flight < switch_off) and
    -tempvolts_12 or 0

adj_elect57 =
    (ion_time_of_flight >= start_dodeca and ion_time_of_flight < switch_off) and
    -tempvolts_12 or 0

adj_elect58 =
    (ion_time_of_flight >= start_dodeca and ion_time_of_flight < switch_off) and
    -tempvolts_12 or 0

adj_elect59 =
    (ion_time_of_flight >= start_dodeca and ion_time_of_flight < switch_off) and
    -tempvolts_12 or 0

adj_elect60 =
    (ion_time_of_flight >= start_dodeca and ion_time_of_flight < switch_off) and
    -tempvolts_12 or 0

adj_elect61 =
    (ion_time_of_flight >= start_dodeca and ion_time_of_flight < switch_off) and
```

```
    -tempvolts_12 or 0

adj_elect62 =
    (ion_time_of_flight >= start_dodeca and ion_time_of_flight < switch_off) and
    -tempvolts_12 or 0     phase II of RF

end

local is_initialized
    Import HS1 collision model.
    SIMION other actions segment.  Called on every time step.

local old_tstep_adjust = segment.tstep_adjust

function segment.tstep_adjust()     Keep time step size <= X usec.
    ion_time_step = min(ion_time_step, 0.1)
    old_tstep_adjust()
end
```

Bibliography

[Adler and Bassi, 2009] Adler, S. L. and Bassi, A. (2009). Physics. Is quantum theory exact? *Science*, 325(5938):275–6.

[Adler et al., 2013] Adler, S. L., Bassi, A., and Donadi, S. (2013). On spontaneous photon emission in collapse models. *J. Phys. A Math. Theor.*, 46(24):245304.

[Amborski and Flierl, 1953] Amborski, L. and Flierl, D. (1953). Physical properties of polyethylene terephthalate films. *Ind. Eng. Chem.*, 45(1):2290–2295.

[Antoine and Dugourd, 2011] Antoine, R. and Dugourd, P. (2011). Visible and ultraviolet spectroscopy of gas phase protein ions. *Phys. Chem. Chem. Phys.*, 13(37):16494–509.

[Arimondo et al., 1993] Arimondo, E., Phillips, W., and Strumia, F. (1993). *Laser manipulation of atoms and ions*.

[Arndt and Hornberger, 2014] Arndt, M. and Hornberger, K. (2014). Testing the limits of quantum mechanical superpositions. *Nat. Phys.*, 10(April):271–277.

[Arndt et al., 1999] Arndt, M., Nairz, O., Vos-Andreae, J., Keller, C., van der Zouw, G., and Zeilinger, A. (1999). Wave-particle duality of C(60) molecules. *Nature*, 401(6754):680–2.

[Asenbaum et al., 2013] Asenbaum, P., Kuhn, S., Nimmrichter, S., Sezer, U., and Arndt, M. (2013). Cavity cooling of free silicon nanoparticles in high vacuum. *Nat. Commun.*

[Asvany et al., 2004] Asvany, O., Schlemmer, S., and Gerlich, D. (2004). Deuteration of CHn+ (n= 3-5) in Collisions with HD Measured in a Low-Temperature Ion Trap. *Astrophys. J.*, 3:685–692.

[Bahns et al., 1996] Bahns, J. T., Stwalley, W. C., and Gould, P. L. (1996). Laser cooling of molecules: A sequential scheme for rotation, translation, and vibration. *J. Chem. Phys.*, 104(24):9689.

[Barker and Shneider, 2010] Barker, P. F. and Shneider, M. N. (2010). Cavity cooling of an optically trapped nanoparticle. *Phys. Rev. A*, 81(2):023826.

[Bassi and Ghirardi, 2003] Bassi, A. and Ghirardi, G. (2003). Dynamical reduction models. *Phys. Rep.*, 379(5-6):257–426.

[Bassi et al., 2013] Bassi, A., Lochan, K., Satin, S., Singh, T., and Ulbricht, H. (2013). Models of wave-function collapse, underlying theories, and experimental tests. *Rev. Mod. Phys.*

[Berry et al., 2001] Berry, M., Marzoli, I., and Schleich, W. (2001). Quantum carpets, carpets of light. *Phys. World*, (June 2001).

[Bertelsen et al., 2006] Bertelsen, A., Jø rgensen, S., and Drewsen, M. (2006). The rotational temperature of polar molecular ions in Coulomb crystals. *J. Phys. B At. Mol. Opt. Phys.*, 39(5):L83–L89.

[Bian et al., 2010] Bian, Q., Forbes, M. W., Talbot, F. O., and Jockusch, R. a. (2010). Gas-phase fluorescence excitation and emission spectroscopy of mass-selected trapped molecular ions. *Phys. Chem. Chem. Phys.*, 12(11):2590–8.

[Bohr, 1928] Bohr, N. (1928). Das Quantenpostulat und die neuere Entwicklung der Atomistik. *Naturwissenschaften*, 13.

[Bothner and Siuzdak, 2004] Bothner, B. and Siuzdak, G. (2004). Electrospray ionization of a whole virus: analyzing mass, structure, and viability. *Chembiochem Eur. J. Chem. Biol.*, 5(3):258–60.

[Bowe et al., 1999] Bowe, P., Hornekæ r, L., Brodersen, C., Drewsen, M., Hangst, J., and Schiffer, J. (1999). Sympathetic Crystallization of Trapped Ions. *Phys. Rev. Lett.*, 82(10):2071–2074.

[Brezger et al., 2002] Brezger, B., Hackermüller, L., Uttenthaler, S., Petschinka, J., Arndt, M., and Zeilinger, A. (2002). Matter-Wave Interferometer for Large Molecules. *Phys. Rev. Lett.*, 88(10):100404.

[Broglie, 1923] Broglie, L. D. (1923). Waves and quanta. *Nature*.

[Brümmer et al., 2003] Brümmer, M., Kaposta, C., Santambrogio, G., and Asmis, K. R. (2003). Formation and photodepletion of cluster ion–messenger atom complexes in

a cold ion trap: Infrared spectroscopy of VO+, VO2+, and VO3+. *J. Chem. Phys.*, 119(24):12700.

[Cai et al., 2002] Cai, Y., Peng, W. P., Kuo, S. J., Sabu, S., Han, C. C., and Chang, H. C. (2002). Optical detection and charge-state analysis of MALDI-generated particles with molecular masses larger than 5 MDa. *Anal. Chem.*, 74(17):4434–40.

[Campbell et al., 1998] Campbell, J. M., Collings, B. a., and Douglas, D. J. (1998). A new linear ion trap time-of-flight system with tandem mass spectrometry capabilities. *Rapid Commun. Mass Spectrom.*, 12(20):1463–1474.

[Carnal and Mlynek, 1991] Carnal, O. and Mlynek, J. (1991). Young's double-slit experiment with atoms: A simple atom interferometer. *Phys. Rev. Lett.*, 66(21).

[Case et al., 2009] Case, W. B., Tomandl, M., Deachapunya, S., and Arndt, M. (2009). Realization of optical carpets in the Talbot and Talbot-Lau configurations. *Opt. Express*, 17(23):20966–74.

[Champenois, 2009] Champenois, C. (2009). About the dynamics and thermodynamics of trapped ions. *J. Phys. B At. Mol. Opt. Phys.*, 42(15):154002.

[Chiaverini et al., 2005] Chiaverini, J., Blakestad, R., and Britton, J. (2005). Surface-electrode architecture for ion-trap quantum information processing. *arXiv Prepr. quant-ph/ ...*, 5(6):419–439.

[Church and Dehmelt, 1969] Church, D. and Dehmelt, H. (1969). Radiative cooling of an electrodynamically contained proton gas. *J. Appl. Phys.*, 40(9):3421.

[Clauser, 1997] Clauser, J. F. (1997). Experimental Metaphysics. *Quantum Mech. Stud. Abner Shimony*, pages 1–11.

[Dahl, 2000] Dahl, D. (2000). SIMION for the personal computer in reflection. *Int. J. Mass Spectrom.*, 200(1-3):3–25.

[Dalibard and Cohen-Tannoudji, 1989] Dalibard, J. and Cohen-Tannoudji, C. (1989). Laser cooling below the Doppler limit by polarization gradients: simple theoretical models. *J. Opt. Soc. Am. B*, 6(11):2023.

[Daly, 1960] Daly, N. R. (1960). Scintillation Type Mass Spectrometer Ion Detector. *Rev. Sci. Instrum.*, 31(3):264.

[Davisson and Germer, 1927] Davisson, C. and Germer, L. (1927). The scattering of electrons by a single crystal of nickel. *Nature*.

[Dawson, 1970] Dawson, P. H. (1970). Quadrupole Mass Filter: Circular Rods and Peak Shapes. *J. Vac. Sci. Technol.*, 7(3):440.

[DeCarvalho et al., 1999] DeCarvalho, R., Doyle, J., Friedrich, B., Guillet, T., Kim, J., Patterson, D., and Weinstein, J. (1999). Buffer-gas loaded magnetic traps for atoms and molecules: A primer. *Eur. Phys. J. D*, 309:289–309.

[Dehmelt, 1967] Dehmelt, H. (1967). Radiofrequency spectroscopy of stored ions I: Storage. *Adv. At. Mol. Phys*.

[Demelbauer et al., 2004] Demelbauer, U. M., Zehl, M., Plematl, A., Allmaier, G., and Rizzi, A. (2004). Determination of glycopeptide structures by multistage mass spectrometry with low-energy collision-induced dissociation: comparison of electrospray ionization quadrupole ion trap and matrix-assisted laser desorption/ionization quadrupole ion trap reflectr. *Rapid Commun. Mass Spectrom.*, 18(14):1575–82.

[Demtröder, 2008] Demtröder, W. (2008). *Experimentalphysik 1: Mechanik und Wärme*. Springer Verlag Berlin, 5. auflage edition.

[Denison, 1971] Denison, D. R. (1971). Operating Parameters of a Quadrupole in a Grounded Cylindrical Housing. *J. Vac. Sci. Technol.*, 8(1):266.

[der Vegt and Govaert, 2003] der Vegt, A. V. and Govaert, L. (2003). *Polymeren: van keten tot kunststof*.

[Diedrich and Bergquist, 1989] Diedrich, F. and Bergquist, J. (1989). Laser cooling to the zero-point energy of motion. *Phys. Rev. Lett.*

[Domen, 1991] Domen, S. (1991). Emissivity of aluminized mylar. *Int. J. Radiat. Appl. ...*, 37(2):199–201.

[Douglas and French, 1992] Douglas, D. and French, J. (1992). Collisional focusing effects in radio frequency quadrupoles. *J. Am. Soc. Mass Spectrom.*, 3:398–408.

[Douglas et al., 2005] Douglas, D. J., Frank, A. J., and Mao, D. (2005). Linear ion traps in mass spectrometry. *Mass Spectrom. Rev.*, 24(1):1–29.

[Doyle et al., 1995] Doyle, J., Friedrich, B., Kim, J., and Patterson, D. (1995). Buffer-gas loading of atoms and molecules into a magnetic trap. *Phys. Rev. A*, 52(4).

[Drewsen et al., 2003] Drewsen, M., Jensen, I., Lindballe, J., Nissen, N., Martinussen, R., Mortensen, a., Staanum, P., and Voigt, D. (2003). Ion Coulomb crystals: a tool for studying ion processes. *Int. J. Mass Spectrom.*, 229(1-2):83–91.

[Dubin and O'Neil, 1999] Dubin, D. H. E. and O'Neil, T. M. (1999). Trapped nonneutral plasmas, liquids, and crystals (the thermal equilibrium states). *Rev. Mod. Phys.*, 71(1):87–172.

[Egorov et al., 2002] Egorov, D., Lahaye, T., Schöllkopf, W., Friedrich, B., and Doyle, J. (2002). Buffer-gas cooling of atomic and molecular beams. *Phys. Rev. A*, 66(4):043401.

[Eibenberger et al., 2013] Eibenberger, S., Gerlich, S., Arndt, M., Mayor, M., and Tüxen, J. (2013). Matter-wave interference of particles selected from a molecular library with masses exceeding 10,000 amu. *Phys. Chem. Chem. Phys.*, 15(35):14696–700.

[Everett III, 1957] Everett III, H. (1957). " Relative state" formulation of quantum mechanics. *Rev. Mod. Phys.*

[Farley, 1985] Farley, J. W. (1985). Simple electrostatic quadrupole ion beam deflector. *Rev. Sci. Instrum.*, 56(9):1834.

[Fenn et al., 1989] Fenn, J., Mann, M., and Meng, C. (1989). Electrospray ionization for mass spectrometry of large biomolecules. *Science (80-.).*

[Franck et al., 1961] Franck, J., Manchester, F., and Martin, D. (1961). The specific heat of pure copper and of some dilute copper+ iron alloys showing a minimum in the electrical resistance at low temperatures. *Proc. R. Soc.*

[Freimund et al., 2001] Freimund, D. L., Aflatooni, K., and Batelaan, H. (2001). Observation of the Kapitza-Dirac effect. *Nature*, 413(6852):142–3.

[Fricke et al., 1980] Fricke, J., Müller, A., and Salzborn, E. (1980). Single particle counting of heavy ions with a channeltron detector. *Nucl. Instruments Methods*, 175:379–384.

[Friedman, 1982] Friedman, M. (1982). Fundamentals of ion motion in electric radio-frequency multipole fields. *J. Phys. E.*, 53.

[Friedrich et al., 2004] Friedrich, J., Fu, J., Hendrickson, C. L., Marshall, A. G., and Wang, Y.-S. (2004). Time resolved laser-induced fluorescence of electrosprayed ions confined in a linear quadrupole trap. *Rev. Sci. Instrum.*, 75(11):4511.

[Gerlich, 1986] Gerlich, D. (1986). Low energy ion reactions measured with guided beams. *Electron. At. collisions*.

[Gerlich, 1992] Gerlich, D. (1992). Inhomogeneous rf fields: a versatile tool for the study of processes with slow ions. In *Adv. Chem. Phys. Ser.*, volume LXXXII.

[Gerlich, 1995] Gerlich, D. (1995). Ion-Neutral Collisions in a 22-Pole Trap at Very Low Energies. *Phys. Scr.*, T56:256–263.

[Gerlich, 2008a] Gerlich, D. (2008a). The production and study of ultra-cold molecular ions. In *Low Temp. cold Mol.*, pages 295–344.

[Gerlich, 2008b] Gerlich, D. (2008b). The study of cold collisions using ion guides and traps. *Low Temp. cold Mol.*

[Gerlich and Borodi, 2009] Gerlich, D. and Borodi, G. (2009). Buffer gas cooling of polyatomic ions in rf multi-electrode traps. *Faraday Discuss.*, 142:57.

[Gerlich, 2011] Gerlich, S. (2011). *Interferometry and metrology with macromolecules*. PhD thesis.

[Gerlich et al., 2007] Gerlich, S., Hackermüller, L., Hornberger, K., Stibor, A., Ulbricht, H., Gring, M., Goldfarb, F., Savas, T., Müri, M., Mayor, M., and Arndt, M. (2007). A Kapitza-Dirac-Talbot-Lau interferometer for highly polarizable molecules.

[Ghirardi et al., 1986] Ghirardi, G., Rimini, a., and Weber, T. (1986). Unified dynamics for microscopic and macroscopic systems. *Phys. Rev. D. Part. Fields*, 34(2):470–491.

[Ghosh, 1995] Ghosh, P. K. (1995). *Ion Traps*. Clarendon Press. Oxford.

[Giulini and Groß ardt, 2011] Giulini, D. and Groß ardt, A. (2011). Gravitationally induced inhibitions of dispersion according to the Schrödinger–Newton equation. *Class. Quantum Gravity*, 28(19):195026.

[Glassford and Liu, 1980] Glassford, A. P. M. and Liu, C.-K. (1980). Outgassing rate of multilayer insulation materials at ambient temperature. *J. Vac. Sci. Technol.*, 17(3):696.

[Glassford et al., 1984] Glassford, A. P. M., Osiecki, R. A., and Liu, C.-K. (1984). Effect of temperature and preconditioning on the outgassing rate of double aluminized mylar and dacron net. *J. Vac. Sci. Technol. A Vacuum, Surfaces, Film.*, 2(3):1370.

[Golovlev et al., 1997] Golovlev, V., Allman, S., Garrett, W., Taranenko, N., and Chen, C. (1997). Laser-induced acoustic desorption. *Int. J. Mass Spectrom.*, 70(I 997):69–78.

[Gould et al., 1986] Gould, P., Ruff, G., and Pritchard, D. (1986). Diffraction of atoms by light: The near-resonant Kapitza-Dirac effect. *Phys. Rev. Lett.*, 56(8).

[Gulde et al., 2003] Gulde, S., Riebe, M., Lancaster, G., and Becher, C. (2003). Implementation of the Deutsch–Jozsa algorithm on an ion-trap quantum computer. *Nature*, 421(January):48–50.

[Haberland et al., 1991] Haberland, H., Karrais, M., and Mall, M. (1991). A new type of cluster and cluster ion source. *Zeitschrift für Phys. D Atoms, Mol. Clust.*, 415:413–415.

[Hackermüller et al., 2004] Hackermüller, L., Hornberger, K., Brezger, B., Zeilinger, A., and Arndt, M. (2004). Decoherence of matter waves by thermal emission of radiation. *Nature*, 427(6976):711–4.

[Hägg and Szabo, 1986] Hägg, C. and Szabo, I. (1986). New ion-optical devices utilizing oscillatory electric fields. II. Stability of ion motion in a two-dimensional hexapole field. *Int. J. Mass Spectrom. Ion Process.*, 73:237–275.

[Haslinger, 2013] Haslinger, P. (2013). *A universal matter-wave interferometer with optical gratings*. PhD thesis.

[Haslinger et al., 2013] Haslinger, P., Dörre, N., Geyer, P., Rodewald, J., Nimmrichter, S., and Arndt, M. (2013). A universal matter-wave interferometer with optical ionization gratings in the time domain. *Nat. Phys.*, 9(3):144–148.

[Herfurth, 2003] Herfurth, F. (2003). Segmented linear RFQ traps for nuclear physics. *Nucl. Instruments Methods Phys. Res. Sect. B Beam Interact. with Mater. Atoms*, 204:587–591.

[Herfurth et al., 2001] Herfurth, F., Dilling, J., Kellerbauer, A., Bollen, G., Henry, S., Kluge, H., Lamour, E., Lunney, D., Moore, R. B., Scheidenberger, C., Schwarz, S., Sikler, G., and Szerypo, J. (2001). A linear radiofrequency ion trap for accumulation, bunching,

and emittance improvement of radioactive ion beams. *Nucl. Instruments Methods Phys. Res. Sect. A Accel. Spectrometers, Detect. Assoc. Equip.*, 469(2):254–275.

[Hogan et al., 2005] Hogan, J. M., Pitteri, S. J., Chrisman, P. A., and Mcluckey, S. A. (2005). Complementary Structural Information from a Tryptic N -Linked Glycopeptide via Electron Transfer Ion-Ion Reactions and Collision-Induced Dissociation. *J. proteome Res. Tech. notes*, (765):628–632.

[Home et al., 2009] Home, J., Hanneke, D., Jost, J., and Amini, J. (2009). Complete methods set for scalable ion trap quantum information processing. *Science (80-.).*, (September).

[Hontañón and Kruis, 2008] Hontañón, E. and Kruis, F. E. (2008). Single Charging of Nanoparticles by UV Photoionization at High Flow Rates. *Aerosol Sci. Technol.*, 42(4):310–323.

[Horak et al., 1997] Horak, P., Hechenblaikner, G., Gheri, K., Stecher, H., and Ritsch, H. (1997). Cavity-Induced Atom Cooling in the Strong Coupling Regime. *Phys. Rev. Lett.*, 79(25):4974–4977.

[Hornberger et al., 2004] Hornberger, K., Sipe, J., and Arndt, M. (2004). Theory of decoherence in a matter wave Talbot-Lau interferometer. *Phys. Rev. A*, 70(5):053608.

[Hornberger et al., 2003] Hornberger, K., Uttenthaler, S., Brezger, B., Hackermüller, L., Arndt, M., and Zeilinger, A. (2003). Collisional Decoherence Observed in Matter Wave Interferometry. *Phys. Rev. Lett.*, 90(16):160401.

[Hudson, 2009] Hudson, E. (2009). Method for producing ultracold molecular ions. *Phys. Rev. A*, 79(3):032716.

[Ishitani et al., 1978] Ishitani, T., Sakudo, N., Tamura, H., and Kanomata, I. (1978). Sputtered neutral mass spectrometry using post-ionization in a microwave plasma. *Phys. Lett. A*, 67(5):375–378.

[Itano et al., 1995] Itano, W. M., Bergquist, J. C., Bollinger, J. J., and Wineland, D. J. (1995). Cooling methods in ion traps. *Phys. Scr.*, T59:106–120.

[Jahns and Lohmann, 1979] Jahns, J. and Lohmann, A. (1979). The Lau effect (a diffraction experiment with incoherent illumination). *Opt. Commun.*, 28(3):3–7.

[Jousten, 2006] Jousten, K. H. (2006). *Wutz Handbuch Vakuumtechnik: Theorie und Praxis*. Springer Verlag Berlin-Heidelberg.

[Juffmann et al., 2010] Juffmann, T., Nimmrichter, S., Arndt, M., Gleiter, H., and Hornberger, K. (2010). New Prospects for de Broglie Interferometry. *Found. Phys.*, 42(1):98–110.

[Kapitza and Dirac, 1933] Kapitza, P. L. and Dirac, P. a. M. (1933). The reflection of electrons from standing light waves. *Math. Proc. Cambridge Philos. Soc.*, 29(02):297.

[Karas and Hillenkamp, 1988] Karas, M. and Hillenkamp, F. (1988). Laser desorption ionization of proteins with molecular masses exceeding 10000 daltons. *Anal. Chem.*, 2301(29):2299–2301.

[Karas and Krüger, 2003] Karas, M. and Krüger, R. (2003). Ion formation in MALDI: the cluster ionization mechanism. *Chem. Rev.*, 103(2):427–40.

[Kasevich and Chu, 1992] Kasevich, M. and Chu, S. (1992). Laser cooling below a photon recoil with three-level atoms. *Phys. Rev. Lett.*, 69(12).

[Keith et al., 1988] Keith, D., Schattenburg, M., Smith, H., and Pritchard, D. (1988). Diffraction of atoms by a transmission grating. *Phys. Rev. Lett.*, 61(14).

[Kielpinski et al., 2002] Kielpinski, D., Monroe, C., and Wineland, D. (2002). Architecture for a large-scale ion-trap quantum computer. *Nature*, 417(June):709–711.

[Kiesel et al., 2013] Kiesel, N., Blaser, F., Delić, U., Grass, D., Kaltenbaek, R., and Aspelmeyer, M. (2013). Cavity cooling of an optically levitated submicron particle. *Proc. Natl. Acad. Sci.*

[Kinsey, 1977] Kinsey, J. L. (1977). Laser-Induced Fluorescence. *Annu. Rev. Phys. Chem.*, 28(1):349–372.

[Kuppens et al., 1998] Kuppens, S., Rauner, M., Schiffer, M., Sengstock, K., Ertmer, W., van Dorsselaer, F., and Nienhuis, G. (1998). Polarization-gradient cooling in a strong doughnut-mode dipole potential. *Phys. Rev. A*, 58(4):3068–3079.

[Lamine et al., 2006] Lamine, B., Hervé, R., Lambrecht, A., and Reynaud, S. (2006). Ultimate Decoherence Border for Matter-Wave Interferometry. *Phys. Rev. Lett.*, 96(5):050405.

[Larsen et al., 2001] Larsen, A., Uran, S., Jacobsen, P. B., and Skotland, T. (2001). Collision-induced dissociation of glycero phospholipids using electrospray ion-trap mass spectrometry. *Rapid Commun. Mass Spectrom.*, 15(24):2393–8.

[Lau, 1948] Lau, E. (1948). Beugungserscheinungen an Doppelrastern. *Ann. Phys.*, 437(7-8):417–423.

[Lee et al., 1996] Lee, H., Adams, C., Kasevich, M., and Chu, S. (1996). Raman Cooling of Atoms in an Optical Dipole Trap. *Phys. Rev. Lett.*, 76(15):2658–2661.

[Liu et al., 1995] Liu, P., Ziemann, P. J., Kittelson, D. B., and McMurry, P. H. (1995). Generating Particle Beams of Controlled Dimensions and Divergence: I. Theory of Particle Motion in Aerodynamic Lenses and Nozzle Expansions. *Aerosol Sci. Technol.*, 22(3):293–313.

[Liu et al., 2014] Liu, R., Li, Q., and Smith, L. M. (2014). Detection of Large Ions in Time-of-Flight Mass Spectrometry: Effects of Ion Mass and Acceleration Voltage on Microchannel Plate Detector Response. *J. Am. Soc. Mass Spectrom.*

[Majima et al., 2012] Majima, T., Santambrogio, G., Bartels, C., Terasaki, A., Kondow, T., Meinen, J., and Leisner, T. (2012). Spatial distribution of ions in a linear octopole radio-frequency ion trap in the space-charge limit. *Phys. Rev. A*, 85(5):053414.

[Major and Dehmelt, 1968] Major, F. and Dehmelt, H. (1968). Exchange-collision technique for the rf spectroscopy of stored ions. *Phys. Rev.*, 170(1).

[Makarov et al., 2006] Makarov, A., Denisov, E., Kholomeev, A., Balschun, W., Lange, O., Strupat, K., and Horning, S. (2006). Performance evaluation of a hybrid linear ion trap/orbitrap mass spectrometer. *Anal. Chem.*, 78(7):2113–20.

[Marquardt et al., 2002] Marquardt, E., Le, J., and Radebaugh, R. (2002). Cryogenic material properties database. In *11th Cryocoolers Conf.*

[Marshall et al., 2003] Marshall, W., Simon, C., Penrose, R., and Bouwmeester, D. (2003). Towards Quantum Superpositions of a Mirror. *Phys. Rev. Lett.*, 91(13):130401.

[Matt et al., 1997] Matt, S., Echt, O., Rauth, T., Dünser, B., Lezius, M., Stamatovic, A., Scheier, P., and Märk, T. D. (1997). Electron impact ionization and dissociation of neutral and charged fullerenes. *Zeitschrift für Phys. D Atoms, Mol. Clust.*, 40(1-4):389–394.

[Meetani and Shin, 2007] Meetani, M. and Shin, Y. (2007). Desorption electrospray ionization mass spectrometry of intact bacteria. *J. Mass Spectrom.*, (July):1186–1193.

[Mikosch et al., 2007] Mikosch, J., Frühling, U., Trippel, S., Schwalm, D., Weidemüller, M., and Wester, R. (2007). Evaporation of Buffer-Gas-Thermalized Anions out of a Multipole rf Ion Trap. *Phys. Rev. Lett.*, 98(22):223001.

[Miller and Denton, 1986] Miller, P. E. and Denton, M. B. (1986). The quadrupole mass filter: Basic operating concepts. *J. Chem. Educ.*, 63(7):617.

[Mø lhave and Drewsen, 2000] Mø lhave, K. and Drewsen, M. (2000). Formation of translationally cold MgH+ and MgD+ molecules in an ion trap. *Phys. Rev. A*, 62(March):1–4.

[Monroe et al., 1995] Monroe, C., Meekhof, D., and King, B. (1995). Demonstration of a fundamental quantum logic gate. *Phys. Rev. Lett.*, 75(25).

[Moore, 2002] Moore, R. B. (2002). Buffer gas cooling of ion beams. Technical Report January.

[Morigi et al., 2000] Morigi, G., Eschner, J., and Keitel, C. H. (2000). Ground State Laser Cooling Using Electromagnetically Induced Transparency. *Phys. Rev. Lett.*, 85(21):4458–4461.

[Nairz et al., 2001] Nairz, O., Brezger, B., Arndt, M., and Zeilinger, A. (2001). Diffraction of Complex Molecules by Structures Made of Light. *Phys. Rev. Lett.*, 87(16):160401.

[Nimmrichter, 2013] Nimmrichter, S. (2013). *Macroscopic Matter Wave Interferometry*. PhD thesis.

[Nimmrichter et al., 2011a] Nimmrichter, S., Haslinger, P., Hornberger, K., and Arndt, M. (2011a). Concept of an ionizing time-domain matter-wave interferometer. *New J. Phys.*, 13(7):075002.

[Nimmrichter et al., 2011b] Nimmrichter, S., Hornberger, K., Haslinger, P., and Arndt, M. (2011b). Testing spontaneous localization theories with matter-wave interferometry. *Phys. Rev. A*, 83.

[O'Hanlon, 2003] O'Hanlon, J. F. (2003). *A User's Guide to Vacuum Technology*. Wiley-Interscience, 3rd editio edition.

[Okada and Wada, 2001] Okada, K. and Wada, M. (2001). Cryogenic ion trap for minimization of trapped ion loss. *Jpn. J. Appl. Phys.*, 4221:4221–4223.

[Ostendorf et al., 2006] Ostendorf, A., Zhang, C., Wilson, M., Offenberg, D., Roth, B., and Schiller, S. (2006). Sympathetic Cooling of Complex Molecular Ions to Millikelvin Temperatures. *Phys. Rev. Lett.*, 97(24):243005.

[Paul, 1990] Paul, W. (1990). Electromagnetic traps for charged and neutral particles. *Angew. Chem. Int. Ed. Engl.*, 29:739–748.

[Paul and Steinwedel, 1953] Paul, W. and Steinwedel, H. (1953). Verfahren zur Trennung bzw. zum getrennten Nachweis von Ionen verschiedener spezifischer Ladung.

[Pearle, 1989] Pearle, P. (1989). Combining stochastic dynamical state-vector reduction with spontaneous localization. *Phys. Rev. A*, 39(5).

[Peng et al., 2004a] Peng, W., Yang, Y., and Kang, M. (2004a). Measuring masses of single bacterial whole cells with a quadrupole ion trap. *J. Am. Chem. Soc.*, 957(126):11766–11767.

[Peng et al., 2004b] Peng, W.-P., Cai, Y., and Chang, H.-C. (2004b). Optical detection methods for mass spectrometry of macroions. *Mass Spectrom. Rev.*, 23(6):443–65.

[Peng et al., 2003] Peng, W.-P., Cai, Y., Lee, Y., and Chang, H.-C. (2003). Laser-induced fluorescence/ion trap as a detector for mass spectrometric analysis of nanoparticles. *Int. J. Mass Spectrom.*, 229(1-2):67–76.

[Peng et al., 2006] Peng, W.-P., Yang, Y.-C., Kang, M.-W., Tzeng, Y.-K., Nie, Z., Chang, H.-C., Chang, W., and Chen, C.-H. (2006). Laser-Induced Acoustic Desorption Mass Spectrometry of Single Bioparticles. *Angew. Chemie*, 118(9):1451–1454.

[Penrose, 1996] Penrose, R. (1996). On gravity's role in quantum state reduction. *Gen. Relativ. Gravit.*, (5):24–29.

[Pfeiffer Vacuum, 2015] Pfeiffer Vacuum (2015). HiPace 80(R) turbomolecular pump, specifications.

[Pietschmann, 1995] Pietschmann, H. (1995). *Phänomenologie der Naturwissenschaft: Wissenschaftstheoretische und philosophische Probleme der Physik*. Springer.

[Pobell, 1996] Pobell, F. (1996). *Matter and methods at low temperatures*. Second edition.

[Poitzsch et al., 1996] Poitzsch, M. E., Bergquist, J. C., Itano, W. M., and Wineland, D. J. (1996). Cryogenic linear ion trap for accurate spectroscopy. *Rev. Sci. Instrum.*, 67(1):129.

[Pratontep et al., 2005] Pratontep, S., Carroll, S. J., Xirouchaki, C., Streun, M., and Palmer, R. E. (2005). Size-selected cluster beam source based on radio frequency magnetron plasma sputtering and gas condensation. *Rev. Sci. Instrum.*, 76(4):045103.

[Prestage et al., 1989] Prestage, J. D., Dick, G. J., and Maleki, L. (1989). New ion trap for frequency standard applications. *J. Appl. Phys.*, 66(3):1013.

[Rauch et al., 1974] Rauch, H., Treimer, W., and Bonse, U. (1974). Test of a single crystal neutron interferometer. *Phys. Lett. A*, 47(5):369–371.

[Rosa, 2004] Rosa, M. D. (2004). Laser-cooling molecules. *Eur. Phys. J. D*, 31(2):395–402.

[Ryjkov et al., 2006] Ryjkov, V., Zhao, X., and Schuessler, H. (2006). Sympathetic cooling of fullerene ions by laser-cooled Mg^{+} ions in a linear rf trap. *Phys. Rev. A*, 74(2):023401.

[Scalf et al., 1999] Scalf, M., Westphall, M. S., Krause, J., Kaufman, S. L., and Smith, L. M. (1999). Controlling Charge States of Large Ions. *Science (80-.).*, 283(5399):194–197.

[Schwarz, 2012] Schwarz, M. (2012). *Lasermanipulation von rotationsgekühlten Molekülionen in einer neuen kryogenen Paul-Falle*. PhD thesis.

[Schwarz et al., 2012] Schwarz, M., Versolato, O., Windberger, A., Brunner, F. R., Ballance, T., Eberle, S. N., Ullrich, J., Schmidt, P. O., Hansen, a. K., Gingell, A. D., Drewsen, M., and López-Urrutia, J. R. C. (2012). Cryogenic linear Paul trap for cold highly charged ion experiments. *Rev. Sci. Instrum.*, 83(8):083115.

[Shackelford and Alexander, 2010] Shackelford, J. and Alexander, W. (2010). *CRC materials science and engineering handbook*. Third edition.

[Shuman et al., 2010] Shuman, E. S., Barry, J. F., and Demille, D. (2010). Laser cooling of a diatomic molecule. *Nature*, 467(7317):820–3.

[Smith et al., 2005] Smith, W. W., Makarov, O. P., and Lin, J. (2005). Cold ion–neutral collisions in a hybrid trap. *J. Mod. Opt.*, 52(16):2253–2260.

[Snow and Bierbaum, 2008] Snow, T. P. and Bierbaum, V. M. (2008). Ion chemistry in the interstellar medium. *Annu. Rev. Anal. Chem. (Palo Alto. Calif).*, 1:229–59.

[Steane, 1997] Steane, A. (1997). The ion trap quantum information processor. *Appl. Phys. B Lasers Opt.*, 642:623–642.

[Stenholm, 1986] Stenholm, S. (1986). The semiclassical theory of laser cooling. *Rev. Mod. Phys.*, (1950).

[Stibor et al., 2004] Stibor, A., Hornberger, K., Hackermüller, L., Zeilinger, A., and Arndt, M. (2004). Talbot-Lau interferometry with fullerenes: Sensitivity to inertial forces and vibrational dephasing. *arXiv Prepr.*

[Sulkes et al., 1980] Sulkes, M., Tusa, J., and Rice, S. a. (1980). Collision induced relaxation of an electronically excited molecule: Evidence for low energy resonance enhanced vibrational deactivation. *J. Chem. Phys.*, 72(10):5733.

[Swanson and Leith, 1985] Swanson, G. and Leith, E. (1985). Analysis of the Lau effect and generalized grating imaging. *JOSA A*, 2(6):789–793.

[Talbot, 1836] Talbot, H. F. (1836). LXXVI. Facts relating to optical science. No. IV. *Philos. Mag. Ser. 3*, 9(56):401–407.

[Tanaka et al., 1988] Tanaka, K., Waki, H., Ido, Y., Akita, S., Yoshida, Y., and Yoshida, T. (1988). Protein and polymer analyses up to m/z 100 000 by laser ionization time-of-flight mass spectrometry. *Rapid Commun. mass Spectrom. RCM*, 2(8):151–153.

[Teloy and Gerlich, 1974] Teloy, E. and Gerlich, D. (1974). Integral cross sections for ion-molecule reactions. *Chem. Phys.*

[Thomson, 1927] Thomson, G. (1927). The diffraction of cathode rays by thin films of platinum. *Nature*.

[Tolmachev et al., 2000] Tolmachev, A. V., Udseth, H. R., and Smith, R. D. (2000). Charge capacity limitations of radio frequency ion guides in their use for improved ion accumulation and trapping in mass spectrometry. *Anal. Chem.*, 72(5):970–8.

[Uetrecht et al., 2010] Uetrecht, C., Rose, R. J., van Duijn, E., Lorenzen, K., and Heck, A. J. R. (2010). Ion mobility mass spectrometry of proteins and protein assemblies. *Chem. Soc. Rev.*, 39(5):1633–55.

[Van Sciver, 2012] Van Sciver, S. W. (2012). Low-Temperature Materials Properties. In *Helium Cryog.*, chapter 2. Springer New York, New York, NY.

[Wang et al., 2005] Wang, X.-B., Woo, H.-K., and Wang, L.-S. (2005). Vibrational cooling in a cold ion trap: vibrationally resolved photoelectron spectroscopy of cold C60(-) anions. *J. Chem. Phys.*, 123(5):051106.

[White and Malmberg, 1982] White, W. and Malmberg, J. (1982). Feedback damping of the l=1 diocotron wave. *Bull. Am. Phys. Soc.*

[Willitsch et al., 2008a] Willitsch, S., Bell, M. T., Gingell, A. D., Procter, S., and Softley, T. P. (2008a). Cold Reactive Collisions between Laser-Cooled Ions and Velocity-Selected Neutral Molecules. *Phys. Rev. Lett.*, 100(4):043203.

[Willitsch et al., 2008b] Willitsch, S., Bell, M. T., Gingell, A. D., and Softley, T. P. (2008b). Chemical applications of laser- and sympathetically-cooled ions in ion traps. *Phys. Chem. Chem. Phys.*, 10(48):7200–10.

[Wineland et al., 1987] Wineland, D., Itano, W., Bergquist, J., and Hulet, R. (1987). Laser-cooling limits and single-ion spectroscopy. *Phys. Rev. A*, 36(5):2220–2232.

[Wuerker et al., 1959] Wuerker, R. F., Shelton, H., and Langmuir, R. V. (1959). Electrodynamic Containment of Charged Particles. *J. Appl. Phys.*, 30(3):342.

[Yinon et al., 1997] Yinon, J., McClellan, J., and Yost, R. (1997). Electrospray ionization tandem mass spectrometry collision-induced dissociation study of explosives in an ion trap mass spectrometer. *Rapid Commun. Mass Spectrom.*, 11:1961–1970.

[Zeh, 1970] Zeh, H. D. (1970). On the interpretation of measurement in quantum theory. *Found. Phys.*, 1(1):69–76.

[Zhang et al., 2002] Zhang, X., Smith, K. a., Worsnop, D. R., Jimenez, J., Jayne, J. T., and Kolb, C. E. (2002). A Numerical Characterization of Particle Beam Collimation by an Aerodynamic Lens-Nozzle System: Part I. An Individual Lens or Nozzle. *Aerosol Sci. Technol.*, 36(5):617–631.

[Zurek, 1982] Zurek, W. (1982). Environment-induced superselection rules. *Phys. Rev. D*, 26(8).

[Zurek, 2003] Zurek, W. (2003). Decoherence and the transition from quantum to classical–REVISITED. *arXiv Prepr. quant-ph/0306072*, (27).

Acknowledgements

First and foremost I want to express my thankfulness to *Markus Arndt*, being the kind and considerate professor he is, for giving me the opportunity to work on this thesis and to gain my experiences within his group. At this, I am obliged for being taught and inducted into our particular project by *Philipp Schmid*, an enthusiastic experimentalist with whom I enjoyed discussing and learning. Besides, I appreciate the pleasant times in the lab and the nice atmosphere with my colleagues in the office, where we enjoyed plenty of funny and interesting dialogues. Additionally I have found a unique friend in *Philipp Geyer* who is always helpful and amusing with his very own temper and exeptional ideas. Also I'm very grateful for *Joseph Cotter* and *Christian Brand* patiently reading, revising and finding the thesis within the mountain of papers I've placed into their hands.

For the many years that passed during my studies at the faculty I gained several friends and met even more lovely people with whom I have many happy memories. Among the great professors that lectured me, I want to mention *Herbert Pietschmann* for giving me delight with his wonderful courses which retain a small portion of the traditional philosophical background the physics studies program would have otherwise lost. Thereupon I want to thank *Helmut Neufeld* for the many amusing discussions that we had and even resulted in a refreshing friendship. Beyond all, I have to phrase my huge gratefulness to my very precious friend *Ursula Ludacka* with whom I share so much and for our mutual encouragement.

Most of all, I devote my deep gratitude to my beloved family, in particular my mother *Olga Mitrea*, my father *Philipp Lang* and my grandmother *Rodica Witkowski-Costin* who have made everything imaginable possible for me, always being generous, caring and wise, and providing me a wonderful and loving home. I am utterly thankful and happy for all of the support and understanding I have had along the way to this part of my life.

Finally, with words of my greatuncle *Heinz von Förster*, which are important to me and reflect a speck of my perception, I want to conclude this master thesis:

"In jedem Augenblick unseres Lebens sind wir frei, auf die Zukunft hin zu handeln, die wir uns wünschen."

Curriculum Vitae

Personal information

Name	Philine Mitrea, BSc.
Address	Franzensgasse 18 / 32 1050 Vienna
Telephone	+43 699 111 766 47
Date of birth	May 29th 1989
Parents	Olga Mitrea and Philipp Lang
Place of birth	Vienna, Austria
Nationality	Austria

Education

10/2012 - 11/2014	**Master thesis about simulations on linear ion trap devices** for massive molecular beams in the Quantum Nanophysics Group, mentored by Univ. Prof. Dr. Markus Arndt
10/2012 - 02/2013	**Teaching assistent**, University of Vienna, Faculty of Physics Courses: "Theoretical physics 1: Classical mechanics" and "Introduction in Physics 3: Atoms, quanta and nucleii"
2011 - 2015	**Studies of master degree physics**, University of Vienna
02/2011	**Conferment of Bachelor of Science (BSc.)**

07/2010 - 09/2010	**Bachelor thesis about radiometric dating methods**, mentored by Univ. Prof. Dr. Harry Friedmann
09/2008 - 10/2008	**Internship in the Quantum Nanophysics Group**, mentored by Univ. Prof. Dr. Markus Arndt
2007 - 2011	**Studies of bachelor degree physics**, University of Vienna
06/2007	Passed high school leaving examination "**Matura**" **with excellent success**
05/2007	"**Certificate of Recognition" of the Bentley Education Network** for using MicroStation
2003 - 2007	High school "Bundesrealgymnasium IV Waltergasse", Vienna
1999 - 2003	Secondary school "St. Marien Liniengasse", Vienna
1995 - 1999	Elementary school "Piaristen St. Thekla", Vienna

Computer skills

Operating systems	Apple (advanced), Windows (good), Linux (good)
Programming	Mathematica (good), MATLAB (basics), LabView (basics), Lua (good)
Office, typesetting	MS Office (advanced), LaTeX (good)
Simulation, CAD	SIMION (good), SolidWorks (good), MicroStation (good)
Graphics, video-editing	Photoshop (advanced), Illustrator (good), iMovie (advanced), Final Cut Pro (good)